Suture Accessory Sensor to Monitor Graft Loading in Reconstructed Ulnar Collateral Ligaments

by

Kaylee Marie Meyers

A dissertation accepted and approved in partial fulfillment of the requirements for the degree of

Doctor of Philosophy

In Bioengineering

Dissertation Committee:

Dr. Nick Willet, Chair

Dr. Keat Ghee Ong, Advisor

Dr. Nick Strasser, Core Member

Dr. Matthew Johnston, Core Member

Dr. Mike Hahn, Institutional Representative

University of Oregon

&

Oregon State University

Spring, 2026

© 2026 Kaylee Marie Meyers

Abstract

Kaylee M. Meyers

Doctor of Philosophy in Bioengineering

Title: Suture Accessory Sensor to Monitor Graft Loading in Reconstructed Ulnar Collateral Ligaments

The engineering objective of the thesis was to develop a wireless and battery-free implantable sensor in the form of an inductor-capacitor (LC) suture accessory to detect graft loading magnitude in ulnar collateral ligament reconstruction (UCLR). A central question guiding the objective consisted of determining if a passive, implantable LC-based suture sensor can provide quantitative and reliable measurements of graft loading under clinically relevant biomechanical conditions specific to UCLR. The overall hypothesis was that tensile loading applied to a ligament graft construct can produce measurable and repeatable changes in the resonance behavior of an integrated passive LC-based suture accessory sensor, enabling wireless detection of relative changes in graft loading under biomechanically relevant UCLR conditions.

To test the hypothesis, a suture accessory sensor was engineered with plastic materials and an embedded circuit to detect suture loading force over ranges applied during human ulnar collateral ligament reconstruction (20-40 N). Sensor performance (i.e., sensitivity, drift, repeatability, etc.) was determined with mechanical testing. A detection system comprising a miniaturized network analyzer, a detection coil, and a microcontroller circuit was engineered to provide information on loading force measured by the implanted sensor. Transmission metrics (i.e., detection distance, alignment, tissue thickness, etc.) were assessed and optimized through device

and antenna design. Finally, a preclinical *ex vivo* study was performed to assess sensor functionality in a joint ligament reconstruction environment to evaluate the sensor's ability to detect changes in graft tension during valgus stress and flexion/extension as well as graft failure via knot slippage.

In conclusion, the thesis work established the basic functionality of a suture accessory sensor that could eventually be utilized in measuring tension in UCLR grafts to help surgeons determine correct tension during operation and physical therapists with guiding post-operative rehabilitation. Additionally, the sensing technology could inform healthcare professionals of reinjury due to suture breakage or graft failure complications. Important questions on how tight grafts should be tensioned, how well graft tension is maintained after surgery, and how variations in surgical technique influence graft loading behavior could be elucidated by the sensing platform.

This dissertation includes previously published, unpublished, and coauthored material.

Acknowledgements

I would like to thank Dr. Keat Ghee Ong for his guidance and support in the execution of the biosensors research project outlined in the dissertation. Further, I am grateful to all members of the Ong Lab for their assistance and comradery. In addition, special thanks are due to my committee members for overseeing the thesis dissertation project. The investigation was supported in part by the National Science Foundation Graduate Research Fellowship Program and the Joe and Clara Tsai Foundation, the Wu Tsai Human Performance Alliance.

Curriculum Vitae

Kaylee Marie Meyers

PROFESSIONAL SUMMARY

As a biomedical innovator with 8 years of research experience, I have developed skills in electronics design, leadership, teaching, and entrepreneurship while interacting with clinicians, FDA regulatory officials, and start-up businesses to engineer wearable and implantable medical devices. I graduated with highest academic honors, received the most prestigious student research awards in the country (*Goldwater* & *NSF GRFP*), and won over $1.2M in grants for biomedical research and STEM education.

EDUCATION

PhD Bioengineering (*Electronics Focus*) 4.20 GPA **August 2021 – June 2026**

University of Oregon/Oregon State University: Knight Campus for Accelerating Scientific Impact

- National Science Foundation Graduate Research Fellowship Program (GRFP) Awardee
- Thesis: *Wireless, Passive Suture Sensors for Load Monitoring in Reconstructed Ligaments*

MS Bioengineering (*Electronics Focus*) 4.20 GPA **August 2021 - June 2023**

University of Oregon: Knight Campus for Accelerating Scientific Impact

- Women's Innovation Network and Lens of the Market Entrepreneurship Trainee
- Stanford University's Wu Tsai Human Performance Alliance Most Innovative Demonstration Award

BS Biomedical Engineering (*Materials Focus*) 4.00 GPA, Honors **August 2017 - May 2021**

Michigan Technological University

- Provost's Award for Scholarship (Top student in academics and research at Michigan Tech)
- University Honors (Top 2% in College of Engineering)
- Barry Goldwater Scholar and Biomedical Engineering Departmental Scholar

---

RESEARCH EXPERIENCE

Graduate Researcher **August 2021 - Present**

Suture Accessory Sensors to Monitor Graft Loading

Biosensors Laboratory (Eugene, OR)

- Secured a competitive (14% awardee rate) National Science Foundation Graduate Research Fellowship totaling $159k to independently fund my graduate school education and training
- Designed implantable, wireless, and battery-free suture accessory sensors to detect loading (10-50N) in reconstructed ligaments for personalizing orthopedic surgery and post-operative therapy methods
- Fabricated prototype sensors using CAD (Inventor, Fusion), 3D printing (FDM, SLA), and injection molding while implementing FEA (Ansys) to tailor sensor loading mechanics
- Optimized sensor design for reducing operating frequency by 20x to improve signal transmission
- Automated (Visual Studios C#) sensor data collection processes for evaluating loading performance with mechanical testing and antenna coupling cutting data collection time by 75%

Tracheostomy Tube Airway Complication Monitor

Children's National Hospital (Washington D.C.)

- Collaborated remotely with Children's National Hospital to design a wearable tracheostomy tube complication monitor for identifying airway emergencies in ventilator-independent pediatric patients
- Prototyped (Fusion, Eagle) and programmed (C++) the device to reduce size by 50% and weight by 85% while implementing a power budget to increase battery life by 7x compared to existing monitors
- Interviewed FDA regulatory officials, insurance reimbursement specialists, and clinicians (nurses, physicians, infection control staff) at Children's National Hospital to implement design feedback
- Collected primary and secondary market analysis data from >50 sources to write a STTR grant
- Worked as a team to receive a *National Capital Consortium for Pediatric Device Innovation Award*
- Mentored 7 undergraduate students in sensor design, testing, data analysis, and presentation

Undergraduate Researcher **September 2017 - July 2021**

Nitric Oxide Releasing Composite Hydrogels for Tendon Repair

Engineered Biomaterials Laboratory (Houghton, MI)

- Wrote 4 biomaterials grant proposals and was awarded $17k in fellowships for undergraduate research
- Synthesized and functionalized injectable PEG-fibrin based hydrogels for thermal-mediated nitric oxide drug delivery to treat tendinopathy
- Evaluated hydrogel mechanical properties (stiffness, swelling ratio) to tailor the mechanics of the polymer network to the native tendon tissue microenvironment
- Conducted advanced cell culture and protein activation characterization (gelatin zymography) to investigate the effects of nitric oxide delivery on the activation of enzymes that degrade network collagens and extracellular matrix proteins

Focused Ultrasound for the Remote Modulation of Nitric Oxide Release from Injectable Composite Hydrogels

Focused Ultrasound Laboratory (Blacksburg, VA)

- Designed (Inventor), wired, and programmed (MATLAB) a focused ultrasound system to study temperature-mediated nitric oxide drug delivery from hydrogels
- Performed thermocouple and thermodynamic FEA analysis (COMSOL) to evaluate ultrasound-mediated heating of hydrogels in 3D
- Mentored 5 undergraduate students in biomaterials design, testing, data analysis, and presentation

---

INDUSTRY EXPERIENCE

Technical Consultant: Electronics Design **June 2024 – January 2026**

Penderia Technologies Incorporated (Eugene, OR)

- Designed printed circuit boards (Eagle) for a radiofrequency network analysis medical device to detect electrical resonance-based implantable sensors following IEC 60601 EMI/EMC standards
- Programmed device microcontrollers (C++) while employing both serial communication (UART, I2C, SPI, USB) and peripheral Bluetooth Low Energy (BLE) protocols
- Developed a GUI computer app (Visual Studios C#) following central Bluetooth Low Energy (BLE) protocols to wirelessly stream device readings with a sampling rate of 1Hz
- Assisted with successful biotech small business grants (SBIR Phase I & II) totaling ~$2M

Senior Electrical Engineer **January 2026 - Present**

Medtronic PLC (Mounds View, MN)

- Developed and validated test methods for a radiofrequency medical device generator utilizing IEC 60601 industry regulations and standard operating procedures
- Implemented quality systems management and product development processes (ex. dFMEA, TMV, DFMA) in device characterization and design
- Automated power and impedance data collection (MATLAB) and analysis (Minitab) processes to save time by writing custom programs
- Developed an installation qualification plan for a custom electronics characterization testing device

---

SKILLS

Electronics: Microcontrollers, Bluetooth Low Energy, Printed Circuit Board Design (Eagle), Serial Communication (UART, I2C, SPI, USB), Sensor Design and Characterization

Programming: C++, C#, MATLAB, Visual Studios, GUI App Development, Data Collection Automation

Mechanical: Computer Aided Drafting (Inventor Pro, Fusion 360, AutoCAD), 3D Printing (FDM, SLA), Benchtop Injection Molding, Mechanical Testing, Basic Machining (mill, CNC, lathe)

Modeling: Finite Element Analysis (COMSOL, Ansys), Mechanics, Thermodynamics

Entrepreneurship: Small Business Grant Writing, Market Analysis, Patent Claim Drafting

---

TEACHING EXPERIENCE

FTC Robotics Coach **August 2025 – Present**

Essexville-Hampton Public Schools (Essexville, MI)

- Mentored middle school students in CAD design and 3D printing while leading robotics educational and competition activities
- Provided hands-on STEM education outreach activities for sixth graders to increase middle school robotics student participation by 25% and triple girl membership

Circuit Design for Medical Devices Instructor **August 2024 – March 2025**

University of Oregon (Eugene, OR)

- Developed and taught a 10-week graduate-level course employing hands-on circuit design (Eagle) and embedded systems (C++) training while assisting students with troubleshooting term projects

Tech Tutors Instructor **May 2020 – May 2021**

Michigan Technological University (Houghton, MI)

- Taught a full high school math class (Precalculus) over the summer semester
- Tutored 5 elementary thru high school students during the academic year

Undergraduate Teaching Assistant **August 2019 – May 2020**

Michigan Technological University (Houghton, MI)

- Led hands-on learning laboratory activities covering the human body's organ systems to complement Anatomy and Physiology lecture material

Summer Youth Programs Counselor **April 2018 – August 2018**

Michigan Technological University (Houghton, MI)

- Provided pre-college students with the opportunity to explore careers in science, technology, engineering, and mathematics (STEM) as a part of Michigan Tech's Summer Youth Programs

---

LEADERSHIP & SERVICE

Executive & Founding Director Essexville Education Fund **September 2022 - Present**

Essexville-Hampton Public Schools (Essexville, MI)

- Won a highly competitive (10% awardee rate) $1M matching grant to build a regional STEM Center in my hometown from the State of Michigan's Department of Labor and Economic Opportunity
- Collaborated with teachers, architects, businesses, politicians, and non-profits to raise matching funds
- Advised on center design and equipment to train K-12 students in skilled trades and STEM careers

Tech Tutors Co-Director **May 2020 - May 2021**

Michigan Technological University (Houghton, MI)

- Co-developed a virtual K-12 tutoring program (Tech Tutors) during the COVID pandemic that served over 200 K-12 students from more than 30 different school districts across Michigan
- Trained tutors, collected program statistics, and designed the Tech Tutors website (techtutors-mtu.org)
- Received Michigan Tech's *Exceptional Civic Engagement* and *Outstanding Leadership* awards

Student Success Orientation Team Leader & Peer Mentor **Aug 2018 - May 2019**

Michigan Technological University (Houghton, MI)

- Introduced new first-year students to campus and provided methods for success in college
- Mentored first-year biomedical engineering students in courses and extracurricular activities
- Received the Department of Biomedical Engineering's *Outstanding Classmate Award*

GRANTS

Michigan Community Center Capital Grant Award (2024-2026)

$1M matching grant awarded from the Michigan Department of Labor and Economic Opportunity to support the construction of the Essexville-Hampton Public Schools' Regional STEM Center. There were ~1,000 applicants and 100 awardees (10% awardee rate) while only 8 public school districts received capital funds. Matching funds are being obtained via local business and private donations as well as a school bond.

National Science Foundation: Graduate Research Fellowship Program Award (2023-2025)

Most prestigious STEM graduate student research award in the country from the National Science Foundation. The competitive award (14% awardee rate) provides three years of financial support for tuition and stipend totaling $159k.

Knight Campus Mentor Funding Award (2023)

Provided 1 year of funding for a graduate student to mentor and train an undergraduate researcher conducting an independent engineering project.

Barry Goldwater Scholar (2020)

Most prestigious scholarship in the natural sciences, engineering, and mathematics in the United States for undergraduate research. The award provides a $7k scholarship for undergraduate education.

Charles Steger Global Internship Award: Focused Ultrasound Foundation (2019)

Competitive international fellowship program through the Focused Ultrasound Foundation designed to fund high school and undergraduate university students' research projects in the field of focused ultrasound.

MTU Undergraduate Research Internship Program Award (2018)

A competitive university-wide fellowship program designed to fund Michigan Tech students in their proposed research projects during the academic year.

MTU Summer Undergraduate Research Fellowship (2018)

A competitive (15% awardee rate) university-wide fellowship program designed to fund Michigan Tech students in their proposed research projects during the summer semester.

AWARDS & HONORS

National Capital Consortium for Pediatric Device Innovation Honorable Mention (2023)

Awarded to the 4th place pediatric medical device pitch at the 2023 National Capital Consortium for Pediatric Device Innovation conference.

Stanford’s Wu Tsai Human Performance Alliance Most Innovative Demonstration Award (2023)

Awarded to the most innovative biotechnology demonstration at Stanford University's 2023 Wu Tsai Human Performance Alliance conference.

Biomedical Engineering Graduating Scholar Award (2021)

Awarded to an undergraduate senior majoring in Biomedical Engineering, who best represents academic achievement in our department. This student is considered excellent, not only academically, but also for participation in research activity, intellectual curiosity, creativity, and communication skills.

MTU Exceptional Civic Engagement Award (2021)

The Exceptional Civic Engagement Award recognizes a student group that has sponsored an exceptional service project, awareness event, or philanthropic endeavor with the goal of improving the quality of the community. Our Tech Tutors program received the award for helping over 200 different K-12 students from 30 different school districts across Michigan during the first year of the COVID pandemic.

University Honors (2017-2021)

Published at the end of each spring semester, the university honors list recognizes undergraduate students who carry 12 or more credits for both the fall and spring semesters and have placed in the upper 2% of the College of Engineering.

Outstanding Biomedical Engineering Undergraduate Research Award (2020)

Presented to an undergraduate student who has significant research accomplishments, including presentations at conferences or co-authorship of publications.

MTU Provost’s Award for Scholarship (2020)

The Provost’s Award for Scholarship is given to a senior who best represents student scholarship at Michigan Tech. This outstanding student is considered excellent not only by academic standards, but also for participation in research scholarship activity, levels of intellectual curiosity, creativity, and communication skills.

Biomedical Engineering Departmental Scholar (2020)

Awarded to a student majoring in Biomedical Engineering, who best represents academic achievement in our department. This student is considered excellent, not only academically, but also for participation in research activity, intellectual curiosity, creativity, and communication skills.

Outstanding Biomedical Engineering Classmate Award (2019)

The Outstanding Biomedical Engineering Leadership Award is presented to two undergraduate students, majoring in Biomedical Engineering, who exemplifies a dedication to learning and a commitment to the Biomedical Engineering Department and University.

Outstanding Biomedical Engineering Leadership Award (2019)

Presented to a biomedical engineering undergraduate student who exemplifies a combination of outstanding scholastic achievement, demonstrated leadership on campus, and volunteer work in the community.

MTU Summer Undergraduate Research Fellowship Travel Award (2018)

A competitive university-wide funding opportunity to support an undergraduate research fellow with conference travel expenses.

LABORATORY MANAGEMENT

Laboratory Safety Officer **August 2023 – August 2025**

University of Oregon (Eugene, OR)

- Engineered safety controls to prevent workplace hazards in the electronics lab
- Identified and mitigated 14 electrical and wet lab hazards to improve workplace safety
- Trained 8 undergraduate and graduate students in safe electrical lab techniques

Undergraduate Laboratory Manager **May 2020 – May 2021**

Michigan Technological University (Houghton, MI)

- Mentored 5 undergraduate students in biomaterials and bioinstrumentation design, testing, data analysis, and presentation
- Taught 3 undergraduate students how to successfully write biomedical grant proposals totaling $15k
- Managed a cell culture laboratory by overseeing supplies and ensuring biohazard disposal compliance

Safety Captain FIRST Robotics **May 2016 – May 2017**

Essexville-Hampton Public Schools (Essexville, MI)

- Designed and led an award-winning industrial safety program for my hometown's FIRST robotics team as a safety captain to improve workplace safety in the machine shop and robotics lab
- Updated my high school's safety data sheets (SDS) and chemical hygiene plan for over 100 chemicals to comply with new OSHA standards
- Revised the design of my school district's Critical Incident Management Booklets to be more accessible in K-12 classrooms in the event of an emergency
- Secured a $100 grant to mentor elementary and middle school robotics students in workplace safety and how to use Personal Protective Equipment (PPE)
- Won 7 industrial safety awards by delivering safety plan presentations at regional robotics competitions

---

PATENTS

1. Sherman J, Ong KG, **Meyers K**, "Tracheostomy Tube Complication Monitoring Accessory and Uses Thereof," Provisional Patent Application No. 63/580,685, Sept 5, 2023.
2. Karipott S, McGeehan M, **Meyers K**, Guldberg B, Ong KG, "Wireless measurement of suture tension," Patent Issued, US Patent No. 12,419,581, Sept 23, 2025.

PUBLICATIONS

1. **Meyers K**, Ong K (2026) "A Wireless, Passive Sensor to Monitor Intra- and Post-Operative Graft Loading in Reconstructed Medial Ulnar Collateral Ligaments." In-preparation.
2. Karipott S, **Meyers K**, Laffoon S, McGeehan M, Adams S, Riboh J, Strasser N, Gall K, Guldberg R, Ong K (2025) "Wireless Suture Button Accessory Sensor for Intra- and Post-Operative Monitoring of Suture Loading in Soft Tissue Reconstruction." Journal of Orthopaedic Experience & Innovation 6(1).
3. **Meyers K,** Burke Q, Siddiqui A, Zalzal H, Osmond T, Ong K, Sherman J (2024) "Tracheostomy Tube Monitoring Accessory to Detect Accidental Decannulation and Obstruction Emergencies in Ventilator-Independent Pediatric Patients." Tracheostomy 1(3):7-16.
4. **Meyers K**, Simon A, Khan Z, Rajachar RM, Vlaisavljevich E (2023) "Focused Ultrasound for the Remote Modulation of Nitric Oxide Release from Injectable Composite Hydrogels." Frontiers in Materials 10.
5. **Meyers K**, Ong K (2022) "Suture Sensor to Monitor Tensile Stress in Tendon and Ligaments During Physical Therapy for Sports Medicine Applications." IEEE Sensors Journal 22(19).
6. **Meyers K**, Ong K (2021) "Magnetoelastic Materials for Monitoring and Controlling Cells and Tissues." Sustainability MDPI 13.

7. **Meyers K**, Lee BP, Rajachar RM (2021) "Electroactive Polymeric Composites to Mimic the Electromechanical Properties of Myocardium in Cardiac Tissue Repair." Gels MDPI 7(2): 53.
8. Pinnaratip R, Bhuiyan S, **Meyers K**, Rajachar RM, Lee BP (2019) "Multifunctional Biomedical Adhesives." AHM 1801568.
9. Sheffield, C, **Meyers K**, Johnson E, Rajachar RM (2018) "Application of Composite Hydrogels to Control Physical Properties in Tissue Engineering and Regenerative Medicine." Gels MDPI 4(2): 51.

CONFERENCE PRESENTATIONS

1. **Meyers K**, Ong KG. Suture Button Accessory Sensor for Suture Load Monitoring in Reconstructed ACL. Wu Tsai Human Performance Alliance at Oregon Research Symposium 2024 Eugene, OR (Podium)
2. Sherman J, Zalzal H, Burke Q, **Meyers K**, Ong K. Trach Sense: Pediatric Tracheostomy Tube Monitor. Global Tracheostomy Symposium 2024 (Online Presentation)
3. Sherman J, **Meyers K,** Zalzal H, Burke Q, Siddiqui A, McGeehan M, Ong K. Tracheostomy Tube Complication Monitoring Accessory to Alert Caregivers of Accidental Decannulation and Obstruction Emergencies. Children's National Hospital Symposium 2024 Washington DC (Poster)
4. **Meyers K**, Ong KG. Wearable Wireless Detection Device to Monitor Loading in Tendon and Ligament Suture Sensors During Physical Therapy. Oregon Bioengineering Symposium 2023 Eugene, OR (Poster)
5. **Meyers K**, Ong KG. Wearable Detection Device and Pledget Sensor to Monitor Loading in Tendon and Ligament Sutures During Physical Therapy. BMES 2023 Seattle, WA (Poster)
6. Sherman J, **Meyers K**, Ong KG, McGeehan M, Zalzal H. Trach Sense: Pediatric Tracheostomy Tube Monitor. Pediatric Device Innovation Symposium 2023 Anaheim, CA (Funding Pitch)
7. **Meyers K**, Balthazaar L, Ong KG. Pledget Sensor to Monitor Tendon and Ligament Suture Force During Physical Therapy. Wu Tsai Human Performance Alliance Research Symposium 2023 Palo Alto, CA (Demonstration)
8. **Meyers K**, Balthazaar L, Ong KG. Pledget Sensor to Monitor Loading in Tendon and Ligament Sutures During Physical Therapy. BMES 2022 San Antonio, TX (Podium)
9. **Meyers K**, Balthazaar L, Ong KG. Pledget Sensor to Monitor Loading in Tendon and Ligament Sutures During Physical Therapy. Oregon Bioengineering Symposium 2022 Corvallis, OR (Poster)
10. **Meyers K**, Ong KG. Suture Sensor to Monitor Tensile Stress in Tendon and Ligaments During Physical Therapy for Sports Medicine Applications. Wu Tsai Human Performance Alliance at Oregon Research Symposium 2022 Eugene, OR (Podium)
11. **Meyers K**, Karipott S, Guldberg B, Ong KG. Suture Button Sensor to Monitor Strain in Reconstructed Anterior Cruciate Ligament (ACL) During Rehabilitation. Oregon Bioengineering Symposium 2021 (Poster)

12. **Meyers K**, Simon A, Rajachar RM, Vlaisavljevich E. Focused Ultrasound for the Remote Modulation of Nitric Oxide Release from Injectable Composite Hydrogels. FUSF 2020 Virtual (Poster)
13. Khan Z, **Meyers K**, Verbridge S, Rajachar RM, Vlaisavljevich E. Therapeutic Focused Ultrasound Stimulated Controlled Release of Nitric Oxide from an Injectable Hydrogel. BMES 2019 Philadelphia, PA (Poster)
14. Caspers K, **Meyers K**, Kwesiga M, Lee BP, Rajachar RM. Impact of Fibrin Microparticle Cross-linking Density on Physical and Rheological Properties of Composite Polyethylene Glycol-Fibrin Microparticle Hydrogels for use in Tendon Repair. SFB 2019 Seattle, WA (Poster)
15. **Meyers K**, Joseph C, Lee BP, Rajachar RM. Nitric Oxide Releasing Composite Hydrogels for Tendon Repair via Matrix Metalloproteinase Controlled Pathways. ASMB 2018 Las Vegas, NV (Podium)
16. **Meyers K**, Joseph C, Lee BP, Rajachar RM. Nitric Oxide Releasing Composite Hydrogels for Tendon Repair via Matrix Metalloproteinase Controlled Pathways. MPS 2018 Houghton, MI (Poster)

PROFESSIONAL ACTIVITIES & COMMUNITY ENGAGEMENT

Society of Women Engineers (SWE)

Biomedical Engineering Society (BMES)

Tau Beta Pi: National Engineering Honor Society (Service committee)

Wu Tsai Human Performance Alliance

Little Brothers Friends of the Elderly Visitation Volunteer

SCHOLARSHIPS & FUNDING ACKNOWLEDGMENTS

National Science Foundation: Graduate Research Fellowship Program Award (2023-2026)

Knight Campus First Year Fellowship (2021)

Tau Beta Pi National Engineering Honors Society Scholarship (2020)

Dyste Family Endowed Scholarship: Midland Community Foundation (2020)

Turner Alfrey Jr. Scholarship: Midland Community Foundation (2020)

Michigan Tech Provost Award for Scholarship (2020)

Barry Goldwater Scholarship (2020)

Mid-Michigan Health: Bernard F. and Melissa Anne Bailey Family Fund Scholarship (2018-2020)

Charles Steger Global Internship: Focused Ultrasound Foundation (2019)

Michigan Tech Undergraduate Research Internship Program (2018)

Michigan Tech Summer Undergraduate Research Fellowship (2018)

Society of Women Engineers: Brill Family Scholarship (2018)

Society of Women Engineers: Martha Maxwell Memorial Scholarship (2018)

Michigan Masonic Charitable Foundation Scholarship (2017)

United Bay Community Credit Union Scholarship (2017)

Sunrise Family Credit Union: First Prize Leadership Essay Scholarship (2017)

Josh Jasman Memorial Scholarship (2017)

Lily Marie Tarkowski Memorial Scholarship (2017)

Bay City Morning Rotary Club Scholarship (2017)

Michigan Society of Professional Engineers Scholarship (2017)

Martin Luther King Jr. Regional Scholarship (2017)

Michigan Tech FIRST Robotics Scholarship (2017-2021)

Table of Contents

Abstract 3

Acknowledgements 5

Curriculum Vitae 6

List of Figures 24

List of Tables 32

Chapter 1: Introduction 33

1.1 Aim 1: Fabricate and characterize a suture accessory sensor platform. 35
1.2 Aim 2: Develop wearable detection device. 35
1.3 Aim 3: Assess sensor performance in ligament reconstruction model. 36
Impact 36

Chapter 2: Background 37

2.1 Ulnar Collateral Ligament Reconstruction (UCLR) 37
2.1.1 UCL Structure & Function 37
2.1.2 UCL Reconstruction Occurrence and Projected Growth in Baseball 38
2.1.3 UCL Surgical Reconstruction Procedure 40
2.1.4 Rehabilitation of Reconstructed UCL 41
2.1.5 Importance of UCLR Graft Tension & Loading 43
2.2 Current Methods for Estimating UCL Loading 43
2.3 Inductor-Capacitor (LC) Sensors in Medical Applications 44
2.3.1 LC Sensor Theory 45
2.3.2 Electrical Resonance 47
2.3.3 Quality Factor 48
2.3.4 Radiofrequency Transmission Through Tissues 50
2.3.5 Electromagnetic Coupling Considerations 50
2.3.6 Reflected Impedance Measurements 51
2.4 Planar Inductors as LC Sensors 55
2.4.1 Equivalent Circuit 55

2.4.2 Stacking Planar Inductors 57
2.4.3 Bending Planar Inductors 59
2.4.4 Planar Inductor LC Sensor Design Environmental Considerations 61
Chapter 3: Engineering a Force Detecting LC Sensor 62
3.1 Introduction 63
3.2 Sensor Design Clinical Feedback 64
3.2.1 Voice of Surgeon 64
3.2.2 Voice of Physical Therapist 65
3.3 Sensor Design Considerations for Ulnar Collateral Ligament (UCL) Reconstruction. 65
3.3.1 Force Detection Range and Sensitivity 65
3.3.2 Sensor Reproducibility 66
3.3.3 Sensor Drift 66
3.3.4 Load to Failure 66
3.3.5 Temperature Effects 67
3.3.6 Sensor Lifetime 67
3.3.7 Tissue Depth Requirement 67
3.3.8 Sensor Size 68
3.3.9 Sensor Materials 68
3.4 Sensor Design Iteration Overview 68
3.5 Sensor Iteration 1: 3D-Printed PLA Body + Rectangular LC Circuit 70
3.5.1 Sensor Fabrication Materials and Methods 70
3.5.2 Sensor Bending and Finite Element Analysis (FEA) 71
3.5.3 Suture Tension Detection 72
3.5.4 Detection Distances 75
3.6 Sensor Iteration 2: Injection Molded HDPE Body + Rectangular LC Circuit 76
3.6.1 Sensor Fabrication Materials and Methods 76
3.6.2 Sensor Bending and Finite Element Analysis (FEA) 80
3.6.3 Suture Tension Detection 81
3.7 Sensor Iteration 3: Machined PEEK Body + Rectangular, Stacked LC Circuit 86
3.7.1 Sensor Fabrication Materials and Methods 86

3.7.2 Impact of Substrate Thickness 87
3.7.3 Impact of Inductor Stacking in LC Circuit 89
3.7.4 Suture Tension Detection 91
3.8 Sensor Iteration 4: Machined PEEK Body + Rounded Rectangular, Stacked LC Circuit 94
3.8.1 Sensor Fabrication Materials and Methods 94
3.8.2 Planar Inductor Coil Reproducibility 96
3.8.3 Influence of Sensor Aspect Ratio 97
3.8.4 Sensor Bending and Finite Element Analysis (FEA) 99
3.8.5 Suture Tension Detection 100
3.8.6 Temperature Testing 105
3.9 Limitations & Conclusions 106
Chapter 4: Engineering an LC Sensor Detection Device 108
4.1 Introduction 108
4.2 Detection Device Design Clinical Feedback 109
4.2.1 Voice of Surgeon 109
4.2.2 Voice of Physical Therapist 109
4.2.3 Voice of Regulatory Consultant 110
4.3 Detection Device Design Considerations 110
4.3.1 Wearable Detection Device Size & Weight 110
4.3.2 Detection Range 110
4.3.3 Connection Range 110
4.3.4 EMC, EMI, and ESD Regulations 110
4.3.5 Battery Life 111
4.3.6 Sampling Rate 111
4.4 Fabrication of Detection Device 111
4.5 Detection Device Testing 119
4.5.1 Connection Distance 119
4.5.2 Antenna Optimization 120
4.5.3 Resolution & Stability Testing 123

4.5.4 ESD, EMC, & EMI Testing 124
4.5.5 Manual Sensor Coupling Displacement Test 126
4.5.6 Automated Sensor Coupling Displacement Test 128
4.5.7 Rotation & Tilt Coupling Test 132
4.5.8 Skin Transmission Test 133
4.6 Limitations & Conclusions 134

Chapter 5: Detecting Graft Loading in Ligament Reconstruction 136

5.1 Introduction 136
5.2 *Ex Vivo* Cervid Cadaver Model 141
5.2.1 Model Rationale 141
5.2.2 Model Methods 143
5.3 *Ex Vivo* Cervid Cadaver Model Results 145
5.3.1 Baseline Frequency Change 145
5.3.2 Valgus Stress 146
5.3.3 Flexion & Extension 148
5.3.4 Failure Detection 150
5.3.5 Static Loading 151
5.4 Limitations & Conclusions 153

Chapter 6: Conclusions 154

6.1 Primary Conclusions & Contributions to the Field 154
6.2 Limitations 156
6.3 Future Directions 157

Appendix 1: Tracheostomy Tube Monitoring Accessory to Detect Accidental Decannulation and Obstruction Emergencies in Ventilator-Independent Pediatric Patients 159

1. Introduction 161
2. Methods 164
A. Custom Carbon Dioxide Monitoring Tracheostomy Tube Attachment 164
B. Pediatric Tracheostomy Model Fabrication 166
C. Breathing Circuit Set-Up for Simulations 168

D. Simulation of Tracheostomy Tube Emergency Events 172
3. Results 173
A. Normal Breathing Measurements 173
B. Incorrect Insertion Simulation 174
C. Accidental Decannulation Simulation 175
D. Partial and Full Blockage Simulation 176
4. Discussion 178
Appendix A 181
Appendix B 182
Appendix C 183
References 184

List of Figures

Figure 1. Anatomy of the human elbow joint showing the UCL complex (Image generated with the assistance of Google Gemini Flash 3.0)..... 38

Figure 2. Early acceleration phase of a baseball pitch loads the UCL in tension (red arrows) (A). Loading of ligaments in the human elbow under valgus stress (B). (Images generated with the assistance of Google Gemini Flash 3.0) 39

Figure 3. During a UCLR, the ruptured anterior UCL (A) is replaced to restore joint stability. Bone tunnels are drilled into the ulna and medial epicondyle of the humerus (B). Whereafter a graft is threaded through the ulnar bone tunnels into the humeral bone (C). The graft can be fixed with a suture button (D). Figure represents the proximal single-tunnel suspensory fixation technique for UCLR. (Images generated partially with the assistance of Google Gemini Flash 3.0) 41

Figure 4. Schematic outlining injury, surgery, and rehabilitation phases of UCLR. For full UCL tears, UCLR is performed 0-1 month following injury while post-operative rehabilitation lasts up to 12 months for full recovery..... 42

Figure 5. Electromagnetic coupling between inductors of a sensor (L_s) and detection coil (L_d) (A). Circuit diagram of LCR sensor coupled to a detection device where R is resistance, C is the capacitance of the capacitor, L_s is inductance of the sensor coil, L_d is inductance of the detection coil, and Z is measured impedance (B). (Images partially generated with the assistance of Google Gemini Flash 3.0)..... 47

Figure 6. Real (A) and imaginary (B) impedance spectra where X_C is capacitive reactance, X_L is inductive reactance, Z is impedance, R is resistance, and f_r is resonance frequency..... 48

Figure 7. Resonance spectra showing quality factor metric determination (A) and the impact of quality factor on resonance spectra shape (B) where f_l is the lower frequency with signal strength equal to 70.7 % of the resonance amplitude, f_h is the higher frequency with signal strength equal to 70.7 % of the resonance amplitude, B is bandwidth, Q is quality factor, and f_r is resonance frequency..... 49

Figure 8. Circuit diagram of LC sensor coupled to a detection device where R_s is parasitic resistance of the sensor, C_s is the capacitance of the sensor, L_s is inductance of the sensor coil, Z_d, is the impedance of the sensor circuit, M is mutual inductance, L_d is inductance of the detection coil, R_d is parasitic resistance of the detection coil, and Z_d is impedance measured by the detection coil (A). Reflected impedance spectra where Z_d is the impedance measured by the detection coil and f_r is resonance frequency (B). Reflection coefficient (S_{11}) spectra where f_r is resonance frequency (C). 54

Figure 9. Planar inductor square and spiral inductor design examples where trace width (w) and spacing (s) are visualized (A). Equivalent circuit of planar inductor coil with parasitic resistance and capacitance (B). (Images partially generated with the assistance of Google Gemini Flash 3.0) 56

Figure 10. Parasitic capacitance (C_p) among planar inductor traces showing capacitance between coplanar (on the same layer) traces. 57

Figure 11. Simplified representation of a 2-layer inductor sensor circuit and detection antenna (A). Circuit diagram of the suture accessory sensor coupled to a detection antenna (parasitic resistance not shown) (B). L_1 is inductance of the top sensor coil, L_2 is inductance of the bottom sensor coil, L_3 is inductance of the detection coil, C_p is parasitic capacitance of the sensor circuit, M_{13} is mutual inductance between the top sensor coil and the detection coil, M_{12} is mutual inductance between the top sensor coil and the bottom sensor coil, M_{23} is mutual inductance between the bottom sensor coil and the detection coil, and Z is measured impedance. 58

Figure 12. Parasitic capacitance (C_p) among stacked planar inductor traces showing capacitance between both board layers and coplanar (on the same layer) traces. 59

Figure 13. Bending of planar inductor traces resulting in a decreased distance between traces and therefore increased parasitic capacitance. (Images partially generated with the assistance of Google Gemini Flash 3.0) 60

Figure 14. Advantages of utilizing an LC sensor integrated into a suture accessory with implantable devices. 64

Figure 15. Schematic showing design evolution of both the sensor LC circuit and sensor body. 69

Figure 16. Printed planar inductor coil on a flexible polyimide substrate (A). Equivalent circuit of the planar inductor coil (R_p = parasitic resistance, C_p = parasitic capacitance, L = inductance) (B). 70

Figure 17. CAD model showing a suture passing through an exploded view of sensor components (A) (PLA = polylactic acid, LC = inductor-capacitor). Suture sensor dimensions in assembled CAD model (B). 71

Figure 18. Image showing assembled sensor incorporation in a basic continuous suture pattern. 71

Figure 19. Deformation of suture sensor under loading from FEA study (A). Images showing side views of suture sensor deformation under unloaded (B) and loaded (C) conditions. 72

Figure 20. Change in sensor resonance frequency during loading (blue circles) and unloading (orange squares). *Error bars represent standard deviation of the mean (n = 3).* 74

Figure 21. Sensor resonance frequency under repetitive loading from 2 N (408.25 + 0.04 MHz) to 12 N (405.51 + 0.04 MHz). *Error bars represent standard deviation of the mean (n = 3).* 74

Figure 22. Sensor impedance at the resonance frequency as a function of tissue mimic thickness. *Error bars represent standard deviation of the mean (n = 3).* 75

Figure 23. Sensor design evolution from a 3D-printed polylactic acid (PLA) version to an injection molded high-density polyethylene (HDPE) version. 76

Figure 24. CAD drawings showing the isometric (A) and front (B) view of an oval-shaped sensor body. 77

Figure 25. Printed circuit pattern generated with an automated user-interface Eagle program (A). Exploded view of fused sensor layers (B). *LC = inductor-capacitor.* 78

Figure 26. Molds and components utilized to fabricate suture sensors. Mold halves are shown to highlight internal features and details. 79

Figure 27. Assembled 1.75 mm suture sensor with suture at a bone tunnel interface (A). Assembled suture sensors with 1.25 and 1.75 mm membrane thicknesses (B). 79

Figure 28. Resonance spectra of unloaded 1.75 mm suture sensor showing a resonance frequency of 620.0 MHz. 80

Figure 29. Images of a suture sensor in unloaded (A) and loaded (B) conditions showing a measured deformation (~0.25 mm) of the top sheet due to a static 35 N suture load. Simulated FEA loading of the sensor showing sensor deformation in the Z-direction at 35 N of loading (C). 81

Figure 30. Images of mechanical testing set-up showing major components utilized during sensor evaluation. 83

Figure 31. Suture sensor (0.75 mm size) mechanical testing sensitivity results showing sensor resonance frequency change during loading (blue circles) and unloading (orange triangles). *Error bars represent standard deviation of the mean (n = 3).* 83

Figure 32. Cyclic loading of the sensor from 5 to 35 N showing drift and deviation over 5 loading cycles (A). *Error bars represent standard deviation of the mean (n = 3).* Change in measured baseline resonance frequency after 100 and 200 loading cycles from 5 to 35 N *(n = 1)* (B). 85

Figure 33. Change in resonance frequency over 5 minutes after a constat 35 N of load is applied indicating instability and increasing drift in the sensing system. 85

Figure 34. Plastically deformed thinner (1.25 mm) sensor due to overloading (A). Example force loading curve showing loss in sensitivity due to overloading failure in a sensor (B). *Error bars represent standard deviation of the mean (n = 3).* 86

Figure 35. Stepwise images showing how the updated sensor design was fabricated and assembled. 87

Figure 36. Resonance frequency readings during loading and unloading of sensors of varying PEEK thickness (0.5, 1, and 2 mm). *Error bars represent standard deviation of the mean (n = 3).* 88

Figure 37. Changes in high-frequency sensor resonance frequency during loading of encapsulated (blue) and unencapsulated (orange) sensors. *Error bars represent standard deviation of the mean (n = 3).* 89

Figure 38. Top (A) and bottom (B) view of double-sided inductor design. Equivalent resonance circuit of inductor design where R_p = parasitic resistance, L = inductance, and C_p = parasitic capacitance (C). Printed circuit board of the double-sided inductor design on a flexible polyimide substrate (D). 90

Figure 39. Resonance spectra of the stacked inductor design circuit. 91

Figure 40. Polyimide (PI) substrate thickness impact on circuit resonance frequency (A), quality factor (Q-factor) (B), and impedance magnitude at resonance (C). *Error bars represent standard deviation of the mean (n = 3).* 91

Figure 41. Changes in sensor resonance frequency (A) and reflection coefficient at resonance (B) during loading (blue) and unloading (orange) from 10 to 50 N. *Error bars represent standard deviation of the mean (n = 3).* 93

Figure 42. Sensor output over time when loaded to 50 N (A) and unloaded to 10 N (B). Changes in sensor resonance frequency over 10 cycles of loading from 10 to 50 N (C). *Error bars represent standard deviation of the mean (n = 3).* Sensor output with overloading of 60 and 70 N *(n = 1)* (D). 94

Figure 43. Sensor components and threaded assembly (A). Rendering of the sensor placed at the proximal end of the humeral bone tunnel containing the UCL graft in an UCLR employing the proximal single-tunnel suspensory fixation technique (B). 96

Figure 44. Normal quartile plot (A), box-plot (B), and histogram with normal fit (C) of resonance frequency values for a lot of planar inductor sensors. 97

Figure 45. Sensors of varying length to study the impact of aspect ratio on sensor resonance metrics (A). The impact of aspect ratio on measured sensor resonance frequency (B), peak magnitude (C), and quality factor (D). *Error bars represent standard deviation of the mean (n = 3).* 98

Figure 46. Simulated deformation in the direction of applied load of the 0.75 mm thick sensor substrate (A) and strain in the longitudinal direction of the sensor substrate (B) at 40 N of loading..... 100

Figure 47. Mechanical testing set-up for evaluating the sensor response to loading (A). Close up image of a suture sensor within the sample holder (B)..... 101

Figure 48. A strong linear trend ($R^2 = 0.98$) was observed for the 0.75 mm thick sensor between load ranging from 10 to 50 N and measured resonance frequency (A). Magnitude of the reflection coefficient value at resonance frequency compared to load ranging from 10 to 50 N demonstrating a linear trend ($R^2 = 0.98$) (B). The sensitivity of the 1 mm thick sensor was lower than the 0.75 mm sensor (C). Of three different 0.75 mm thickness sensors, one had lower sensitivity (D). There were no differences in sensitivity before and after 10^4 cycles of loading (E) but baseline resonance frequency at 10 N of loading increased after 10^4 cycles of loading (F). *Error bars represent standard deviation of the mean (n = 3).*..... 103

Figure 49. Schematic of off-axis suture loading in the X and Y directions showing suture positioning in bone tunnel (A). Results indicated a lower sensitivity for off-axis loading in the X direction when compared to both on-axis loading and off-axis loading in the Y direction (B). *Error bars represent standard deviation of the mean (n = 3).*..... 105

Figure 50. Change in resonance frequency (A) and peak magnitude at resonance (B) with increasing temperature. *Error bars represent standard deviation of the mean (n = 3).* 106

Figure 51. Schematic diagram of the detection device sending and receiving signals from a computer via Bluetooth Low Energy (BLE) or Universal Serial Bus (USB) and implantable sensor via inductive coupling (not to scale) (A). Detection device with coil antenna (B). 109

Figure 52. Schematic showing connectivity among wearable device components and the implantable sensor. A computer or mobile device (1) communicates with the wearable detection device (2) over Bluetooth Low Energy so that the excitation and detection coil (3) receives loading data from the implantable sensor (4) that can be processed by a computer or phone app. 113

Figure 53. Detection system device major components (A) and assembly (B).....114

Figure 54. Wearable detection system device incorporated in a knee (top left), shoulder (bottom left) and ankle brace (right).....115

Figure 55. Graphical user interface of computer app designed for research use. 116

Figure 56. Redesigned wearable detection device circuit board integrating measurement circuitry with BLE microcontroller. 118

Figure 57. Prototype remote display device to receive wearable detection device force readings over a BLE connection.....118

Figure 58. Measured received signal strength indicator (RSSI) as a function of distance between Bluetooth Low Energy transmitter on wearable detection device and a phone receiver *(n = 1).* 120

Figure 59. Example of variations in detection antenna planar inductor designs covering differences in trace shape, thickness, and turn number. 121

Figure 60. Comparison of antenna design sensor coupling with measured resonance frequency (A), peak magnitude (B), and quality factor (C). *Error bars represent standard deviation of the mean (n = 3).* 122

Figure 61. At span settings of 1, 3, and 10 MHz measured resonance frequency (A), quality factor (B), and peak magnitude (C) were recorded. The standard deviation in measured metrics across span settings was also compared (D). *Error bars represent standard deviation of the mean (n = 100).* 124

Figure 62. Electromagnetic compatibility (EMC) of the detection device test results spectra showing emitted radiation levels above threshold at 900 MHz. 125

Figure 63. Schematic illustrating how the vertical and longitudinal distance between the antenna and sensor was varied to evaluate coupling behavior (A). Change in resonance frequency (B) and reflection coefficient at resonance (C) when antenna displacement is varied from 0-5 mm longitudinally for antennas placed 2, 4, and 6 mm above the high-frequency sensor. *Error bars represent standard deviation of the mean (n = 3).* 127

Figure 64. Image of automated sensor coupling test set up and components. 128

Figure 65. Scans of measured reflection coefficient (left), resonance frequency (middle), and quality factor (right) from 1 (top row) to 5 mm (bottom row) of displacement between the detection coil and sensor. 129

Figure 66. Schematic showing displacement directions between the sensor and detection coil (A). Changes in resonance frequency with displacement (0 to 10 mm) in both the X (blue circles) and Y (orange triangles) directions (B). Change in resonance frequency with displacement (1 to 10 mm) in the Z direction (C). A grid scan of peak magnitude at resonance in the X and Y directions at a Z displacement of 5 mm (D). Change in peak magnitude at resonance with displacement (0 to 10 mm) in both the X (blue circles) and Y (orange triangles) directions (E). Change in the value of peak magnitude at resonance with displacement (1 to 10 mm) in the Z direction (F). *Error bars represent standard deviation of the mean (n = 3).* 131

Figure 67. Schematic showing rotation directions between the sensor and detection coil (A). Changes in resonance frequency with rotation (0 to 60 degrees) in both the θ_1 (blue circles) and θ_2 (orange triangles) directions (B) Change in resonance frequency with rotation (0 to 330 degrees) in the θ_3 direction (C). Change in peak magnitude at resonance with rotation (0 to 60 degrees) in both the θ_1 (blue circles) and θ_2 (orange triangles) directions (D). *Error bars represent standard deviation of the mean (n = 3).* 132

Figure 68. Schematic showing how distance (Z) varied between the detection coil and skin mimic superficial to the sensor (A). Comparison of measured sensor resonance frequency (B) and peak magnitude at resonance (C) through 3 mm of skin mimic and air. Change in resonance frequency (D) and peak magnitude at resonance (E) with increasing Z distance. *Error bars represent standard deviation of the mean (n = 3).* 134

Figure 69. Standard linear viscoelastic model where E_1 is Young's modulus of the series spring, E_2 is the Young's modulus of the spring in parallel, and η is the viscosity of the dashpot in parallel..... 137

Figure 70. Relationship between force and strain during stress relaxation (A) and creep (B). .. 138

Figure 71. Stress-strain curve of tissue showing a toe, linear, and failure region (A). Stress-strain curve showing fast versus slow strain-rate stiffening behavior (B). Stress-strain curve showing loading and unloading behavior after 1 versus 100 cycles of loading (C)..... 140

Figure 72. Stress-strain curve comparison of tendon versus ligament. Vertical dashed lines split respective toe, linear, and failure regions. 141

Figure 73. Comparison of human (A) and cervid (B) elbow joint skeletons. (Image partially generated with the assistance of Microsoft Copilot and Google Gemini Flash 3.0) 143

Figure 74. Incision at the joint (A). Isolation of the graft tendon (B). The medial ligament to be excised (C). Distal bone tunnel drilling (D). Sutured graft construct sutured with accessory sensor (E). Detection coil placed over implanted sensor (F). 145

Figure 75. Human elbow valgus stress test (A) and flexion (B) schematics. (Image partially generated with the assistance of Google Gemini Flash 3.0) 146

Figure 76. Sensor signal and resonance frequency (A) and magnitude (B) change during joint valgus stress application *(n = 1).* 147

Figure 77. Sensor signal magnitude (A) and resonance frequency (B) change during joint flexion *(n = 1).* 148

Figure 78. Sensor resonance frequency (A) and signal magnitude at resonance (B) change during joint extension *(n = 1).* 149

Figure 79. Sensor resonance frequency response when bending joint from maximum flexion to extension and back to maximum flexion *(n = 1).* 150

Figure 80. Loosened suture in sensor deployed in ligament reconstruction. 151

Figure 81. Sensor resonance frequency measurements during application of valgus stress with knot slippage failure of the graft construct *(n = 1).* 151

Figure 82. Schematic of graft construct static loading set-up. 152

Figure 83. Sensor resonance frequency at graft static loads of 0 and 40 N. *Error bars represent standard deviation of the mean (n = 3).* 152

List of Tables

Table 1. General rehabilitation guidelines for baseball players following UCL reconstruction... 42

Table 2. Sensor iteration design comparison. 69

Table 3. Antenna design comparison. 121

Chapter 1: Introduction

Content of this chapter are adapted from:

Meyers K, Ong K (2026) "A Wireless, Passive Sensor to Monitor Intra- and Post-Operative Graft Loading in Reconstructed Medial Ulnar Collateral Ligaments." In-preparation.

Karipott S, Meyers K, Laffoon S, McGeehan M, Adams S, Riboh J, Strasser N, Gall K, Guldberg R, Ong K (2025) "Wireless Suture Button Accessory Sensor for Intra- and Post-Operative Monitoring of Suture Loading in Soft Tissue Reconstruction." Journal of Orthopaedic Experience & Innovation 6(1).

Despite advances in orthopedic surgery and rehabilitation, retear rates for surgically repaired rotator cuffs, anterior cruciate ligaments, and hand flexor tendons occur at 39.8%, 17.2%, and 9% respectively [1-3]. Graft tensioning in tendon and ligament reconstruction surgeries significantly influence operation success, yet there are no clinically available technologies that can effectively assist with measuring graft tensioning and relaxation after surgical knotting both during and following operation. After surgery, early mobilization and physical therapy are vital to restoring tendon and ligament tissue function [4]. However, rehabilitation guidelines are highly variable and lack standardization as a result of differences in patient anatomy, healing rates, and pain tolerance, making it difficult to optimize physical therapy programs for safe and effective recovery [5-7]. Inconsistent physical therapy techniques can impede tendon and ligament healing as too conservative exercise routines can cause tissue adhesion formation, limited range of motion, and delays in returning to normal levels of physical activity [8]. Conversely, too intense rehabilitation regimens can lead to tissue re-rupture, suture pullout, and suture breakage, requiring

further revision surgeries [8]. Therefore, a technology that provides tendon/ligament graft construct loading biofeedback in real-time during both intra-operative graft tensioning and physical therapy exercises could facilitate personalized, evidence-based care.

While many intra-operative technologies for measuring suture force tension before knotting have been developed to aid with graft tightening, none allow the surgeon to measure suture loading after knots are secured with final fixation or following suturing of the patient's superficial tissues. Measuring suture loading and graft security after suture knot tying as the surgeon completes graft function and range of motion testing could provide vital information on the extent of graft relaxation and complication identification. Post-operative methods for monitoring the tendon and ligament loading environment *in vivo* include imaging techniques (e.g., ultrasound, magnetic resonance imaging, and computed tomography), external sensors (e.g., superficial strain gauges, elastography, and force plates), and implantable sensors (e.g., optical and resistive strain sensors) [9, 10]. Shortcomings of existing imaging approaches include motion artifact interference, high cost of operation, limited availability, specialized user knowledge, as well as an inability to capture loading during dynamic physical therapy exercises [11]. Wearable sensors can provide estimations of tendon and ligament biomechanics based on external metrics but cannot fully capture a complex loading environment or directly detect force loading of internal sutures [11]. Numerous implantable strain and force sensors can accurately monitor tissue loading environments but are not clinically viable due to transcutaneous wire connection demands for power and data transmission, internal battery requirements, and the need to perform secondary surgeries for device removal [12-16].

To address the limitations of current tendon and ligament suture load monitoring techniques, this thesis work contributed to the long-term goal of sensitizing suture accessories that

function without the use of transcutaneous wires or batteries to allow real-time monitoring of suture load magnitude in clinical settings. The engineering objective of the thesis was to develop a wireless and battery-free implantable sensor in the form of an inductor-capacitor (LC) suture accessory to detect graft loading magnitude in ulnar collateral ligament reconstruction (UCLR). A central question guiding the objective consisted of determining if a passive, implantable LC-based suture sensor can provide quantitative and reliable measurements of graft loading under clinically relevant biomechanical conditions specific to UCLR. The overall hypothesis was that tensile loading applied to a ligament graft construct can produce measurable and repeatable changes in the resonance behavior of an integrated passive LC-based suture accessory sensor, enabling wireless detection of relative changes in graft loading under biomechanically relevant UCLR conditions. The following specific aims were conducted to develop and evaluate the sensing platform:

1.1 Aim 1: Fabricate and characterize a suture accessory sensor platform.

The objective of this aim was to develop an implantable biosensor that could transduce UCLR loading wirelessly. A suture accessory sensor was engineered with plastic materials and an embedded circuit to detect suture loading force over ranges applied during human ulnar collateral ligament reconstruction. Sensor performance (i.e., sensitivity, drift, repeatability, etc.) was determined with mechanical testing. Variations in sensor circuit and mechanical design were varied with iterations to optimize both electrical signal transmission and load sensing capability.

1.2 Aim 2: Develop wearable detection device.

In parallel with Aim 1, a wearable detection system comprising a miniaturized network analyzer, a detection coil, and a microcontroller circuit was engineered to provide information on suture loading force measured by the implanted sensor. The device remotely outputted sensor

resonance spectra and suture loads from the sensor to a custom computer app with both Bluetooth Low Energy and serial connections. Anatomically relevant transmission metrics (i.e., detection distance, alignment, tissue thickness, etc.) were assessed and improved as needed through device and antenna design. Detection device limitations were also explored with connection range, sampling rate, electrostatic discharge, and electromagnetic compatibility testing.

1.3 Aim 3: Assess sensor performance in ligament reconstruction model.

A preclinical *ex vivo* study was performed to assess sensor functionality in a joint ligament reconstruction environment. Specifically, *ex vivo* simulation of sensor deployment and function was performed with a cervid cadaver joint reconstruction surgery to evaluate the sensor's ability to detect changes in graft tension and graft failure.

Impact

Overall, this work engineered a tool to provide real-time intra-operative graft tightening information and eventual personalized suture loading biofeedback during physical therapy. Some of the broader impacts of the proposed technology include utilizing suture tension sensing to gain an improved understanding of biomechanical differences and clinical outcomes with varying graft choice, suture material, and reconstruction techniques.

Chapter 2: Background

Content of this chapter are adapted from:

Meyers K, Ong K (2026) “A Wireless, Passive Sensor to Monitor Intra- and Post-Operative Graft Loading in Reconstructed Medial Ulnar Collateral Ligaments.” In-preparation.

Karipott S, Meyers K, Laffoon S, McGeehan M, Adams S, Riboh J, Strasser N, Gall K, Guldberg R, Ong K (2025) “Wireless Suture Button Accessory Sensor for Intra- and Post-Operative Monitoring of Suture Loading in Soft Tissue Reconstruction.” Journal of Orthopaedic Experience & Innovation 6(1).

Meyers K, Ong K (2022) “Suture Sensor to Monitor Tensile Stress in Tendon and Ligaments During Physical Therapy for Sports Medicine Applications.” IEEE Sensors Journal 22(19).

2.1 Ulnar Collateral Ligament Reconstruction (UCLR)

2.1.1 UCL Structure & Function

On the medial side of the human elbow joint, the ulnar collateral ligament (UCL) complex connects the ulna to the medial epicondyle of the humerus (Figure 1). The UCL is composed of 3 bands: (anterior, posterior, and transverse) and resists valgus and extension stress from 70° to 120° of elbow flexion [17]. Primary resistance to valgus and rotational stresses is provided by the anterior band [17]. Adjacent to the UCL, many muscles cross the elbow joint to drive arm flexion and extension while the ulnar nerve runs behind the medial epicondyle of the humerus.

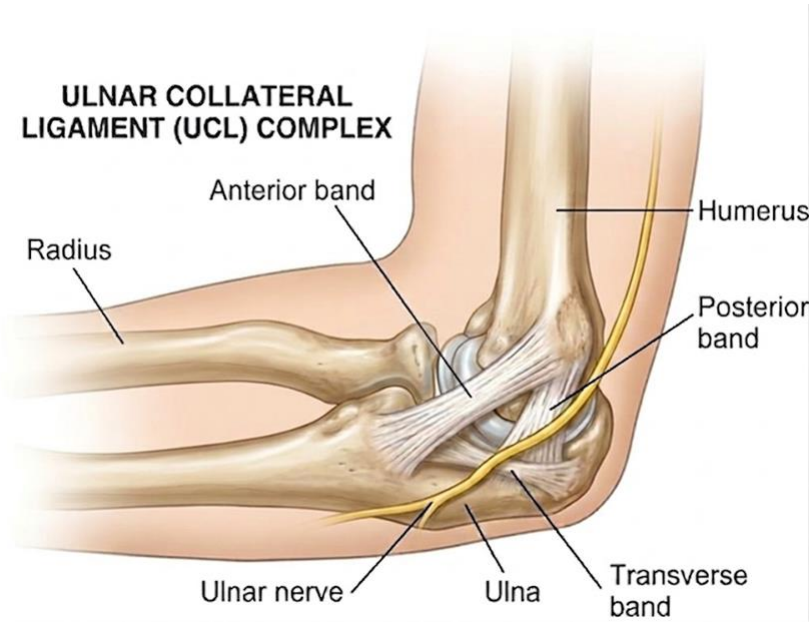

Figure 1. Anatomy of the human elbow joint showing the UCL complex (Image generated with the assistance of Google Gemini Flash 3.0).

2.1.2 UCL Reconstruction Occurrence and Projected Growth in Baseball

In overhead throwing athletes, the anterior bundle of the ulnar collateral ligament (UCL) in the elbow can tear when resisting heightened valgus forces and rotational stresses during the early acceleration phase of the throwing motion (Figure 2) [17]. Ulnar collateral ligament reconstruction (UCLR), also known as “Tommy John surgery”, has been on the rise among both youth and professional baseball pitchers over the past couple of decades to treat full UCL tears [18]. In 2024, 41.1% of active Major League Baseball (MLB) pitchers had undergone UCLR at least once in their career [19]. Youth account for the greatest share of UCLR at 67.4% in the 16- to 20- year old age group with UCLR increasing at a rate of 9.12% per year for the 15- to 19-year-old group [20, 21]. Overuse with year-round training and an increase in pitching velocity and spin have been attributed to the rise in UCLR in baseball pitchers [22]. To help address the increase in UCL injuries, pitching guidelines dictating pitch counts and periods of rest were created, but youth

pitch recommendations are not always enforced [23]. Although UCLR is widely regarded as a successful procedure for repairing the elbow joint, return-to-play (RTP) rates range from 80 to 97% in MLB pitchers with only 57% to 87% of players returning to the same level of play [24, 25]. In adolescent baseball pitchers RTP rates are reported to be near 84% [26]. Furthermore, 13.2 to 15% of MLB pitchers undergo a second revision UCLR surgery at roughly 3-5 years after initial reconstruction [27, 28]. Surgical complication rates increased with revision UCLR and RTP rate at the same level of performance was only 55% to 70% in MLB pitchers [29].

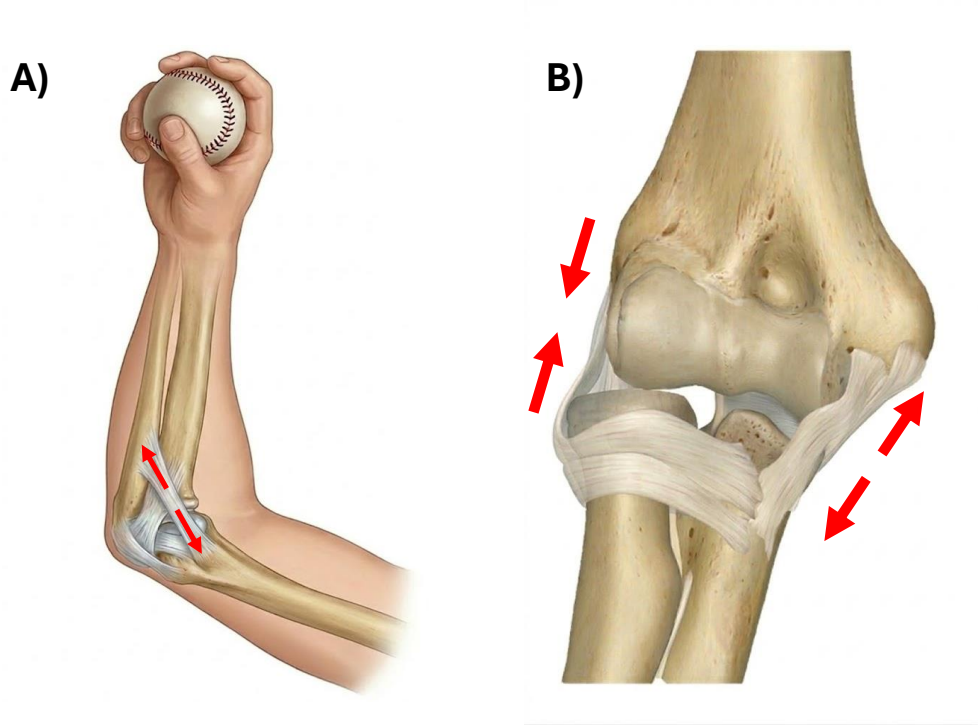

Figure 2. Early acceleration phase of a baseball pitch loads the UCL in tension (red arrows) (A). Loading of ligaments in the human elbow under valgus stress (B). (Images generated with the assistance of Google Gemini Flash 3.0)

2.1.3 UCL Surgical Reconstruction Procedure

Since ligament tissues have restricted regeneration capabilities due to limited vascularity, surgical repair or reconstruction is often required for UCL rupture and tear injuries (Figure 3A) [30]. Numerous UCLR techniques have been developed since the 1970s including Jobe, Docking, and Suspensory. Specifically, the thesis project focused on UCLR Suspensory methods with suture accessories. During surgical reconstruction, the ruptured UCL is usually replaced with a graft composed of tendon autograph. Typically, a hamstring tendon or palmaris longus tendon is harvested from the patient to be utilized in the UCLR graft. At the elbow joint an incision is made to expose the damaged UCL whereafter bone tunnels are drilled into the sublime tubercle of the ulna and medial epicondyle of the humerus (Figure 3B). The graft is then passed through the bone tunnels and tensioned (Figure 3C). The graft is secured in place with sutures and suture accessories (e.g., suture button) are optional to facilitate fixation (Figure 3D). The ulnar nerve may also be transposed away from the reconstruction site to prevent post-operative neurological complications. Overall, the UCLR procedure lasts between 60-90 minutes in an outpatient setting.

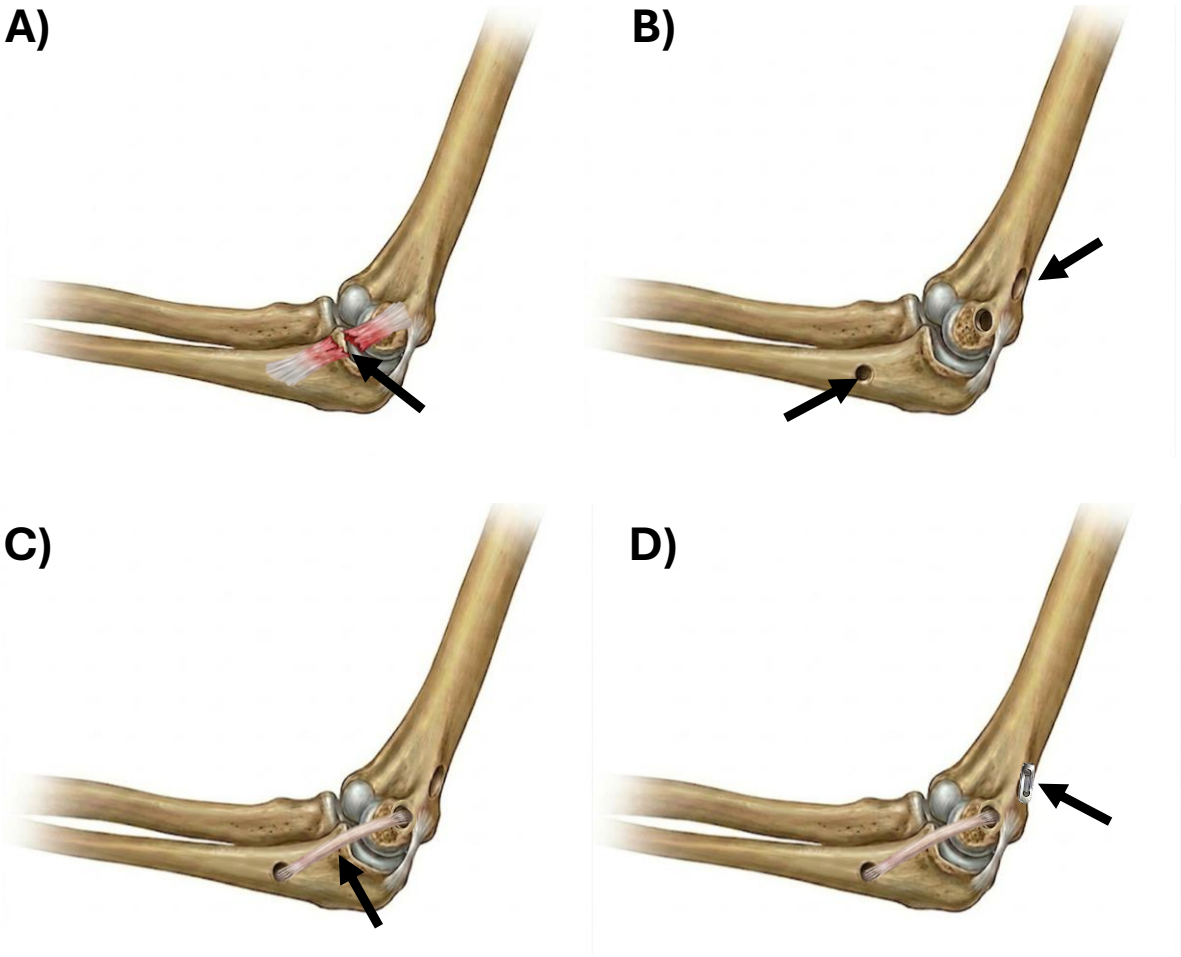

Figure 3. During a UCLR, the ruptured anterior UCL (A) is replaced to restore joint stability. Bone tunnels are drilled into the ulna and medial epicondyle of the humerus (B). Whereafter a graft is threaded through the ulnar bone tunnels into the humeral bone (C). The graft can be fixed with a suture button (D). Figure represents the proximal single-tunnel suspensory fixation technique for UCLR. (Images generated partially with the assistance of Google Gemini Flash 3.0)

2.1.4 Rehabilitation of Reconstructed UCL

Early mobilization during post-operative physical therapy is vital to restoring UCL function during a 9-12 month rehabilitation period [31]. Immediately following UCLR surgery, the elbow is immobilized with a brace (Figure 4). Physical therapy guidelines for UCLR typically

cover 9-12 months until full recovery (Table 1). The first 2 weeks after UCLR, muscles and joints near the elbow are exercised to prevent atrophy as the elbow joint heals and inflammation subsides. From 2 to 6 weeks following reconstruction, gradual elbow flexion and extension is introduced below full range of motion (e.g., 0 to 125 degrees). Approximately 6 weeks after surgery full range of motion (e.g., 0 to 145-150 degrees) exercises are implemented with a focus on strengthening [32]. Light throwing activities are implemented 3 months following UCLR with return to competitive throwing approximately a year after surgery.

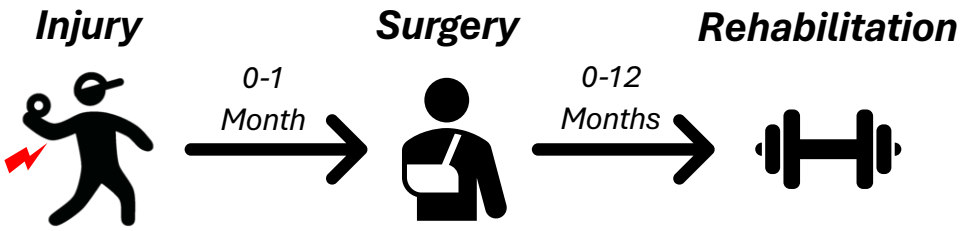

Figure 4. Schematic outlining injury, surgery, and rehabilitation phases of UCLR. For full UCL tears, UCLR is performed 0-1 month following injury while post-operative rehabilitation lasts up to 12 months for full recovery.

Table 1. General rehabilitation guidelines for baseball players following UCL reconstruction.

Phase	Rehabilitation Regime
0-6 Weeks	Immobilization & Gradual Flexion/Extension
6-12 Weeks	Full ROM Exercises & Strengthening
3-6 Months	Light Throwing
6-12 Months	Build Up to Throwing Regularly

2.1.5 Importance of UCLR Graft Tension & Loading

When surgical repair is utilized in UCLR, optimal graft tension during the procedure ranges from 20 to 40 N when evaluated with cadaver assessments [33]. Some technologies exist for monitoring suture tension when performing surgery, but none are clinically used to measure loading after final graft fixation [34-36]. Correct graft tensioning during UCLR is paramount as under-tensioning can lead to join laxity and graft integration failure while over-tensioning can cause restricted range of motion and graft breakdown which may require revision surgery. Early mobilization during post-operative physical therapy is vital to restoring UCL function during a 9-12 month rehabilitation period [31]. However, no universal or standardized UCLR rehabilitation guidelines have been established partially due to variability in patient anatomy and healing rates [31]. As a result, many rehabilitation treatment decisions rely on qualitative factors such as tissue swelling or patient pain tolerance, creating irregularities in recovery care. Inconsistent physical therapy regimes can be detrimental to repair as overly relaxed routines can lead to tissue adhesion formations and limited range of motion whereas excessively intense programs can cause re-rupture of tissue, suture pullout through tissue, and suture breakage [37-40]. Therefore, a device that could provide graft loading biofeedback in real-time during physical therapy exercises could facilitate personalized, evidence-based rehabilitation therapy. Individualized data provided by a graft load sensing platform could reduce speculation around RTP decisions and help establish guidance for rehabilitation exercise frequency, duration, and intensity to optimize recovery.

2.2 Current Methods for Estimating UCL Loading

While many intra-operative technologies for measuring suture force tension before graft fixation have been developed to aid with graft tightening, none allow the surgeon to measure suture loading after final graft fixation [41, 42]. Current methods for estimating graft placement,

tensioning, and subsequent relaxation rely on cadaver models and computer simulations [43, 44]. Cadaver model testing requires complex and costly equipment and can only provide generalized, non-patient specific information about surgical methods. Computer models can utilize patient-specific anatomy but are limited by material and boundary condition assumptions and cannot fully capture *in vivo* graft loading behavior.

Current methods to quantify or estimate graft loading and post-operative complications *in vivo* include imaging techniques (e.g., ultrasound, magnetic resonance imaging, and computed tomography), external sensors (e.g., superficial strain gauges, elastography, and force plates), and implantable sensors (e.g., optical and resistive strain sensors) [9, 10]. Limitations to imaging approaches include motion artifact interference, high cost of operation, limited availability, specialized user knowledge, as well as an inability to capture loading during dynamic physical therapy exercises [11]. Wearable sensors can provide estimations of tendon and ligament biomechanics based on external metrics but cannot fully capture a complex loading environment or directly detect force loading of internal structures [11]. Numerous implantable strain and force sensors can accurately monitor tissue loading environments in the laboratory but are not clinically viable currently due to transcutaneous wire connection demands for power and data transmission or internal battery requirements, limiting their administration to superficial skin and subcutaneous applications [12-16]. In addition, some suture loading sensors require extensive manufacturing modifications to the diverse number of suture types available on the market, increasing barriers to clinical adoption [45, 46].

2.3 Inductor-Capacitor (LC) Sensors in Medical Applications

One method to overcoming the limitations of wired and/or battery powered implantable sensors includes passive sensors. Since passive sensors are operated by an external interrogator

and do not require an internal power supply (i.e., batteries), several design aspects can be enhanced. For example, the footprint or size of the sensor can be reduced since no batteries are present. Further, the duration of implantation can last longer when not limited by a battery lifetime. The cost of sensor materials and manufacturing can be reduced via the absence of batteries and power management components (e.g., voltage regulators, filters, etc.). Finally, the safety of the sensing platform can be improved by eliminating the opportunity for battery accidental toxic leakage and heat generation [47-49].

A subcategory of passive sensors includes chipless inductive-capacitor (LC) sensors which are activated with an electromagnetic field and emit a secondary field that can be measured remotely. One example of an LC sensor application in the medical field includes radiofrequency identification (RFID) used for medical supply tracing. Implantable LC sensors are utilized in clinically available pulmonary artery pressure monitoring systems (CardioMEMS^{TM}) to assess heart failure progression [50]. Further, many other LC sensor designs are being developed and researched for applications in wearable sweat monitors and implantable intracranial pressure measurement systems [51, 52].

2.3.1 LC Sensor Theory

Electromagnetic-based passive sensors are typically made of a simple electrical resonance circuit consisting of an electrical inductor (L) and capacitor (C). A static or variable resistor (R) may be deliberately added to an LC circuit to form a RCL circuit, but inherent parasitic resistance (R_p) will still be present in a LC circuit. The parasitic resistance (R_p) of a circuit trace can be calculated as:

$$R_p = \rho \frac{l}{A} \tag{1}$$

Where ρ is the resistivity of the conducting metal (typically 1.68 x 10^{-6} Ωm for copper at room temperature), l is the length of trace, and A is the cross-sectional area of the trace. Interrogating a planar inductor with varying AC frequency also impacts the impedance of the circuit traces. For example, at higher frequencies (above 100 kHz), the skin effect increases trace impedance since current tends to flow near the perimeter of the trace due to the formation of eddy currents near the center. Additionally, proximity effects from neighboring traces induce eddy currents, further increasing trace impedance. Equations have been proposed to estimate frequency-dependent skin and proximity effects while optimizing planar inductor design to reduce AC resistance [53]. Generally, as frequency increases above 100 kHz, the skin and proximity effects increase and become more pronounced as current density concentrates near the edges of the conductor.

In an LC circuit, remote transfer of power and data can be achieved through mutual inductance (M) between the sensor's inductor coil (L_s) and an external detection device coil (L_d) (Figure 5). Specifically, the detection device emits a frequency varying AC signal and measures reflected signals (e.g., S_{11} parameter comparing reflected and incident power) to generate a sensor resonance spectra. Various parameters on the resonance spectra (i.e., resonance frequency, quality factor, impedance) can be tracked to measure a change in the sensor circuit.

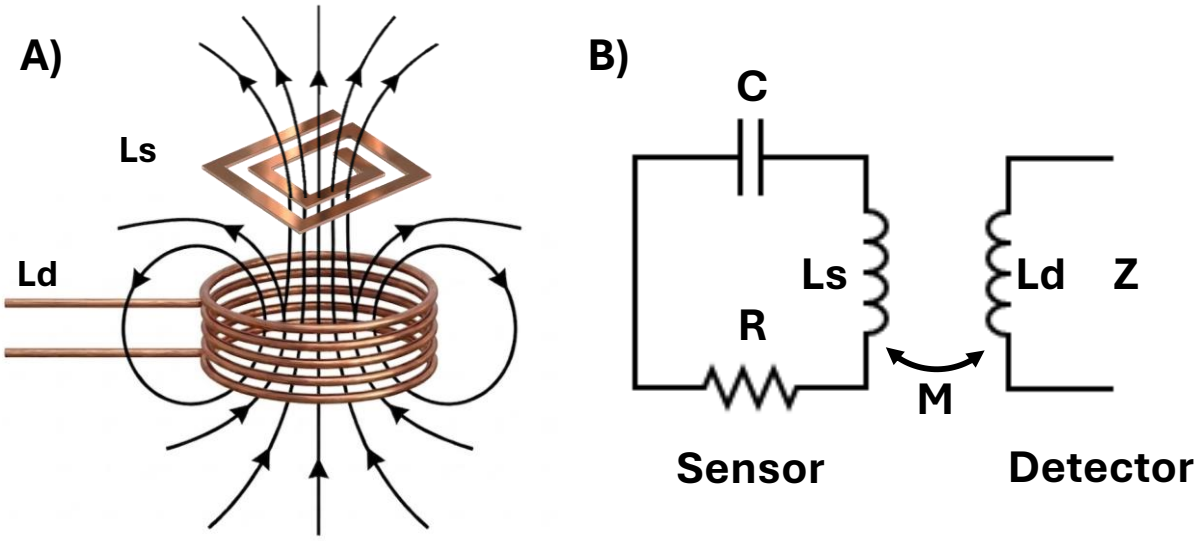

Figure 5. Electromagnetic coupling between inductors of a sensor (L_s) and detection coil (L_d) (A). Circuit diagram of LCR sensor coupled to a detection device where R is resistance, C is the capacitance of the capacitor, L_s is inductance of the sensor coil, L_d is inductance of the detection coil, and Z is measured impedance (B). (Images partially generated with the assistance of Google Gemini Flash 3.0)

2.3.2 Electrical Resonance

In the presence of an electromagnetic field, LC sensors undergo resonance when impedance is minimized resulting in a maximized returned signal (Figure 6). Since the behavior of capacitors and inductors are frequency dependent, impedance (Z) is determined by resistance (R), capacitive reactance (X_C), and inductive reactance (X_L) as follows:

$$X_C = \frac{1}{2\pi f C} \tag{2}$$

$$X_L = 2\pi f L \tag{3}$$

$$Z = \sqrt{R^2 + (X_L - X_C)^2} \tag{4}$$

When $X_L > X_C$, the circuit is inductive (voltage leads current) and when $X_C > X_L$ the circuit is capacitive (current leads voltage). Resonance occurs when $X_L = X_C$ and total impedance of the circuit equals the resistance value (Z = R). Resonance frequency (f_r) is dependent on the inductance (L) and capacitance (C) of a circuit as follows:

$$f_r = \frac{1}{2\pi\sqrt{LC}} \tag{5}$$

As inductance or capacitance increases, resonance frequency decreases and vice versa. Therefore, an LC circuit designed to modify inductance or capacitance in response to a stimulus can act as a sensor via transducing measured changes in resonance frequency.

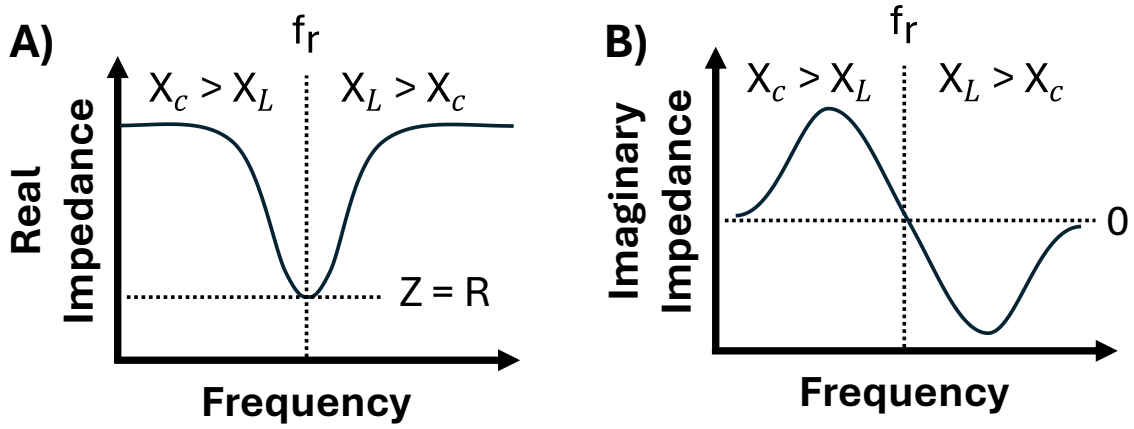

Figure 6. Real (A) and imaginary (B) impedance spectra where X_C is capacitive reactance, X_L is inductive reactance, Z is impedance, R is resistance, and f_r is resonance frequency.

2.3.3 Quality Factor

Quality factor (Q factor) is a dimensionless parameter that quantifies the sharpness of a resonance spectra (Figure 7). Q factor is defined by the ratio between resonance frequency (f_r) and half power bandwidth (B) (i.e., the bandwidth between the two frequencies with signal strength equal to 70.7 % of the resonance amplitude) and defined as follows [54]:

$$Q = \frac{f_r}{B} \tag{6}$$

Q factor is also influenced by inductance (L), capacitance (C), resistance (R) as follows [54]:

$$Q = \frac{1}{R}\sqrt{\frac{L}{C}} \tag{7}$$

Since Q factor is inversely related to resistance, increasing resistance drops Q factor and vice versa. Therefore, an LC circuit designed to modify resistance in response to a stimulus can act as a sensor via transducing measured changes in Q factor. Further, with a high Q factor, the circuit resonance spectrum has a narrower bandwidth and is more sensitive to alterations in resonance frequency for sensors based on measuring change in resonance frequency.

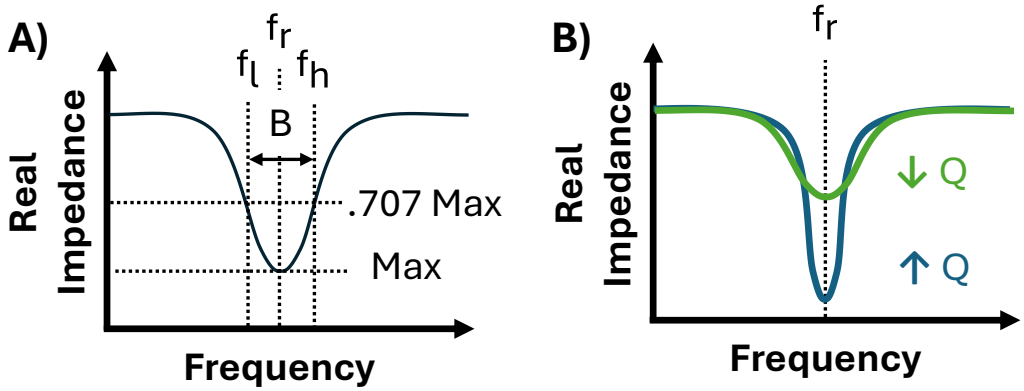

Figure 7. Resonance spectra showing quality factor metric determination (A) and the impact of quality factor on resonance spectra shape (B) where f_l is the lower frequency with signal strength equal to 70.7 % of the resonance amplitude, f_h is the higher frequency with signal strength equal to 70.7 % of the resonance amplitude, B is bandwidth, Q is quality factor, and f_r is resonance frequency.

2.3.4 Radiofrequency Transmission Through Tissues

When measuring implantable LC sensor signals, attenuation occurs with radiofrequency energy absorption or reflection by tissues. Since tissues are largely composed of water, the absorption of radiofrequency energy by biological tissue can be approximated with the absorption spectrum of water [55]. As a result, signal attenuation through tissue can be minimized by using radiofrequencies below 100 MHz. Electromagnetic safety guidelines have been developed to regulate the amount of thermal energy absorbed by tissue during radiofrequency exposure. The specific absorption rate (SAR) quantifies the rate of energy absorption by a unit of mass and is quantified as follows:

$$SAR = \frac{\sigma |E|^2}{\rho} \tag{8}$$

Where σ is the electrical conductivity of the tissue, E is the strength of the electric field, and ρ is the density of the tissue. SAR is measured in W/kg of tissue and limits are set based on body location (e.g., head, torso, etc.). Therefore, it is important to design LC sensor detection systems that are powerful enough to interrogate and record implantable sensor signals through tissues while limiting radiofrequency heating.

2.3.5 Electromagnetic Coupling Considerations

Mutual inductance (M) describes the magnetic flux linkage between inductors. With a transmitter coil, only a portion of generated magnetic flux is transmitted to the receiver coil. As a result, the efficiency of can be described by coupling factor (k). Coupling factor is a dimensionless unit between 0 and 1, where 1 represents perfect coupling between the transmitter and receiver coils. The distance, alignment, and orientation between transmitter and receiver coils impacts the

value of k. Mutual inductance (measured in H) is calculated based on coupling factor (k), as follows:

$$M = k\sqrt{L_s \cdot L_d} \tag{9}$$

Where L_s is inductance of the sensor coil (receiver) and L_d is inductance of the detection coil (transmitter). Generally, coupling factor is reduced by increasing distance between coils, misaligning of coils/displacing coils, or disoriented coils. Further the relative size and shape of coils impacts coupling factor. For example, a smaller receiver coil (relative to a transmitter coil) only captures a fraction of the magnetic flux produced by a transmitter coil. The magnetic permeability of the material composition between the transmitter and receiver coil also influences coupling factor. For example, a material with high magnetic permeability (e.g., ferrite) can help concentrate magnetic flux.

Regulatory standards such as IEC 60601 outline specifications related to electromagnetic interference (EMI), the susceptibility of the device to external electromagnetic interference or noise, and electromagnetic compatibility (EMC), the ability of the device to function without causing EMI to other instrumentation. Combinations of shielding and filtering methods are employed in device design to reduce EMI and improve EMC. Certain frequency operating ranges were also set aside via Industrial, Scientific, and Medical (ISM) bandwidths to partially address EMI and EMC concerns with telecommunication devices.

2.3.6 Reflected Impedance Measurements

When measuring LC sensor signals, a detection device transmits a frequency varying AC signal through a detection antenna coil and records reflected waveforms (Figure 8A). Reflected

impedance (Z_d) depends on the impedance of the detection coil and sensor (Z_s) as well as the mutual inductance (M) between the coils as follows:

$$Z_d = R_d + 2\pi f L_d + \frac{(2\pi f M)^2}{Z_s} \quad (10)$$

Where R_d is parasitic resistance of the detection coil, L_d is inductance of the detection coil, and f is frequency measured in Hz. The impedance of the sensor (Z_s) can be calculated as follows:

$$Z_s = R_s + 2\pi f L_s + \frac{1}{2\pi f C_s} \quad (11)$$

Where R_s is parasitic resistance of the sensor, C_s is the capacitance of the sensor, L_s is inductance of the sensor coil. At resonance, reflected impedance (Z_d) is highest when sensor impedance (Z_s) is lowest (Figure 8B). A vector network analyzer can be utilized to measure LC sensor reflection signals. Vector network analyzers measure and compare reflected voltage (V_{ref}) to incident voltage (V_{fwd}) to calculate a reflection coefficient (S_{11}) as follows:

$$S_{11} = \frac{V_{ref}}{V_{fwd}} = \frac{Z_d - Z_0}{Z_d + Z_0} \quad (12)$$

Where Z_0 is the characteristic impedance of the vector network analyzer. The input impedance of the vector network analyzer (Z_0) is typically 50 **Ω** (i.e., $Z_0 = 50$ **Ω**). Reflection coefficient is value between -1 and 1, where a value of 0 represents no reflected energy (i.e., all energy is transmitted when $Z_d = Z_0$). A reflection coefficient of 1 represents infinite Z_d (i.e., open condition) where all energy is reflected while a reflection coefficient of -1 represents zero Z_d (i.e., short condition) where all energy is reflected 180° out of phase with the incident wave. When $Z_d < Z_0$ or the polarity of the reflected wave is opposite of the incident wave (i.e., phase inversion of

the reflected voltage), reflection coefficient is negative (Figure 8C). Sometimes reflection coefficients are expressed in decibels on a logarithmic scale as follows:

$$S_{11}(\mathrm{dB}) = 20\log_{10}|S_{11}| \tag{13}$$

Reflected impedance can be calculated from reflection coefficients by rearranging Equation 12 as follows:

$$Z_d = Z_0\frac{1 + S_{11}}{1 - S_{11}} \tag{14}$$

Background subtraction can be utilized to partially remove the impact of detection coil impedance from measured signals. However, mutual inductance between the detection coil and sensor is still dependent on the inductance of the detection coil according to Equation 9.

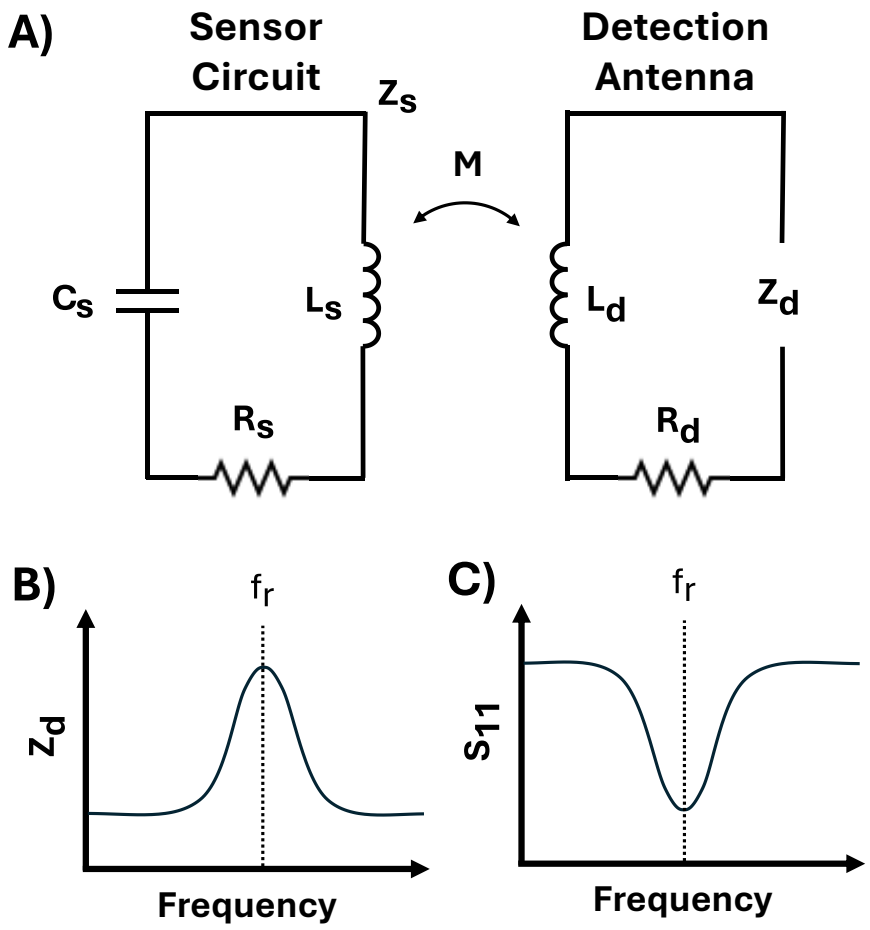

Figure 8. Circuit diagram of LC sensor coupled to a detection device where R_s is parasitic resistance of the sensor, C_s is the capacitance of the sensor, L_s is inductance of the sensor coil, Z_d, is the impedance of the sensor circuit, M is mutual inductance, L_d is inductance of the detection coil, R_d is parasitic resistance of the detection coil, and Z_d is impedance measured by the detection coil (A). Reflected impedance spectra where Z_d is the impedance measured by the detection coil and f_r is resonance frequency (B). Reflection coefficient (S_{11}) spectra where f_r is resonance frequency (C).

2.4 Planar Inductors as LC Sensors

Since planar inductors have parasitic capacitance among the traces that make up the inductor turns, they can act as LC sensor circuits. Advantages of utilizing planar inductor coils as LC circuits include limiting implantable sensor footprint size while reducing manufacturing complexity. However, tradeoffs in sensitivity and selectivity may impact LC sensor design when utilizing a planar inductor approach.

2.4.1 Equivalent Circuit

Planar inductor coils can be designed according to various shapes (e.g., square, spiral, rectangular, rounded rectangular, etc.). Trace width (w) and spacing (s) impact the inductance and parasitic capacitance of the coil as well as parasitic resistance (Figure 9). Solenoid coil inductance can be calculated as follows:

$$L = \frac{\mu N^2 A}{l} \tag{15}$$

Where μ is permeability of the core material (i.e., material capacity to magnetize in response to a magnetic field), N is turn number, A is coil cross-sectional area, and l is coil length. Conversely, inductance value equations are more complex when accounting for the mutual inductance between each turn as well as variations in planar inductor shapes. Some inductance equations have been proposed based on for varying shape planar inductor coils (e.g., Modified Wheeler), but numerical simulation techniques are often utilized to estimate the inductance of planar inductor coils [56]. Generally, increasing planar inductor turns results in increased inductance.

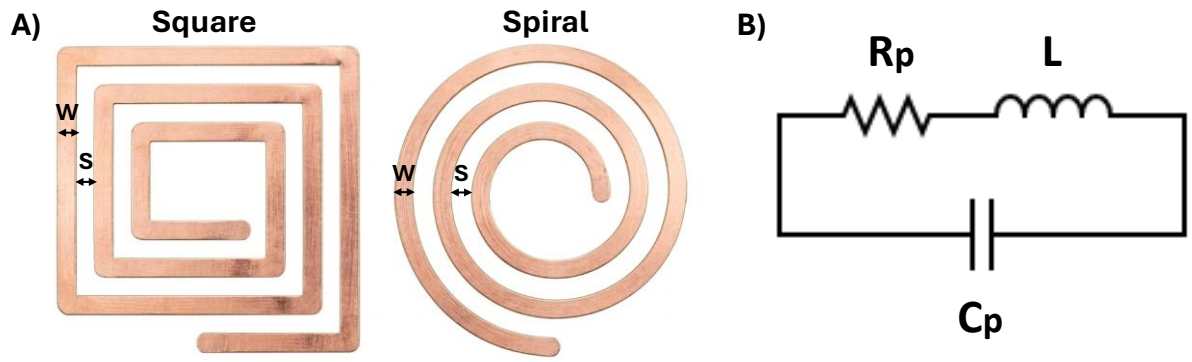

Figure 9. Planar inductor square and spiral inductor design examples where trace width (w) and spacing (s) are visualized (A). Equivalent circuit of planar inductor coil with parasitic resistance and capacitance (B). (Images partially generated with the assistance of Google Gemini Flash 3.0)

Complexity also exists in determining the inherent parasitic capacitance among turns in a planar inductor coil as fringe capacitance is present between both adjacent and distant traces (Figure 10). However, the capacitance (C) equation between two parallel plates is determined by the following equation:

$$C_p = \frac{\varepsilon A}{d} \tag{16}$$

Where ε is the permittivity of the dielectric (i.e., material capacity to polarize in the presence of an electric field), d is the distance between the plates, and A is the area of plate overlap. Generally, parasitic capacitance increases with increasing planar inductor turns and trace density as more coplanar trace area overlap occurs.

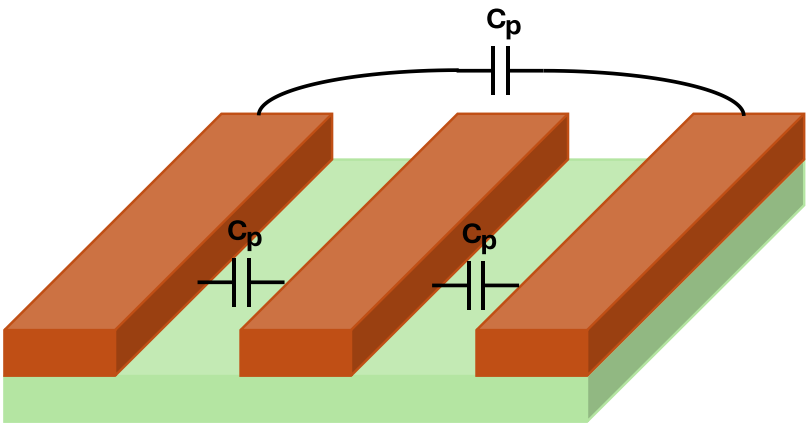

Figure 10. Parasitic capacitance (C_p) among planar inductor traces showing capacitance between coplanar (on the same layer) traces.

Parasitic resistance increases with increasing trace length (e.g., increasing planar inductor turn number or area) according to Equation 1 and reduces sensor signal quality factor according to Equation 7. However, increasing trace thickness can help offset increases in parasitic resistance.

2.4.2 Stacking Planar Inductors

Miniaturizing planar inductors for LC sensors in implantable devices is desired but presents significant sensor signal transmission challenges. Generally, when planar inductor size is decreased, resonance frequency increases according to Equation 5 with reductions in turn number and therefore lowered inductance and capacitance. Reducing trace width also increases parasitic resistance and therefore diminishes signal quality factor. In an effort to maintain lower resonance frequencies while reducing sensor size for implantable devices planar inductor stacking with multilayer circuit boards can be designed (Figure 11A). In multilayer planar inductors, mutual inductance is added between inductor layers in equivalent circuits (Figure 11B). In LC sensor applications, multilayer inductors also have mutual inductance between each inductor layer and

the detection coil. Stacking connected inductors onto multiple layers reduces resonance frequency by increasing inductance since inductors add in series as follows:

$$L_T = L_1 + L_2 + \cdots + L_n \tag{17}$$

Where L_T is total inductance and L_n are inductances of n number of inductors.

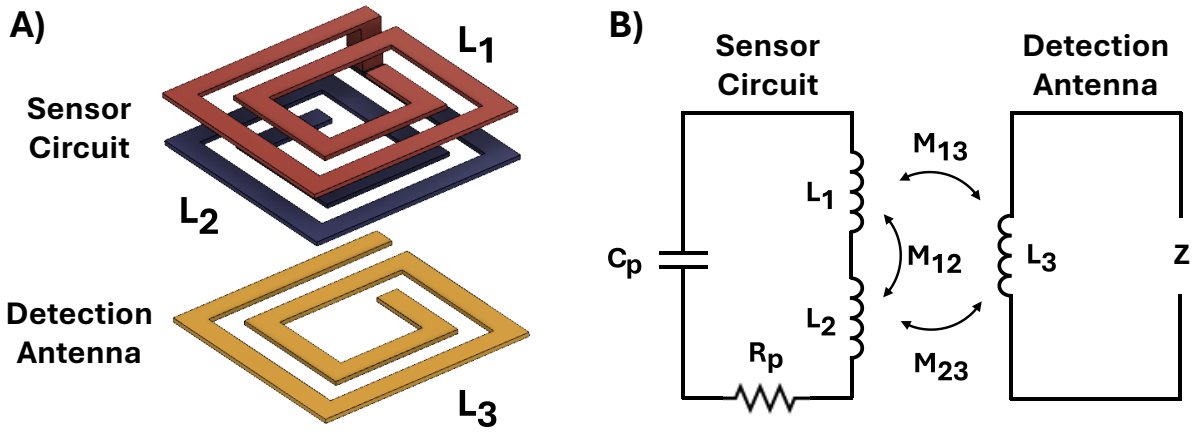

Figure 11. Simplified representation of a 2-layer inductor sensor circuit and detection antenna (A). Circuit diagram of the suture accessory sensor coupled to a detection antenna (parasitic resistance not shown) (B). L_1 is inductance of the top sensor coil, L_2 is inductance of the bottom sensor coil, L_3 is inductance of the detection coil, C_p is parasitic capacitance of the sensor circuit, M_{13} is mutual inductance between the top sensor coil and the detection coil, M_{12} is mutual inductance between the top sensor coil and the bottom sensor coil, M_{23} is mutual inductance between the bottom sensor coil and the detection coil, and Z is measured impedance.

With multilayer inductors, parasitic capacitance increases with additional inductors. Series planar multilayer inductors provide parasitic capacitance among stacked planar inductor traces between both board layers and coplanar (on the same layer) traces (Figure 12). The parasitic capacitance of multilayer planar inductors can also be increased by reducing the distance between the stacked inductor layers (i.e., decreasing thickness of circuit substrate) according to Equation

16. Stacking connected inductors onto multiple layers reduces resonance frequency by increasing capacitance since capacitors add in parallel as follows

$$C_T = C_1 + C_2 + \cdots + C_n \tag{18}$$

Where C_T is total capacitance and C_n are capacitances of n number of capacitors.

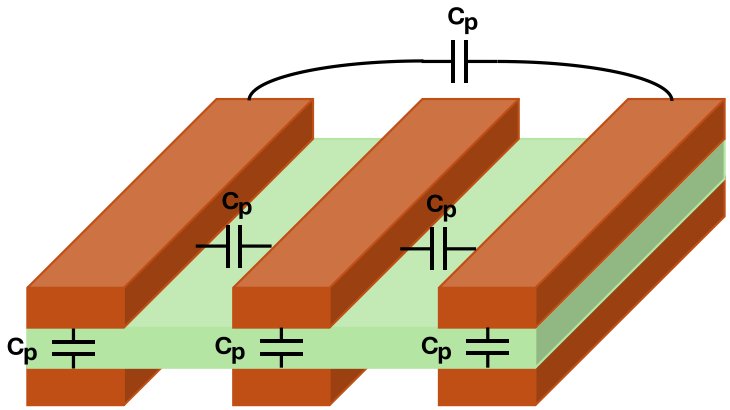

Figure 12. Parasitic capacitance (C_p) among stacked planar inductor traces showing capacitance between both board layers and coplanar (on the same layer) traces.

The parasitic resistance of multilayer planar inductor coils increases with additional inductors as resistors add in series as follows:

$$R_T = R_1 + R_2 + \cdots + R_n \tag{19}$$

Where R_T is total resistance and R_n are resistances of n number of resistors. Increasing parasitic resistance of the planar inductor sensor reduces signal quality factor according to Equation 7. However, increasing planar inductor trace thickness can help mitigate reductions in signal quality factor by reducing parasitic resistance.

2.4.3 Bending Planar Inductors

A planar inductor coil may be fabricated on a flexible substrate (e.g., polyimide) where it

can undergo bending in response to mechanical stimulus. When a planar inductor coil undergoes bending, electromagnetic field interactions within the planar inductor sensor change as well as the mutual inductance behavior with a coupled detection coil. Therefore, resonance signal alterations due to bending depend on both the planar inductor sensor and detection coil designs as well as bending direction and location or concentration on the circuit pattern.

As a planar inductor coil is flexed, the distance between circuit traces decreases due to bending of the sensor, increasing the parasitic capacitance of the circuit as described in Equation 16 (Figure 13). Increasing capacitance reduces the measured resonance frequency of the circuit according to Equation 5.

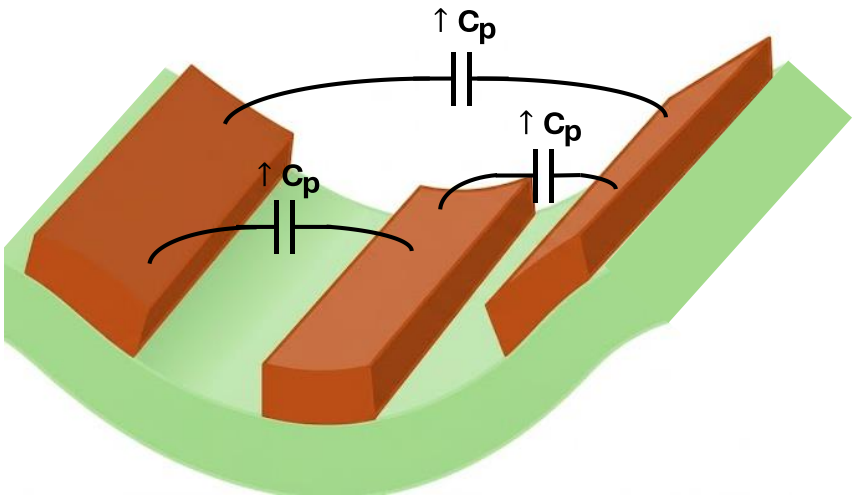

Figure 13. Bending of planar inductor traces resulting in a decreased distance between traces and therefore increased parasitic capacitance. (Images partially generated with the assistance of Google Gemini Flash 3.0)

Additionally, bending of a planar inductor reduces inductance as bending reduces magnetic field distribution [57]. Reducing inductance increases the measured resonance frequency of the circuit according to Equation 5. A reduction in magnetic field distribution also impacts the mutual inductance between the planar inductor and a detection coil. Specifically, since coupling factor is

reduced based on increasing distance and altering geometric parameters, bending can reduce mutual inductance according to Equation 9 leading to a reduction in measured signal strength. Due to opposing resonance frequency responses with bending, inductors and capacitors partially cancel individual effects on the resonant frequency of a planar inductor.

2.4.4 Planar Inductor LC Sensor Design Environmental Considerations

When designing a planar inductor LC sensor, circuit insulation and integration into the sensor structure are paramount. The electrical permittivity of the materials used to isolate the sensor circuit and form the sensor body structure impact parasitic capacitance and therefore resonance behavior of the circuit. Since the behavior of LC sensor signals are susceptible to humidity and moisture interference due to alterations in permittivity (i.e., dielectric of water is significantly higher than that of air), thickness of insulation materials can also determine how well sensor responses are maintained in a humid environment or when implanted into biological tissues. Further, temperature influences the behavior of LC sensor signals via thermal expansion and thermal-dependent alterations of permittivity and permeability. For example, parasitic resistance increases with temperature, reducing signal quality factor. It is also challenging to use planar inductor coils near nonferromagnetic metals as high eddy current generation significantly impacts inductance.

Chapter 3: Engineering a Force Detecting LC Sensor

Content of this chapter are adapted from:

Meyers K, Ong K (2026) “A Wireless, Passive Sensor to Monitor Intra- and Post-Operative Graft Loading in Reconstructed Medial Ulnar Collateral Ligaments.” In-preparation.

Author contributions

Conceptualization: KM, KO

Data Collection and Analysis: KM

Interpretation: KM, KO

Writing and Editing: KM, KO

Karipott S, Meyers K, Laffoon S, McGeehan M, Adams S, Riboh, J, Strasser N, Gall K, Guldberg R, Ong K (2025) “Wireless Suture Button Accessory Sensor for Intra- and Post-Operative Monitoring of Suture Loading in Soft Tissue Reconstruction.” Journal of Orthopaedic Experience & Innovation 6(1).

Author contributions

Conceptualization: SK, KG

Data Collection and Analysis: SK, KM

Interpretation: SK, KM, KO, SL, MM, SA, JR, NS, KG, RG

Writing and Editing: KM, SK, KO, SL, MM, SA, JR, NS, KG, RG

Meyers K, Ong K (2022) “Suture Sensor to Monitor Tensile Stress in Tendon and Ligaments During Physical Therapy for Sports Medicine Applications.” IEEE Sensors Journal 22(19).

Author contributions

Conceptualization: KM, KO

Data Collection and Analysis: KM

Interpretation: KM, KO

Writing and Editing: KM, KO

3.1 Introduction

One approach to generating clinically feasible implantable suture loading sensors includes developing wireless biosensors integrated into the design of suture accessories (i.e., suture anchors, button, clips, and pledgets) utilized in some iterations of UCLR [58-60]. Advantages of sensitizing suture accessories consist of preserving surgical workflow without influencing operation time and suture selection preferences which increases the likelihood of clinical adoption by surgeons. The following work focuses on the development of an implantable biosensor incorporated into a suture accessory that can perform real-time monitoring of UCLR graft loading. To increase the safety and decrease the size of the sensor, the device was developed to function passively so no internal power sources (i.e., batteries) are required. Unlike many other suture loading sensors, this device does not require transcutaneous wire connections, so patient movement is not restricted during physical therapy exercises and the possibility of infection from skin breakage by wires is eliminated. Instead, remote coupling with the implantable sensor was achieved through an external detection device that can be employed during surgery or worn by the patient during physical therapy

exercises. In order to preserve suture selection preferences and surgical operation workflow, the technology is also designed to be utilized with existing sutures already available on the market for UCLR. Design requirements and criteria for the sensor were gathered from literature, surgeons, physical therapists, consultants, and industry standards. Overall, this chapter focuses on determining if LC sensor designs can transduce changes in loading force via alterations in measured sensor resonance frequency according to calibrated transfer functions.

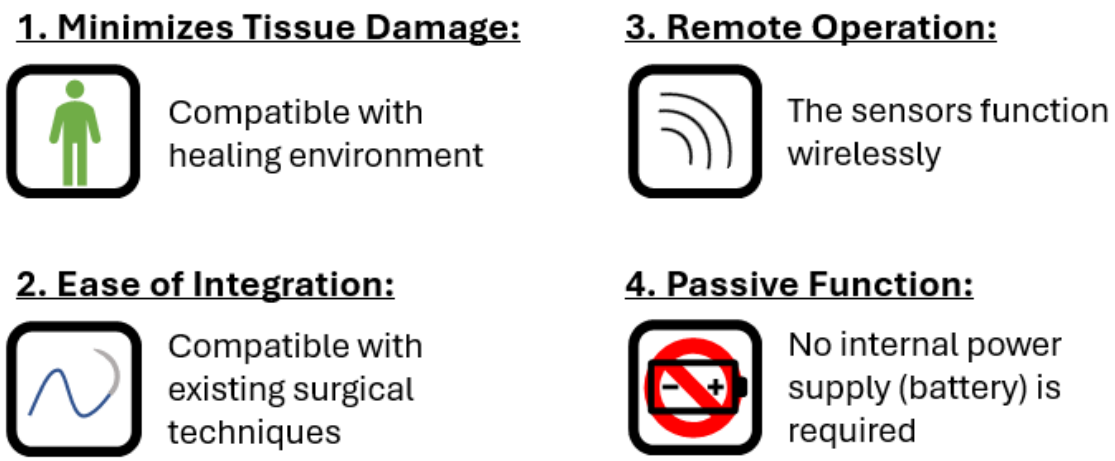

Figure 14. Advantages of utilizing an LC sensor integrated into a suture accessory with implantable devices.

3.2 Sensor Design Clinical Feedback

3.2.1 Voice of Surgeon

Orthopedic surgeon guidance on the suture accessory sensor morphology as well as common suture material types and sizes utilized in tendon and ligament repair surgeries were obtained and implemented into the design of the sensor system. Feedback on ideal suture sensor placement in tendon and ligament repair surgeries was also given. To minimize soft tissue contact damage and irritation, sensor placement at a bone tunnel interface was determined to be ideal. For

example, sensor incorporation at the medial epicondyle humeral bone tunnels in a medial ulnar collateral ligament reconstruction with a docking method would be a suitable application for the proposed sensor to assist with intra- and post-operative suture force quantification. Finally, clinical feedback confirmed that the sensor would be measuring graft loading forces up until the bone tunnel/graft interface heals.

3.2.2 Voice of Physical Therapist

Physical therapist feedback on various aspects of the sensing platform (e.g., sensor functional lifetime, sensor loading ranges) was obtained and incorporated into the design of the LC sensors. Explanations on the various stages of physical therapy, exercise type, and rehabilitation timing were also reviewed and it was suggested that the sensor would be most useful for rehabilitation exercises between 1.5 to 3 months after surgery and that recovery windows span 6 to 12 months after operation for tendon and ligament injuries requiring surgery for most patients.

3.3 Sensor Design Considerations for Ulnar Collateral Ligament (UCL) Reconstruction

3.3.1 Force Detection Range and Sensitivity

Changes in sensor resonant frequency, signal amplitude, and quality factor will be monitored as suture loading is applied from 10 N to 50 N with a step of 5 N in both the loading and unloading directions. This loading range covers correct UCL graft tension (20-40 N) during reconstruction with the addition of $\pm$ 10 N to capture under and overloading conditions while providing 9 discrete steps for generating sensor prototype calibration curves [33]. A loading step of 5 N is approximately equal to 1 lbf and falls well within the 20 N difference required to observe clinical outcome differences as measured by elbow kinematics, stability, and motion pathways in human cadaver studies within a 20 to 60 N loading range [33]. Sensor readings will be collected

within 30 seconds of loading. Any presence of hysteresis will be assessed by comparing sensor output in the loading and unloading directions. With consistent benchtop manufacturing practices, hysteresis should not exceed 5% of the sensor full-scale output as 5% is equivalent to 2 N with a 40 N full-scale output which falls within the 5 N step detection requirement.

3.3.2 Sensor Reproducibility

Variability in sensor performance will be quantified among multiple sensors to ensure consistent fabrication techniques. Sensor measurements should all fall within 10% of one another for non-automated benchtop prototyping purposes as 10% is equivalent to 4 N with a 40 N full-scale output which falls within the 5 N step detection requirement.

3.3.3 Sensor Drift

To comply with UCL reconstruction evaluation protocols, the sensor should withstand 1000 cycles without signal drift exceeding 5% of the sensor full-scale output as 5% is equivalent to 2 N with a 40 N full-scale output which falls within the 5 N step detection requirement [61, 62]. Sensor performance after cyclic loading from 10 to 50 N will be assessed to measure any sensor drift over time.

3.3.4 Load to Failure

The maximum load the sensor can withstand without damaging the sensing mechanism (e.g., permanent deformation) and ultimate loads to mechanical failure (e.g., device structure breaks) will be determined along with modes of failure of the sensor. For UCL reconstruction applications the sensor should withstand 70 N of loading without influencing sensor performance metrics including sensitivity and hysteresis [33]. To prevent catastrophic failure of the sensor structure in the elbow joint, the sensor body will be engineered to have a safety factor of 2.5 in

accordance with IEC 60601. A safety factor of 2.5 indicates the device should be designed to withstand 175 N which is 2.5 times the maximum required suture load of 70 N in a UCL reconstruction.

3.3.5 Temperature Effects

Since the sensor is implanted subcutaneously in a UCL reconstruction application, expected temperate operation range is 33-38°C [63]. Any effects of temperature on sensor performance will be evaluated by testing warmed (33 to 38°C by a step of 1°C) units during sensor loading (10-50 N) on a mechanical tester. Acceptable temperature interference with sensor performance will be less than 5% of the sensor full-scale output as 5% is equivalent to 2 N with a 40 N full-scale output which falls within the 5 N step detection requirement.

3.3.6 Sensor Lifetime

Similar to other suture accessories, the sensor will be designed for chronic implantation with no surgical removal required. The sensor should be measuring graft loading forces up until the bone tunnel/graft interface heals which corresponds to 6-12 months.

3.3.7 Tissue Depth Requirement

Since sensor placement in a UCL reconstruction application is at the humeral medial epicondyle, a sensor detection distance of 3 mm through superficial tissues (skin, subcutaneous tissue, etc.) is required [72].

3.3.8 Sensor Size

The sensor should be no larger than existing suture buttons utilized in UCL reconstruction (≤ 13 x 5 x 3 mm). Further, the sensor must be compatible with #2 USP sized sutures used in UCL reconstruction.

3.3.9 Sensor Materials

Design requirements also include that sensor components are composed of bioinert materials or encapsulated in bioinert materials already utilized in orthopedic implants.

3.4 Sensor Design Iteration Overview

Iterative design while implementing continuous feedback was utilized to create 3 different LC circuit designs and 3 varying sensor body materials/geometries/fabrication methods (Figure 15). Specifically, the sensor LC circuit design began with 1-sided rectangular planar inductors resonating from 400-620 MHz depending on size (e.g., smaller LC sensor area led to higher resonance frequencies). Inductor stacking in the rectangular LC circuit design dropped resonance frequencies to around 30 MHz whereafter the rectangular design was rounded to remove sharp edges. Overall dropping sensor resonance frequency was desired to improve sensor signal detection through body tissues. Sensor body manufacturing methods started with 3D printing with polylactic acid (PLA) for proof-of-concept studies. Injection molding with high density polyethylene (HDPE) was also attempted but design mechanical integrity was not sufficient for UCL reconstruction loads. Polymers that could potentially sufficiently support the sensor bending function had melt temperatures that could damage required circuitry. Therefore, machined polyetheretherketone (PEEK) was implemented in final design prototypes with 3D printed ceramic bases for testing purposes. Further the sensor body shape evolved from rectangular to a more

rounded design to reduce sharp edges and stress concentration points. Overall, 4 different sensor designs were tested in the thesis work by varying LC circuit shape, inductor stacking, sensor boyd material, and sensor body fabrication methods to optimize the sensing platform for UCLR (Figure 15) (Table 2). For all experiments, n = 3 signifies three replicates of the same sensor unless otherwise stated.

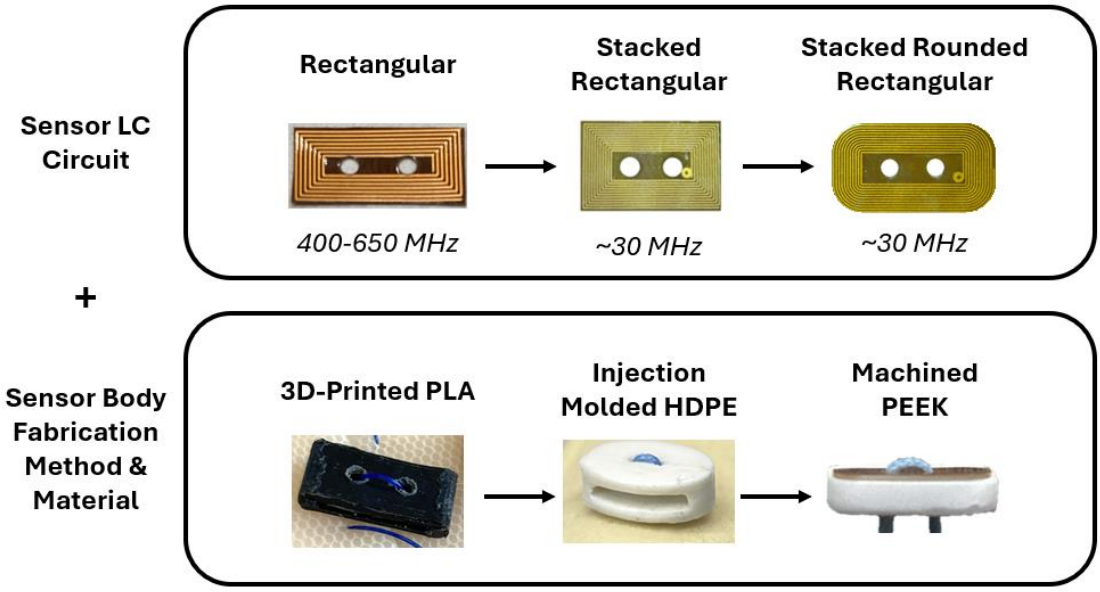

Figure 15. Schematic showing design evolution of both the sensor LC circuit and sensor body.

Table 2. Sensor iteration design comparison.

Sensor Iteration	LC Circuit Shape	Stacked Inductors?	Body Material	Body Fabrication
1	Rectangular	No	PLA	3D printing
2	Rectangular	No	HDPE	Injection Molding
3	Rectangular	No & Yes	PEEK	Machining
4	Rounded Rectangular	Yes	PEEK	Machining

3.5 Sensor Iteration 1: 3D-Printed PLA Body + Rectangular LC Circuit

Initial proof-of-concept studies combined 3D-printed sensor bodies composed of PLA with rectangular, 1-sided LC circuits. Mechanical testing was utilized to demonstrate bending of the LC circuit pattern could transduce suture loading forces.

3.5.1 Sensor Fabrication Materials and Methods

The development of the suture sensor system began by modeling sensors in computer aided drafting (CAD) software (Fusion 360; AutoDesk, San Rafael, CA) and 3D printing design components (Original Prusa i3 MK3S+; Prusa, Prague, Praha, Czech Republic) with polylactic acid (PLA; eSUN, Shenzhen, China). A 7-turn planar inductor coil was generated with circuit design software (Eagle; AutoDesk) and printed on flexible polyimide substrates (Flex Printed Circuit Boards; OSH Park, Lake Oswego, OR) to create an inductor-capacitor (LC) circuit pattern (Figure 16A). The sensor circuit achieved electrical resonance by utilizing a simple planar inductor with inherent parasitic capacitance (Figure 16B). Thermal fusion at 200°C was utilized to embed the flexible circuit within the PLA structure. All components were designed with concentric holes to allow a suture to pass through the sensor (Figure 17). Overall, sensor size was 12 mm × 6.5 mm × 2.5 mm (Figure 17-Figure 18).

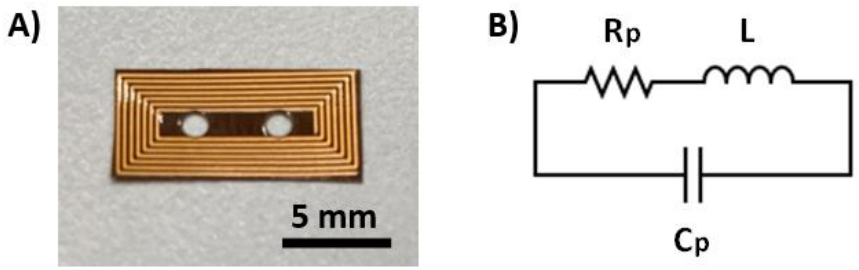

Figure 16. Printed planar inductor coil on a flexible polyimide substrate (A). Equivalent circuit of the planar inductor coil (R_p = parasitic resistance, C_p = parasitic capacitance, L = inductance) (B).

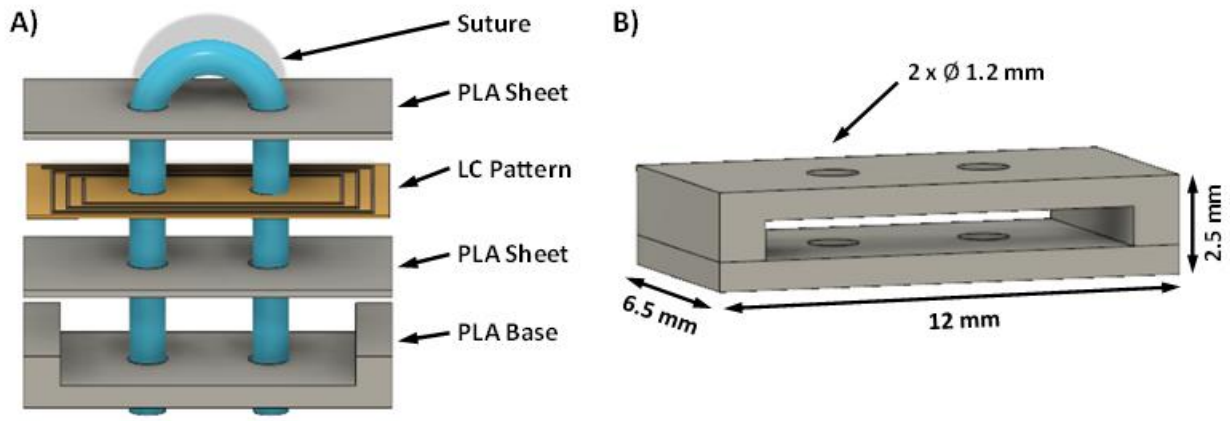

Figure 17. CAD model showing a suture passing through an exploded view of sensor components (A) (PLA = polylactic acid, LC = inductor-capacitor). Suture sensor dimensions in assembled CAD model (B).

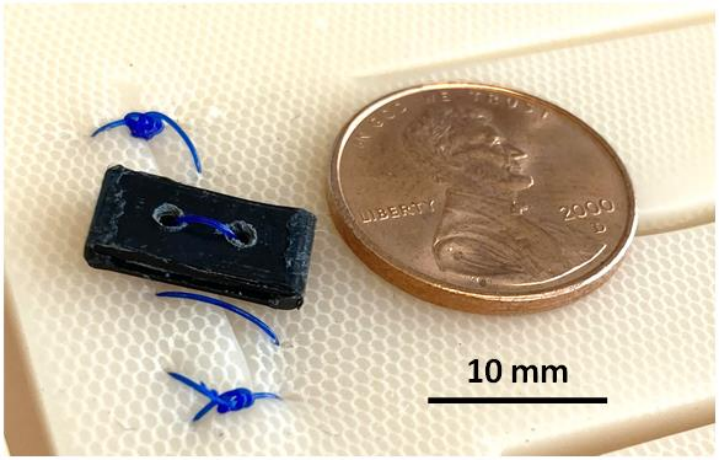

Figure 18. Image showing assembled sensor incorporation in a basic continuous suture pattern.

3.5.2 Sensor Bending and Finite Element Analysis (FEA)

Bending of the circuit pattern embedded in the suture sensor alters the parasitic capacitance of the LC circuit and therefore the measured resonance frequency during force transduction. Since the sensor relies on flexion of the circuit pattern to determine suture force loading, sensor deformation dictates load sensing characteristics of the platform. Therefore, any design

modifications that affect sensor bending of the sensor can alter the sensitivity and detection range of the sensor. Some examples of how to modify sensor flexion include changing the aspect ratio of the sensor, sheet thickness, leg height, leg thickness, and hole separation distance of the design. Sensor deformation simulation results showed bending behavior under 12 N of loading (Figure 19A). Greatest deformation occurred in the area where the loaded suture is adjacent to the upper face of the sensor, and deformation gradually decreased when approaching the leg attachment regions. A suture threaded thru a sensor prototype also demonstrated visible sensor body deformation with applied tension (Figure 19A-B). Overall, the device design was able to achieve bending of the sensor's upper sheet containing the circuit pattern in response to suture loading.

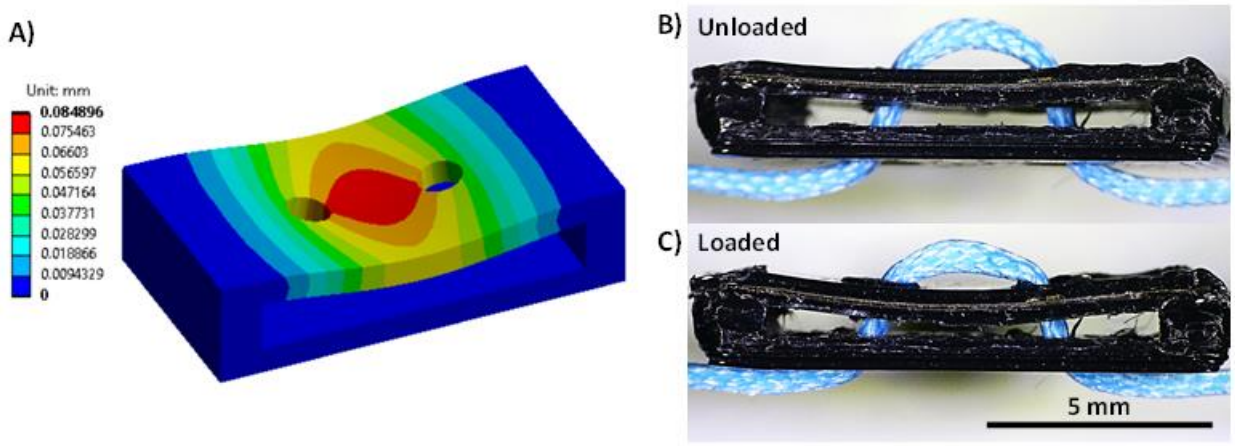

Figure 19. Deformation of suture sensor under loading from FEA study (A). Images showing side views of suture sensor deformation under unloaded (B) and loaded (C) conditions.

3.5.3 Suture Tension Detection

Mechanical testing of the sensor indicated that suture loading and unloading between 2 to 12 N was related to changes in sensor resonance frequency (Figure 20). Specifically, the sensitivity of the sensor was 0.248 MHz/N and the full-scale output (FSO) of the sensor was 2.814 MHz for

the tested loading range. Hysteresis associated with loading and unloading conditions of the sensor did not exceed 7% of the FSO. Hysteresis was consistently the greatest between unloading and loading conditions at 10 N, which may be due to viscoelastic behavior of the sensor body material occurring during loading (12 N). In this study, loading magnitudes were notably lower than the forces experienced by some human connective tissues including the Achilles tendon or anterior cruciate ligament (ACL) [64, 65]. Therefore, the sensor present here is more suitable for tissues including flexor tendons in the hand that experience 2.9 N to 8.8 N of tensile loading during passive and active motion respectively [66]. However, with modifications to the sensor design and material composition the platform may be adapted to accommodate for greater loading ranges. Further mechanical testing indicated that repetitive loading of the sensor from 2 to 12 N did not produce any drift or change in sensitivity over 4 cycles of recurring loads demonstrating the repeatability of platform (Figure 21). This result is significant because maintaining sensor performance with cyclic loading is vital in the suturing of tissues that experience repetitive motion such as tendons and ligaments. In summary, these loading experiments showed the ability of the sensor design to transduce and quantify changes in suture loading.

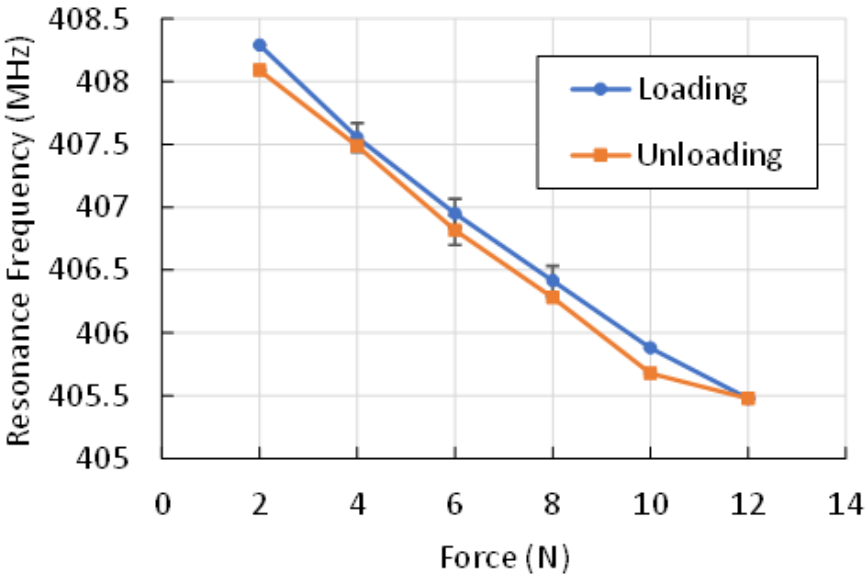

Figure 20. Change in sensor resonance frequency during loading (blue circles) and unloading (orange squares). *Error bars represent standard deviation of the mean (n = 3 measurements of the same sensor).*

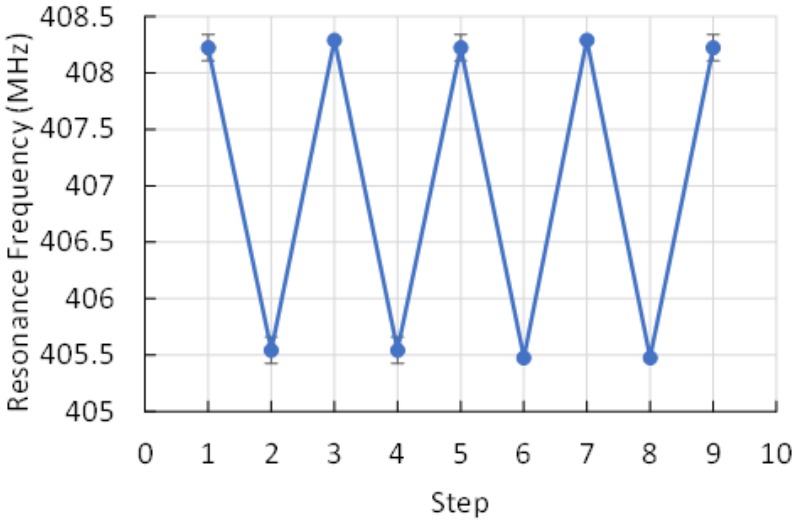

Figure 21. Sensor resonance frequency under repetitive loading from 2 N (408.25 ± 0.04 MHz) to 12 N (405.51 ± 0.04 MHz). *Error bars represent standard deviation of the mean (n = 3 measurements of the same sensor).*

3.5.4 Detection Distances

One important design consideration with wireless, implantable biosensors is ensuring remote communication can be maintained when passing through body tissues (i.e., skin, fat, muscle, etc.). Detection distance of the sensor evaluated with the use of varying thickness tissue mimics indicated a logarithmic relationship between tissue thickness and measured sensor impedance magnitude (Figure 22). Tissue thickness superficial to tendons and ligaments within the human body is highly location specific. The maximum thickness tested (16 cm) reduced sensor impedance amplitude to 0.1 Ω, restricting the current design to more superficial repair applications in elbow extensor, Achilles, quadriceps, patellar, and hand flexor tendons. Transmission depth limitations could be improved by stacking multiple inductor circuits within the sensor, optimizing detection coil design, and increasing the power output form the detection device.

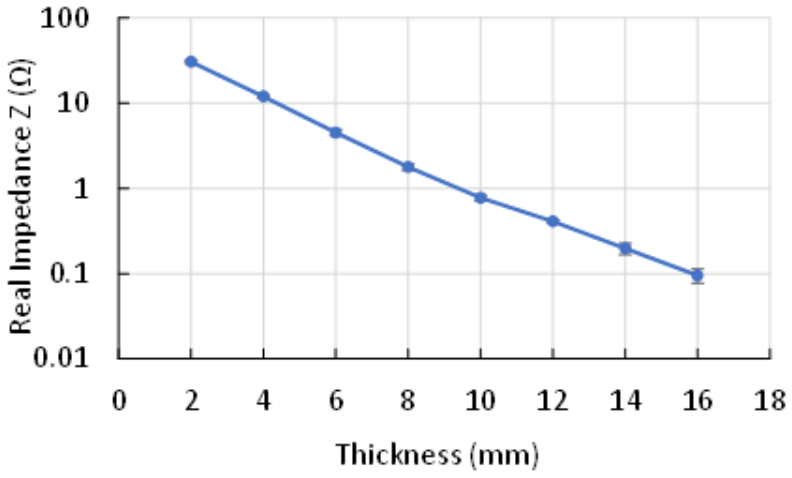

Figure 22. Sensor impedance at the resonance frequency as a function of tissue mimic thickness. *Error bars represent standard deviation of the mean (n = 3 measurements of the same sensor).*

3.6 Sensor Iteration 2: Injection Molded HDPE Body + Rectangular LC Circuit

Initial proof-of-concept studies with 3D-printed sensors indicated force sensing mechanisms over loading ranges from 2-10 N (Figure 23). To accommodate increased loading ranges associated with UCL reconstruction, injection molded high-density polyethylene-based sensor body designs were employed (Figure 23).

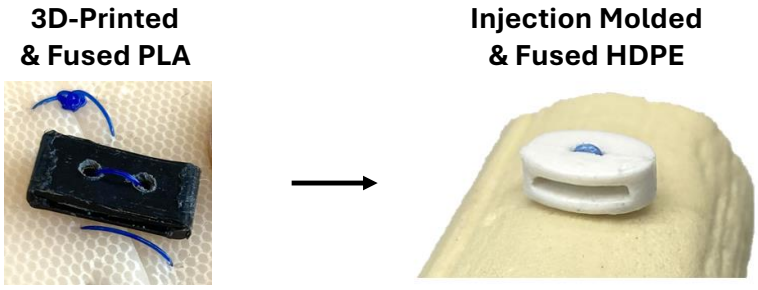

Figure 23. Sensor design evolution from a 3D-printed polylactic acid (PLA) version to an injection molded high-density polyethylene (HDPE) version.

3.6.1 Sensor Fabrication Materials and Methods

Sensor prototypes for proof-of-concept studies were rectangular in shape which was not conducive for implantable sensor deployment and biocompatibility. Therefore, the design of the sensor was modified to be more oval and rounded in shape (Figure 24). All perimeter edges of the sensor body were filleted to minimize tissue irritation.

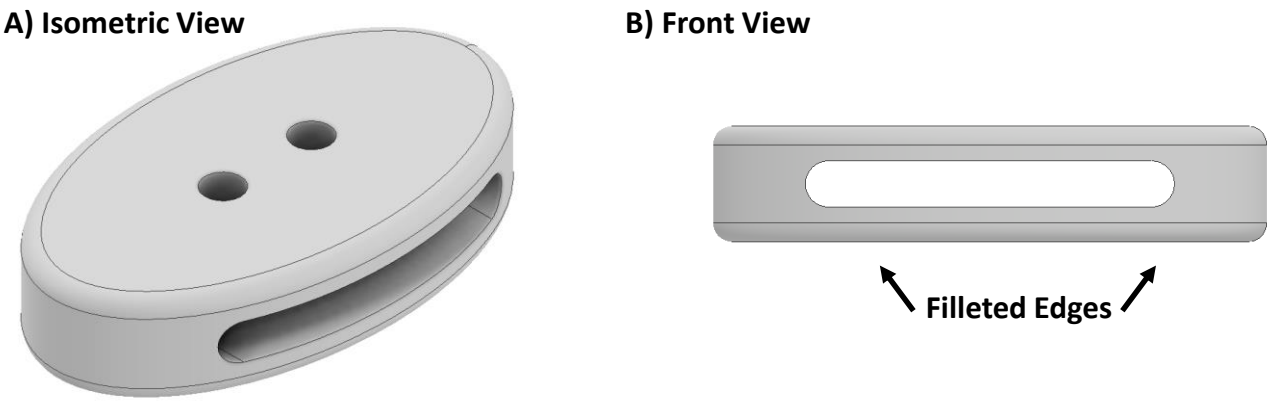

Figure 24. CAD drawings showing the isometric (A) and front (B) view of an oval-shaped sensor body.

Suture sensors were fabricated by embedding a flexible printed circuit into a high-density polyethylene (HDPE) suture sensor structure. For rapid circuit design prototyping, a custom program was developed in Eagle printed circuit board software to simply alter circuit trace width, spacing, positioning and aspect ratio with a few user inputs. This automated circuit design program eliminated the process of manually drawing repetitive circuit patterns and saved hours of time in the design process. An example circuit pattern output from the custom program is included (Figure 25A). Injection molded suture sensor body components were thermally fused with molds to embed the flexible sensing circuit pattern (Figure 25-Figure 26). The overall size of the suture sensor was approximately 7 x 12 x 4 mm, which is similar to existing small suture buttons that are sometimes utilized at bone tunnel interfaces in orthopedic surgeries (Figure 27). Clinical feedback indicated that the overall height of the sensor structures needs to be reduced to 3 mm to be utilized at an injury site. Improved molding and fabrication techniques with industrial-grade tools could be utilized to shrink the height dimension for future studies. A portfolio of suture sensor designs were generated to accommodate various loading ranges by altering sensor membrane thickness. Specifically, sensors with membrane thicknesses of 1.25 and 1.75 mm were developed while

maintaining the same overall sensor height (Figure 27). It should be noted that other modifications that influence sensor bending in response to applied suture loading, such as changing the sensor aspect ratio and altering suture hole spacing, could also be utilized to adjust sensor loading range and sensitivity. The measured resonance frequency of the thicker sensor was 620 MHz at 0 N of loading (Figure 28). Compared to preliminary proof-of-concept sensors, this frequency is ~200 MHz higher since the sensor circuit trace pattern was decreased in size for surgical application compatibility. Lowering the frequency could help with minimizing losses due signal transmission through tissue, reducing interference. Since the circuit pattern was rectangular in shape while the sensor structure is oval-shaped, the circuit pattern could be altered to be oval in shape to increase resonance frequency and coupling between the sensor and external detection coil.

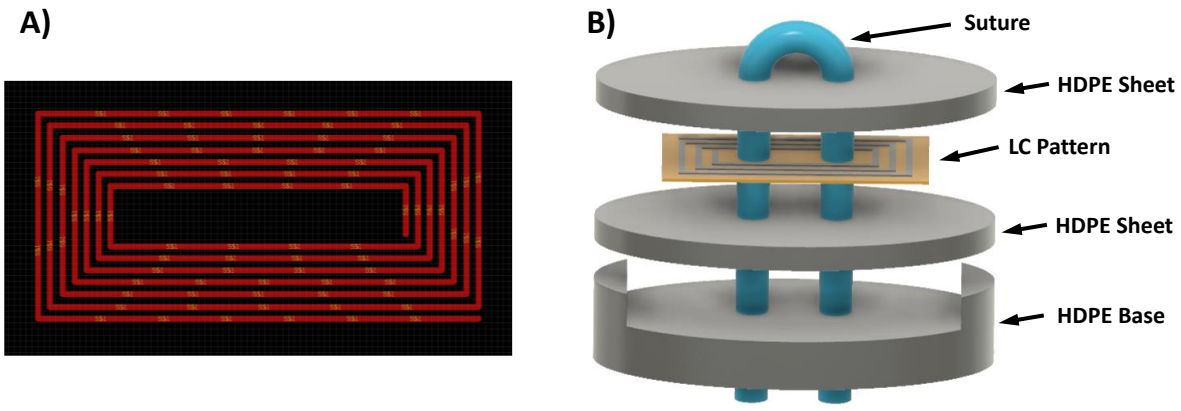

Figure 25. Printed circuit pattern generated with an automated user-interface Eagle program (A). Exploded view of fused sensor layers (B). *LC = inductor-capacitor.*

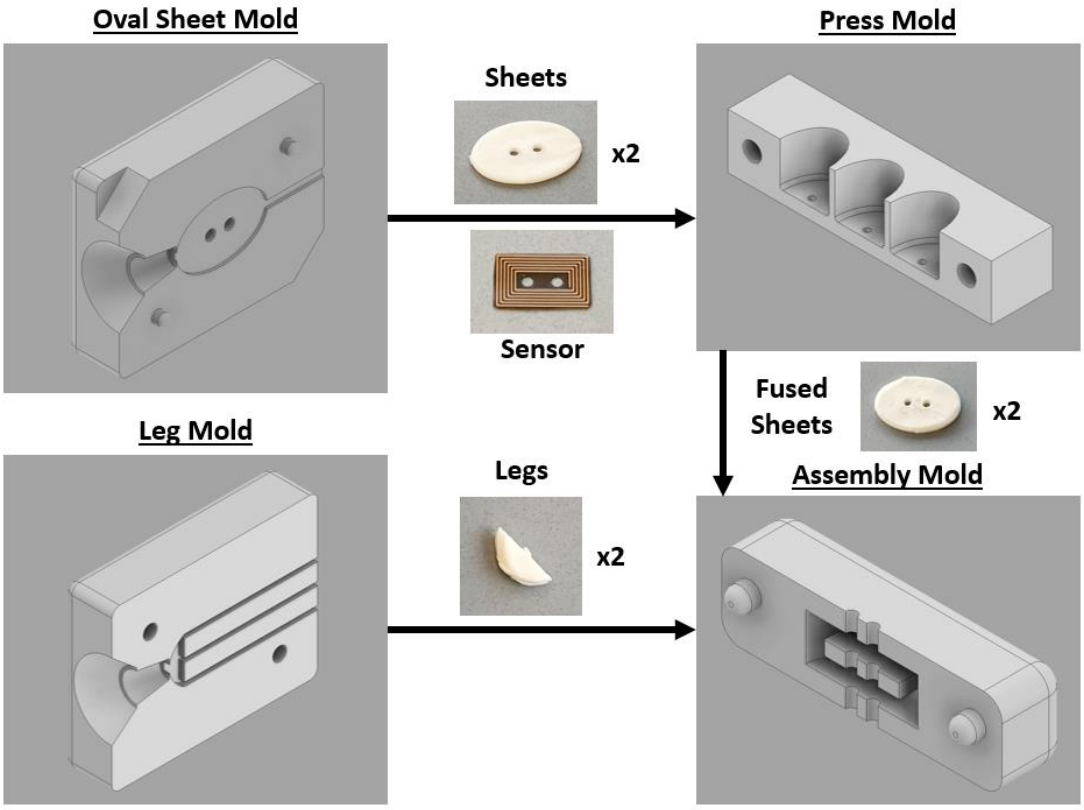

Figure 26. Molds and components utilized to fabricate suture sensors. Mold halves are shown to highlight internal features and details.

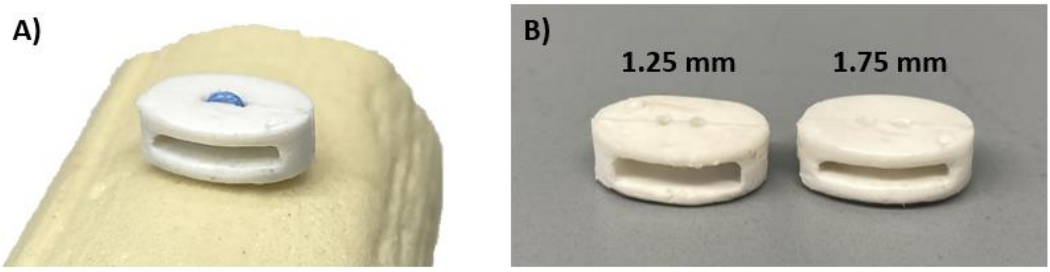

Figure 27. Assembled 1.75 mm suture sensor with suture at a bone tunnel interface (A). Assembled suture sensors with 1.25 and 1.75 mm membrane thicknesses (B).

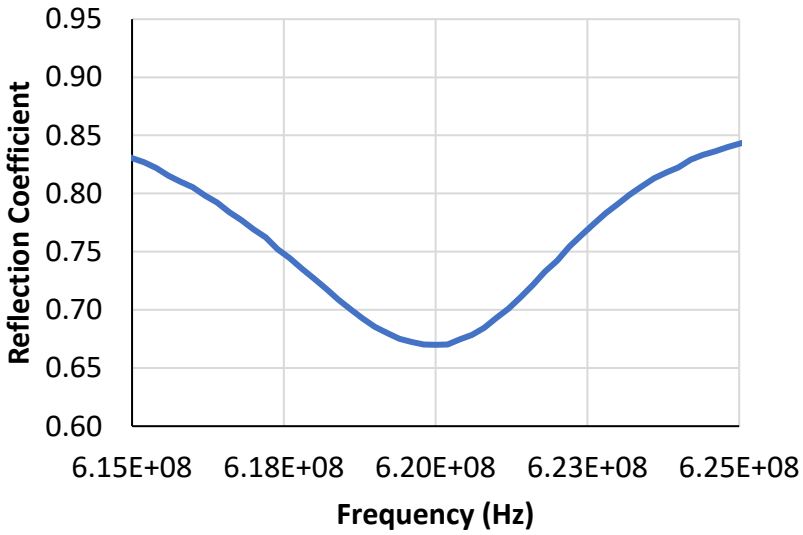

Figure 28. Resonance spectra of unloaded 1.75 mm suture sensor showing a resonance frequency of 620.0 MHz.

3.6.2 Sensor Bending and Finite Element Analysis (FEA)

Static loading of the 1.75 mm suture sensor indicated deformation of ~0.25 mm with ~35 N of suture load (Figure 29A-B). A simple finite element analysis (FEA) model was used on the oval sensor geometry to evaluate sensor deformation under static loading conditions. Results indicated deformations in the Z-direction reached a maximum of ~0.3 mm at 35 N of loading which was similar to measured deformation (Figure 29C). Limitations of the FEA model include that the simulation assumed loading only occurred in the linear elastic region of the HDPE sensor material and the fact that the model geometry and materials was composed of only HDPE, not including the flexible copper and polyimide sensor component.

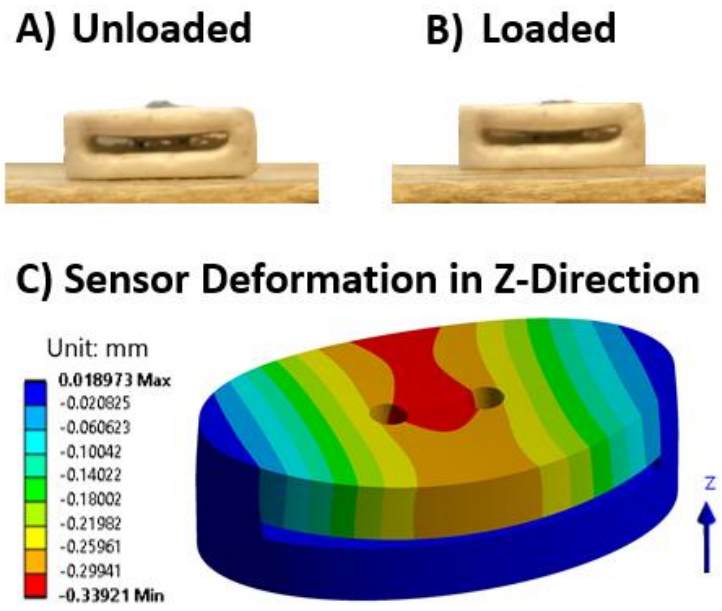

Figure 29. Images of a suture sensor in unloaded (A) and loaded (B) conditions showing a measured deformation (~0.25 mm) of the top sheet due to a static 35 N suture load. Simulated FEA loading of the sensor showing sensor deformation in the Z-direction at 35 N of loading (C).

3.6.3 Suture Tension Detection

To determine loading ranges and sensitivities of the varying sensor designs, static and cyclic mechanical tests were performed. A custom ceramic 3D-printed sample holder was used to hold the sensor and detection coil in place during mechanical testing (Figure 30). All mechanical testing studies were performed with braided polyester size #2 sutures as this type and size suture is used in many medium-sized tendon and ligament reconstruction orthopedic surgeries. A 40 N pre-load was applied to the sensors for 60 seconds before further mechanical testing was performed. Loading the thicker (1.75 mm) sensor from 5 to 35 N by a step of 5 N showed a near linear sensitivity of 0.0339 MHz/N (R-squared value: 0.99) from the 10 to 35 N loading range (Figure 31**)**. However, standard deviation calculations showed large variability in sensor readings for the same applied load, especially at the highest tested load (35 N) with a standard deviation of

0.4 MHz. In fact, standard deviations were too large for the sensor to accurately distinguish between loads within 20-25 N of each other over the tested loading range. Also, the sensor's resonance frequency increased with applied loading, suggesting either the inductance or capacitance of the sensor are increasing in response to deformation of the sensor platform. Overall, the thicker sensor had a full-scale output (FSO) of 1.1 MHz over the testing load range from 5 to 35 N. Unloading of the sensor showed a non-linear relationship between applied loading and sensor output, exhibiting a second-order polynomial shape and large hysteresis (Figure 31). Hysteresis was largest between 10-20 N of loading at 69-72% the FSO. Furthermore, sensor resonance frequency was consistently higher with the unloading curve versus the loading curve for the same applied load. The discrepancy between the loading and unloading curves of the sensor could be a result of the HDPE material, suture material, knot behavior, or cinching performed by the suture on sensor during unloading. Since the sensor repeatability returned to a lower resonance frequency at the start of each trial, a time-dependent variable in the sensing platform may have influenced sensor performance.

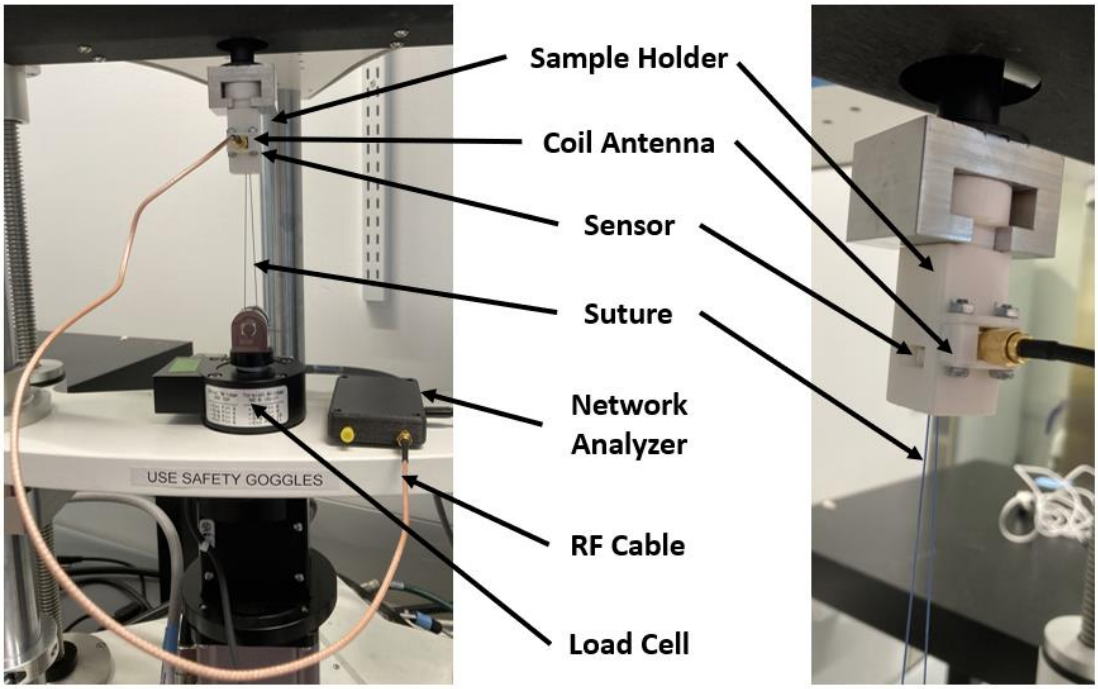

Figure 30. Images of mechanical testing set-up showing major components utilized during sensor evaluation.

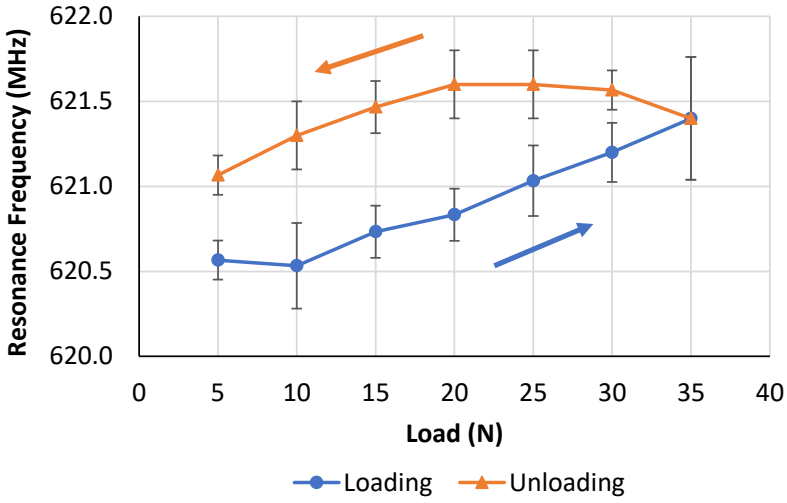

Figure 31. Suture sensor (0.75 mm size) mechanical testing sensitivity results showing sensor resonance frequency change during loading (blue circles) and unloading (orange triangles). *Error bars represent standard deviation of the mean (n = 3 measurements of the same sensor).*

Further mechanical testing sensor indicated that repetitive loading of the thicker sensor from 5 to 35 N produced drift and inconsistent changes in sensitivity over 5 cycles of recurring loads demonstrating that the sensing platform was not repeatable (Figure 32A). The initial increase in sensor output during the first cycle of loading matches the behavior of the sensor during calibration curve generation. Initial testing with increased loading cycles was also performed after 100 and 200 cycles of loading from 5 to 35 N (loading rate of 1 cycle per second) but inconclusive as more sensors needed to be made to produce more replicates (Figure 32B). Variation in sensor performance with cyclic loading is significant to address because tendon and ligament tissues experience repetitive motion. To further evaluate variation and drift in the sensor system, the thicker suture sensor was loaded to and held at 35 N whereafter signal recordings were measured every 30 seconds over a 5-minute period. Results showed that the sensor signal increased by 0.8 MHz (73.7% the FSO) within 5 minutes, indicating a time-dependent drift in the sensing platform and a possible explanation why variability in sensor output is so high (Figure 33). Possible sources of drift include the influence of material properties of the suture, suture knot slippage, non-linear elastic behavior of the sensor material, or digging of the suture into the sensor material. Decreasing the thickness of the sensor from 1.75 to 1.25 mm was expected to increase sensitivity and reduce loading range detection, as a thinner sensor sheet should deform more with the same applied loading and deform at lower loading forces. However, the preload (40 N) and tested loading range (5-35 N) led to large permanent deformation of the sensor structure, damaging the sensor by reducing sensitivity as a result overloading (Figure 34). The higher resonance frequency (~641 MHz) for the thinner sensor compared to the thicker sensor (~620 MHz) shows increasing deformation, increases sensor output, as preloading caused more deformation in the thinner sensor. Besides permanent deformation of the sensor sheet, another mode of failure includes the suture

material tearing through the sensor plastic material. Hardness of the injection moldable HDPE material was poor compared to other implantable plastics (e.g., ultra-high molecular weight polyethylene) and visible indentation of the sensor material from the suture occurs after 30-35 N of loading, even for the thicker sensors (1.75 mm).

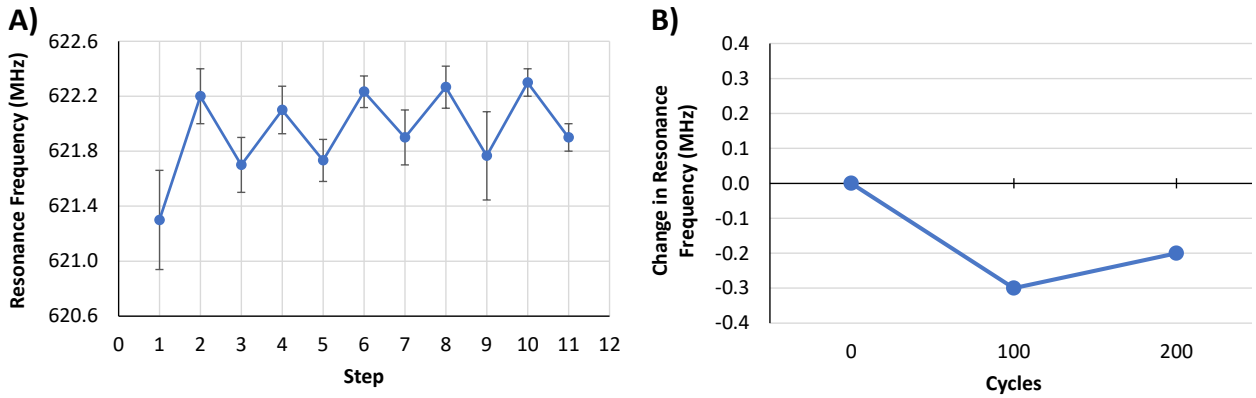

Figure 32. Cyclic loading of the sensor from 5 to 35 N showing drift and deviation over 5 loading cycles (A). *Error bars represent standard deviation of the mean (n = 3 measurements of the same sensor).* Change in measured baseline resonance frequency after 100 and 200 loading cycles from 5 to 35 N *(n = 1)* (B).

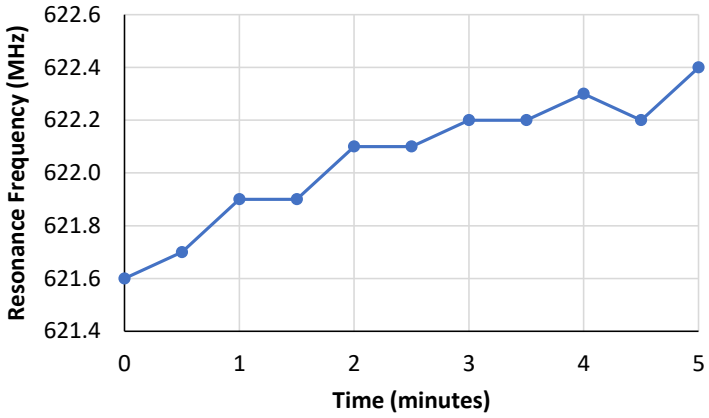

Figure 33. Change in resonance frequency over 5 minutes after a constat 35 N of load is applied indicating instability and increasing drift in the sensing system *(n = 1)*.

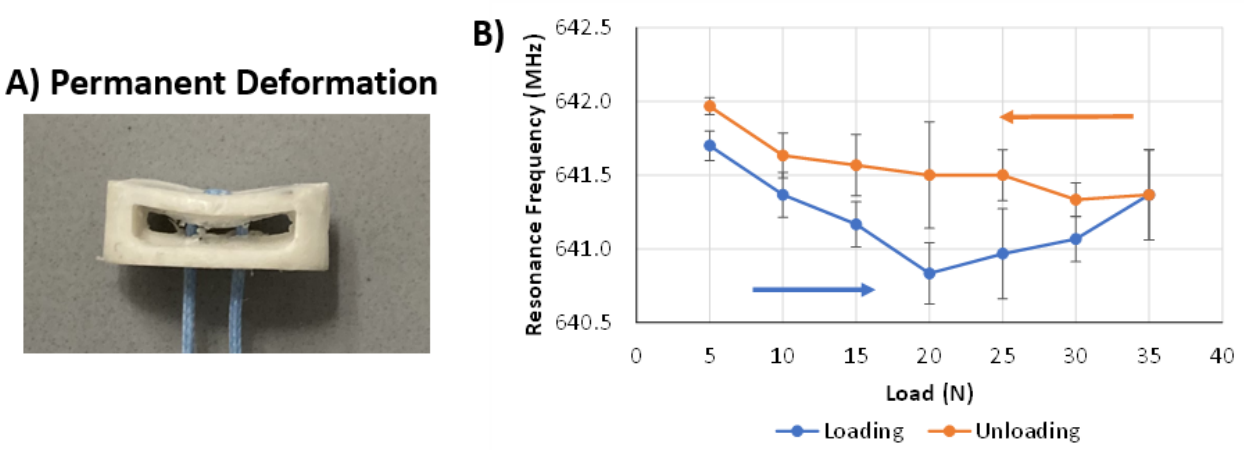

Figure 34. Plastically deformed thinner (1.25 mm) sensor due to overloading (A). Example force loading curve showing loss in sensitivity due to overloading failure in a sensor (B). *Error bars represent standard deviation of the mean (n = 3 measurements of the same sensor).*

3.7 Sensor Iteration 3: Machined PEEK Body + Rectangular, Stacked LC Circuit

After proof-of-concept sensor designs utilized 3D printing, injection molded polypropylene was employed for the sensor body to accommodate for increased loading ranges associated with UCL reconstruction. However, there were issues with the injection molded design causing sensor failure and plastic deformation within the desired loading range. Therefore, the sensor material was switched to polyetheretherketone (PEEK), a polymer commonly utilized in orthopedic implants due to mechanical properties that are more similar to bone.

3.7.1 Sensor Fabrication Materials and Methods

Since the sensing circuitry could not withstand PEEK injection molding temperatures, PEEK machining methods were employed. First, the polyimide printed circuit boards containing the sensor circuit were adhered to machined PEEK substrates with strain gauge adhesive. To isolate the sensing circuitry, the sensor was encapsulated with medical grade epoxy. For prototyping

purposes, a sensor base was 3D printed from ceramic resin. Finally, the sensor was assembled with both an open base design to visualize sensor deformation for characterization purposes and a protective closed based design (Figure 35).

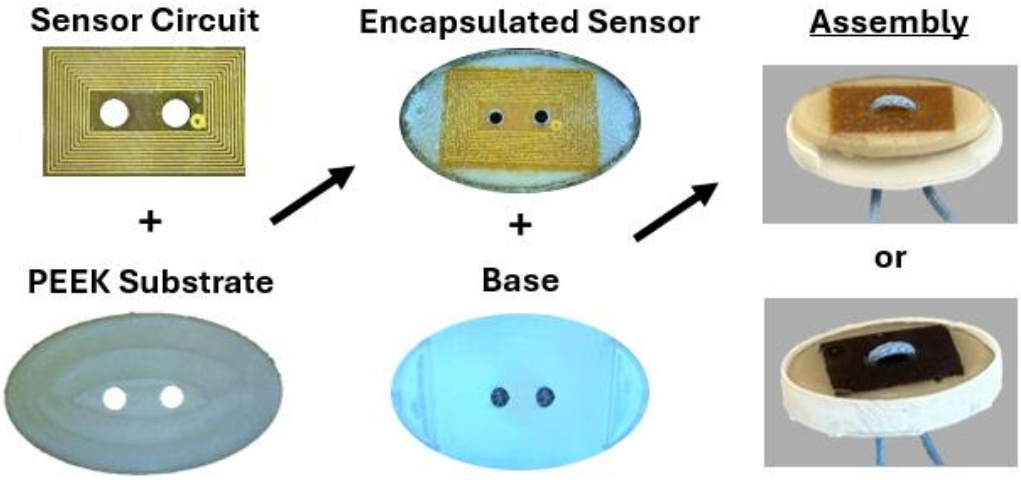

Figure 35. Stepwise images showing how the updated sensor design was fabricated and assembled.

3.7.2 Impact of Substrate Thickness

To generate sensors with a range of loading applications, the thickness of the PEEK backing material was varied (0.5, 1, and 2 mm). The 0.5, 1, and 2 mm sensors were loaded over 3 different ranges: 2-8 N, 5-40 N, and 10-60 N (Figure 36). The sensitivities of the sensors were 0.12, 0.09, and 0.08 MHz/N for the 0.5, 1, and 2 mm PEEK thicknesses respectively. Over the sensor's respective loading ranges the full-scale output of the sensors were 0.77, 3.23, and 4.15 MHz for the 0.5, 1, and 2 mm PEEK thicknesses. Increasing the thickness of the PEEK backing material decreased sensitivity when comparing 0.5 versus 1 mm PEEK thicknesses while the full-scale output was greater with sensors able to withstand relatively higher loads. Overall, varying

PEEK backing material thickness provided a wide range of load sensing for various tendon or ligament applications.

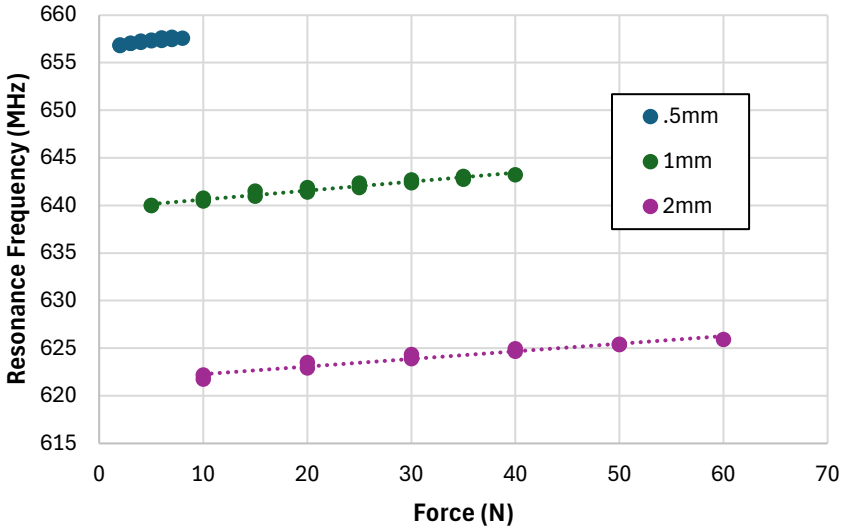

Figure 36. Resonance frequency readings during loading and unloading of sensors of varying PEEK thickness (0.5, 1, and 2 mm). *Error bars represent standard deviation of the mean (n = 3 measurements of the same sensor).*

To evaluate the impact of epoxy encapsulation on sensor load response, unencapsulated and encapsulated sensors were loaded from 5-40 N and 10-50 N respectively (Figure 37). Sensor baseline resonance frequency decreased with encapsulation likely due to the impact of the encapsulation material on parasitic capacitance in the sensor circuit. As expected, the sensitivity of sensors decreased with encapsulation. Specifically, sensitivity dropped from 0.092 MHz/N to 0.051 MHz/N with encapsulation (44.6% reduction). The full-scale output also decreased from 3.23 MHz to 1.88 MHz with encapsulation (41.8% reduction). However, the encapsulation material reinforced the sensor to withstand greater loading ranges.

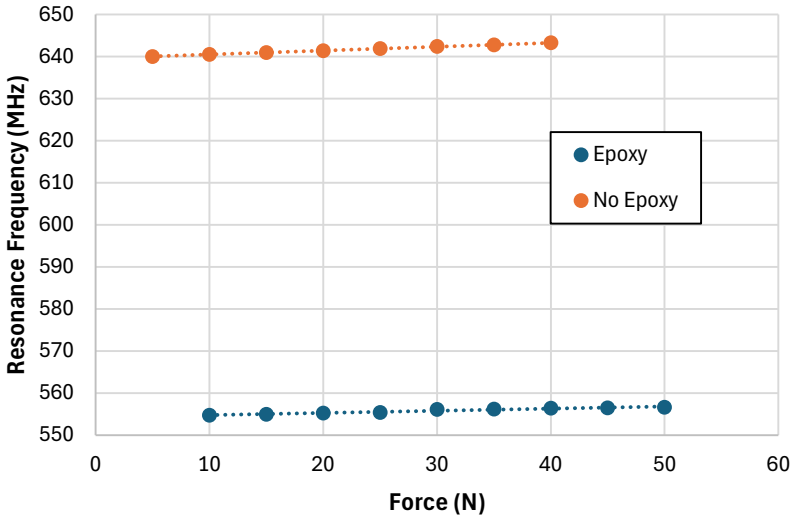

Figure 37. Changes in high-frequency sensor resonance frequency during loading of encapsulated (blue) and unencapsulated (orange) sensors. *Error bars represent standard deviation of the mean (n = 3 measurements of the same sensor).*

3.7.3 Impact of Inductor Stacking in LC Circuit

Since initial sensor circuit planar inductor designs resonated at 640 MHz, reducing resonance frequency was desired to improve signal transmission through tissues. Strategies for dropping resonance frequency include increasing the circuit's inductance or parasitic capacitance following Equation 5. Because planar inductor length and width dimensions are limited to comply with sensor application in UCL reconstruction, an increase in inductance and parasitic capacitance was achieved by utilizing a stacked inductor design (Figure 38). Stacking inductor coils reduced sensor resonance frequency by 20 times to a value of 33.3 MHz (Figure 39). However, the stacked inductor design increased parasitic resistance of the circuit, reducing the quality factor of the signal which decreases force sensing resolution of the system. Specifically, quality factor (Q) is influenced by the inductance (L), parasitic capacitance (C_p), parasitic resistance (R_p) of the circuit according to Equation 7.

Investigations into the effects of polyimide substate thickness on circuit behavior also indicated reducing substrate thickness reduced resonance frequency, increased quality factor, and did not impact impedance (Figure 40).

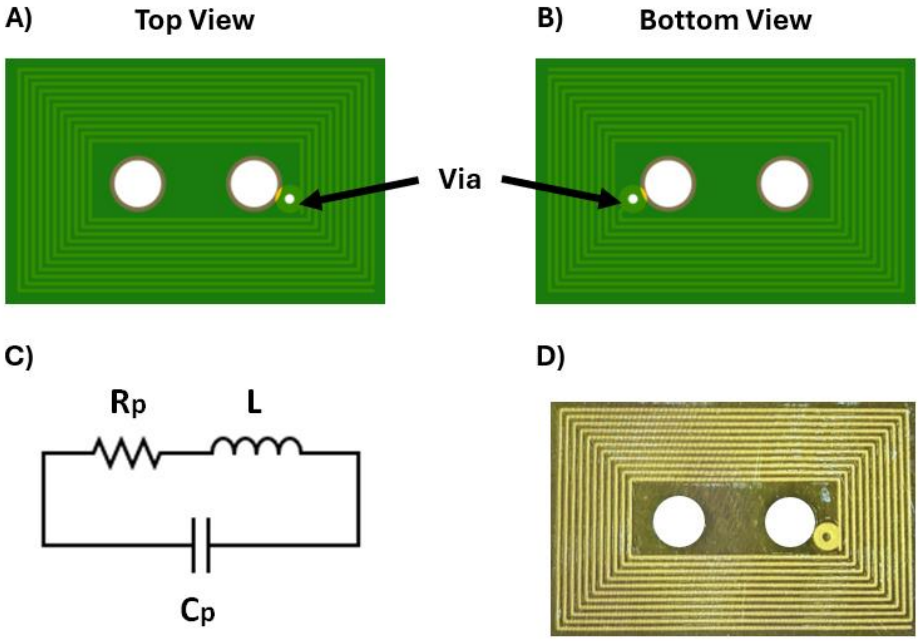

Figure 38. Top (A) and bottom (B) view of double-sided inductor design. Equivalent resonance circuit of inductor design where R_p = parasitic resistance, L = inductance, and C_p = parasitic capacitance (C). Printed circuit board of the double-sided inductor design on a flexible polyimide substrate (D).

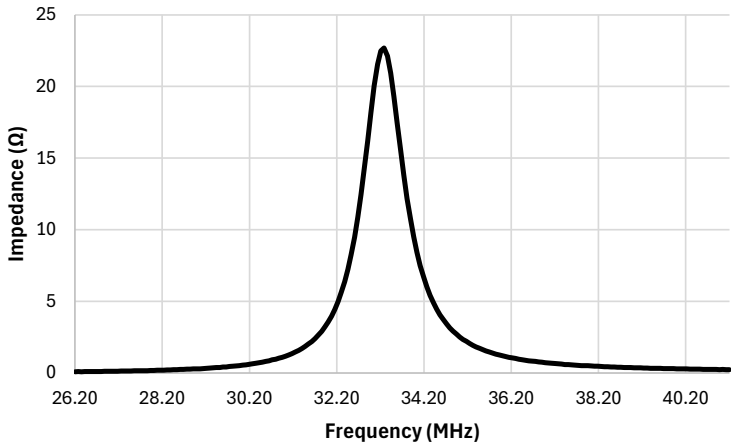

Figure 39. Resonance spectra of the stacked inductor design circuit.

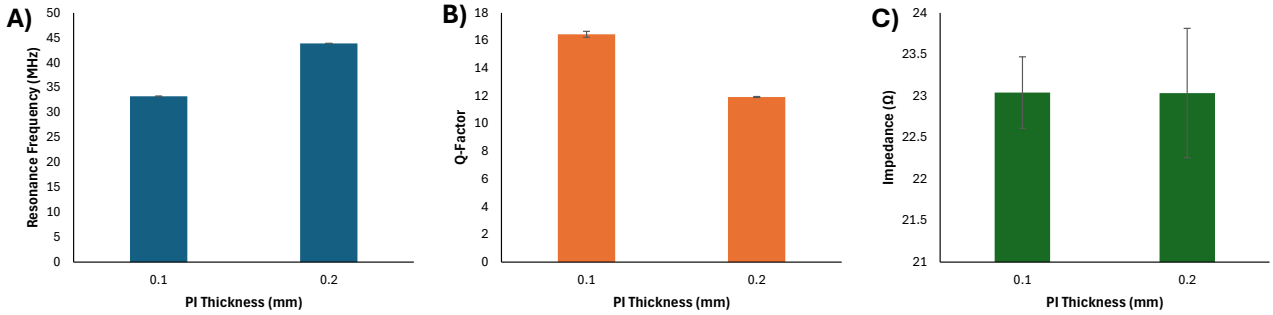

Figure 40. Polyimide (PI) substrate thickness impact on circuit resonance frequency (A), quality factor (Q-factor) (B), and impedance magnitude at resonance (C). *Error bars represent standard deviation of the mean (n = 3 measurements of the same sensor).*

3.7.4 Suture Tension Detection

After combining the reduced resonance frequency sensor circuit design and epoxy encapsulation techniques, mechanical testing was utilized to evaluate sensor recordings during UCL-relevant loading and unloading ranges of 10-50 N by a step of 5 N (Figure 41A). Results indicated a liner relationship ($R^2 = 0.99$) between the load applied and resonance frequency of the sensor. Sensitivity was .0027 MHz/N and the full-scale output was 0.107 MHz. Hysteresis was

maximum at 25 N of loading with a value of 7.81% of the full-scale output. The reflection coefficient at resonance was also recorded as a measure of signal amplitude over the loading range (Figure 41B). When loading from 10 to 50 N, the reflection coefficient slightly increased by 2.33% according to a 2nd order polynomial trend ($R^2 = 0.99$). To assess load reading stability, the sensor was loaded from 10 to 50 N and recordings were taken every 30 seconds over 5 minutes (Figure 42A). Conversely the sensor was unloaded from 50 to 10 N and recordings were taken every 30 seconds over 5 minutes (Figure 42B). Cyclic loading of the sensor from 10 to 50 N over 10 cycles of loading yielded no drift behavior (Figure 42C). After 1000 cycles of loading at 1Hz, the sensitivity of the sensor over the 10-50 N loading range remained the same, indicating the sensor still functions well with repetitive loading. Further, initial overload testing to 60 and 70 N, demonstrated that sensor measurements returned to baseline (Figure 42D).

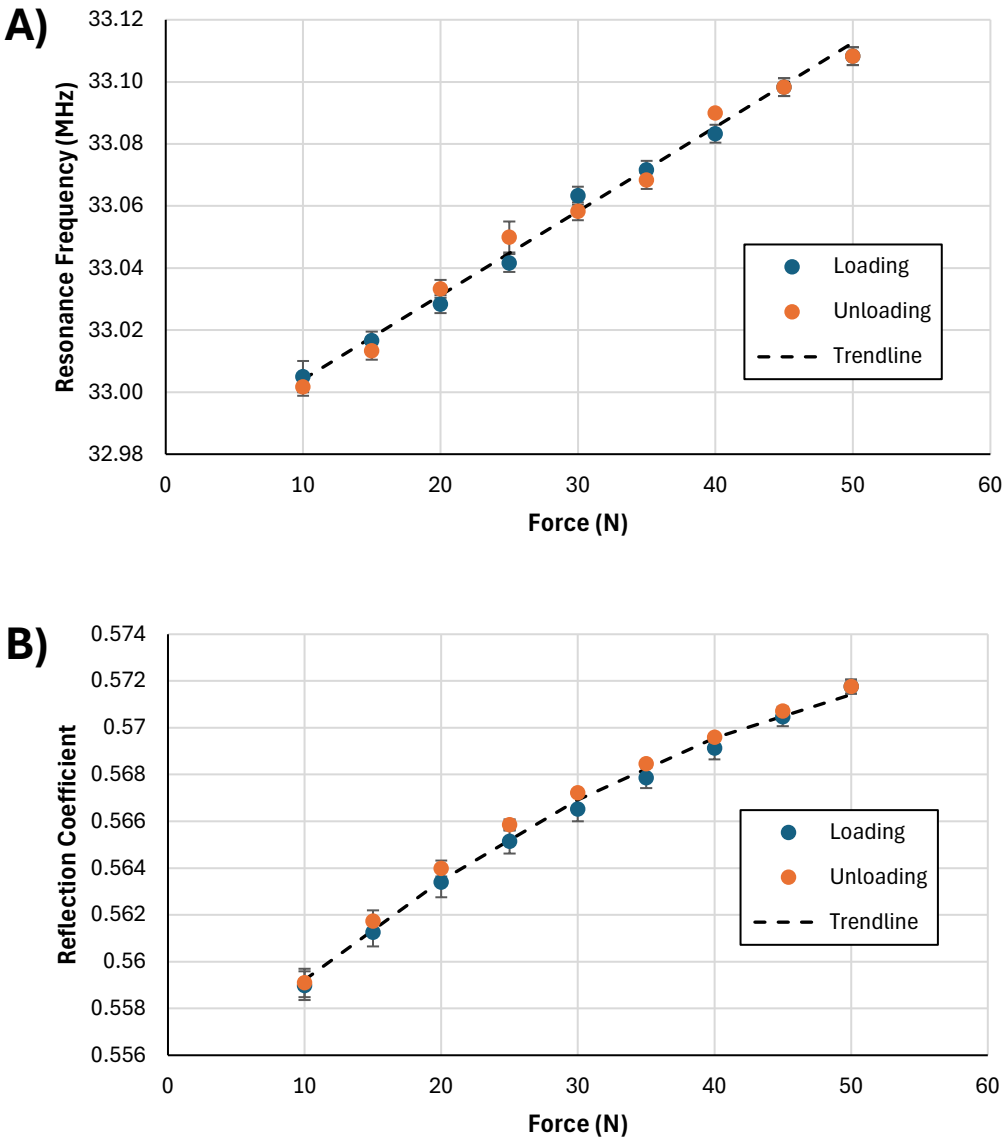

Figure 41. Changes in sensor resonance frequency (A) and reflection coefficient at resonance (B) during loading (blue) and unloading (orange) from 10 to 50 N. *Error bars represent standard deviation of the mean (n = 3 measurements of the same sensor).*

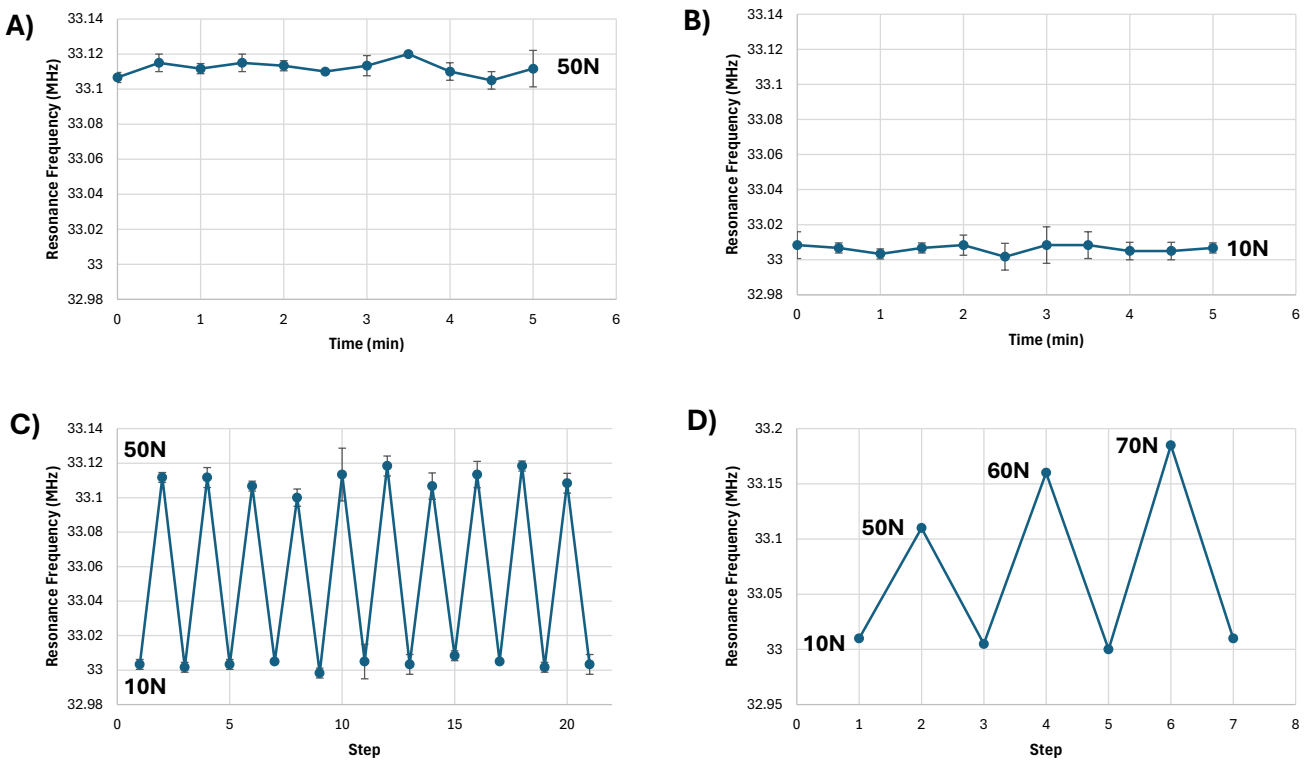

Figure 42. Sensor output over time when loaded to 50 N (A) and unloaded to 10 N (B). Changes in sensor resonance frequency over 10 cycles of loading from 10 to 50 N (C). *Error bars represent standard deviation of the mean (n = 3 measurements of the same sensor).* Sensor output with overloading of 60 and 70 N *(n = 1)* (D).

3.8 Sensor Iteration 4: Machined PEEK Body + Rounded Rectangular, Stacked LC Circuit

3.8.1 Sensor Fabrication Materials and Methods

Previous sensor design indicated that an electrical resonance-based suture accessory sensor could wirelessly transduce suture loading force. To reduce baseline sensor resonance frequency in a range conducive to signal transmission through tissue (< 100 MHz), an improved sensor circuit design was achieved by stacking copper (0.07 mm trace width and spacing) inductor patterns

connected with a via on each side of a flexible polyimide substrate 0.1 mm thick (PCBWay; Hangzhou, China) [55].

Sensor substrates were machined from polyetheretherketone (PEEK), a bioinert polymer commonly used in orthopedic repair surgeries [67, 68]. Substrates were shaped in the form of rounded rectangles and sized at approximately 12 mm in length and 6 mm in width to mimic the footprint of existing suture accessories utilized in UCLR and prevent ulnar nerve irritation [69]. A couple different sensor substrate designs were utilized to test the effects of altering sensor body geometry on sensitivity and loading ranges, specifically substrate thickness was varied at 0.75 and 1 mm. (Figure 40). Holes for passing sutures were 1 mm in diameter and placed 2.5 mm apart to accommodate for both UCLR bone tunnel dimensions and #2 United States Pharmacopeia sized sutures used in UCLR [69, 70]. Sensor circuits were secured to the PEEK substrates with strain gauge adhesive (M-Bond 610; MicroMeasurements, Wendell, NC) according to the manufacturer's specifications. A sensor base structure was designed to enable circuit substrate deformation with loading and 3D printed (Rigid 10K; FormLabs, Somerville, MA) for prototyping purposes (Figure 43A). The sensor suture accessory was designed to be placed on the medial epicondyle of the humerus just above the humeral bone tunnel to anchor the graft in an UCLR (Figure 43B).

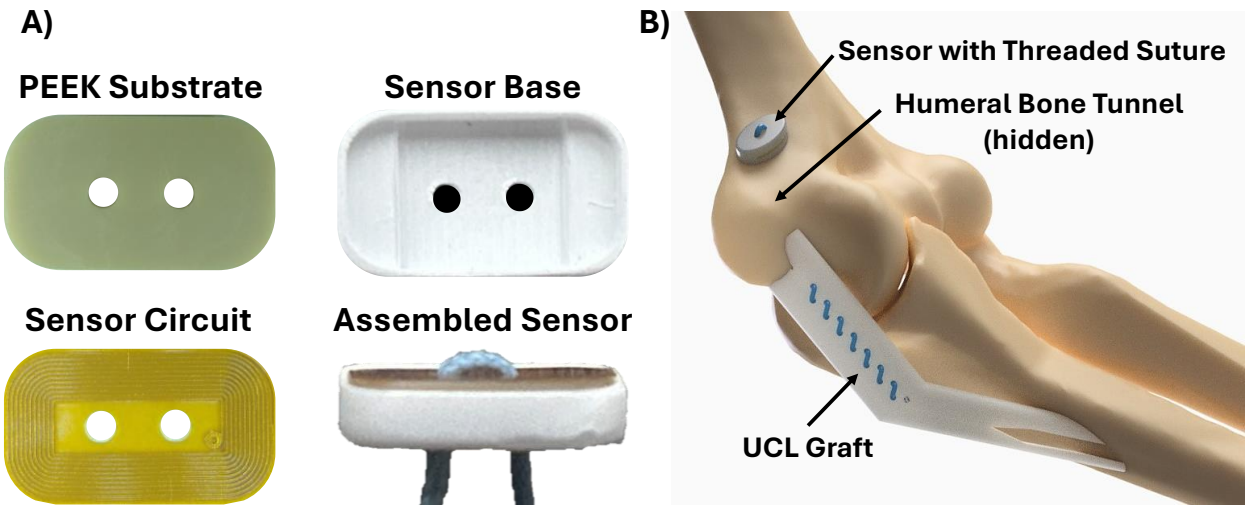

Figure 43. Sensor components and threaded assembly (A). Rendering of the sensor placed at the proximal end of the humeral bone tunnel containing the UCL graft in an UCLR employing the proximal single-tunnel suspensory fixation technique (B).

3.8.2 Planar Inductor Coil Reproducibility

To evaluate the lot distribution of planar inductor coil circuits with respect to baseline resonance frequency, measurements were taken on multiple samples (n=35). Results indicated that the mean baseline resonance frequency was 28.25 MHz with a standard deviation of $\pm$ 0.14 MHz. Distribution plots showed a slight positive skew (Figure 44A-C). However, an Anderson-Darling test for normality indicated a failure to reject the null hypothesis of a normal distribution ($p = 0.33$ which is > 0.05). Further tolerance interval setting and testing would be required to determine if improved planar inductor manufacturing techniques or suppliers are necessary for reproducible sensor designs.

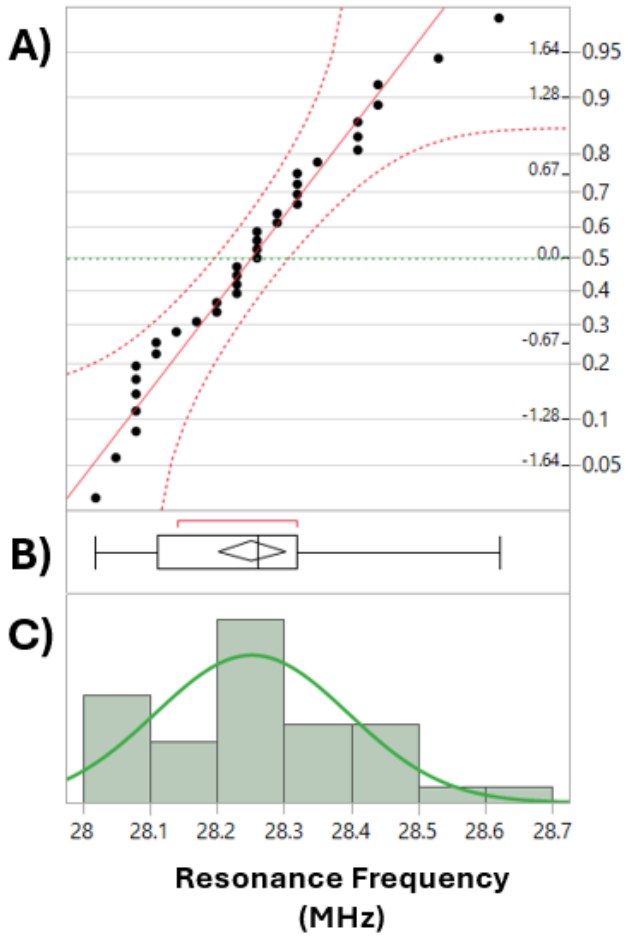

Figure 44. Normal quartile plot (A), box-plot (B), and histogram with normal fit (C) of resonance frequency values for a lot of planar inductor sensors.

3.8.3 Influence of Sensor Aspect Ratio

To evaluate the impact of aspect ratio on the resonance characteristic of planar inductors, circuits ranging from 8 to 9 mm by a step of 0.5 mm in length were engineered (Figure 45A). As sensor aspect ratio (sensor length divided by sensor width) was increased, resonance frequency dropped (Figure 45B). The reduction in resonance frequency may be a result of increased parasitic capacitance in the sensors with greater aspect ratio. Peak magnitude increased with aspect ratio, likely due to increased coupling area between the sensor and detection coil (Figure 45C). As

expected, quality factor of the sensors was reduced with increased aspect ratio which can be contributed to increased parasitic resistance due to greater lengths of circuit traces. Interestingly, all sensors employing the coil stacking technique, had higher frequency peaks observed at approximately 4.7-4.8 times the resonance frequency for the second peak and approximately 10.6-10.7 times the resonance frequency for the third peak. These higher frequency peaks may be attributed to the mutual inductance behavior among the inductors in the equivalent circuit (see Figure 11) and further investigation is needed to determine if useful information can be garnered from the additional peak such as providing calibration constants.

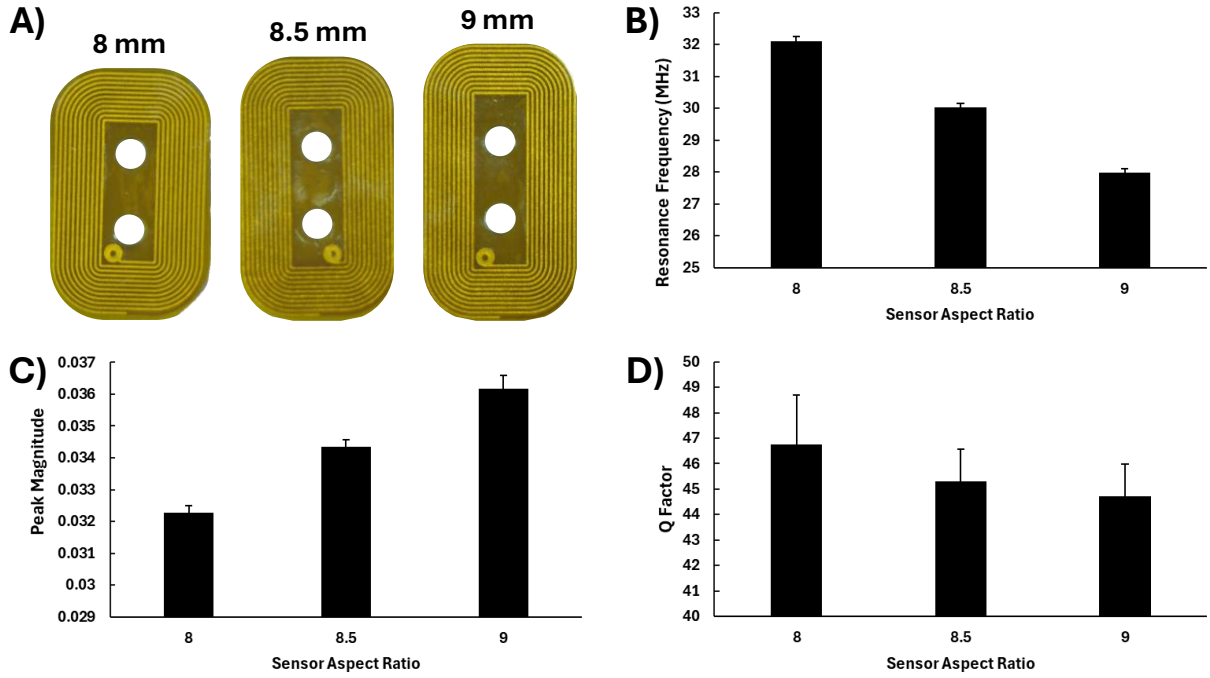

Figure 45. Sensors of varying length to study the impact of aspect ratio on sensor resonance metrics (A). The impact of aspect ratio on measured sensor resonance frequency (B), peak magnitude (C), and quality factor (D). *Error bars represent standard deviation of the mean (n = 3 measurements of the same sensor).*

3.8.4 Sensor Bending and Finite Element Analysis (FEA)

Differences in sensor substrate geometries were first investigated with finite element analysis (FEA) to engineer sensor shape best suited for bending with applied suture loading to provide optimum force sensitivity without premature signal saturation. Static structural simulations in FEA software (Ansys Workbench; Ansys, Canonsburg, PA, USA) were performed on the sensor backing material structure composed of PEEK with a Young's modulus of 3.6 GPa and a Poisson's ratio of 0.36 [71]. The material was assumed to be linearly elastic over the applied loading range. Any effects of the adhered flexible circuit pattern sensor body deformation were not included in the simulations. Tetrahedral elements with a maximum size of 0.54 mm were used to generate sensor substrate model meshes. During loading simulations, a ramped 10 to 50 N force was applied to the area of suture-graft construct contact.

Since the load sensing mechanism is based on bending of the circuit pattern, FEA simulations were utilized to evaluate the mechanics of the sensor substrate under loading. Analysis of sensor FEA loading simulations indicated that 40 N of loading (highest ideal UCLR graft tension) led to a maximum of about 0.34 mm in displacement of the middle of the sensor 0.75 mm thick structure in the direction of applied load (Figure 46A). The strain along the longitudinal direction of the sensor substrate was also evaluated (Figure 46B). By modifying the geometry of sensor substrate, varying loading range can be tuned for different tendon or ligament reconstruction applications. For example, increasing the thickness or width of the sensor substrate increases the loading magnitude required to achieve the same deformation, allowing the sensor to function at a higher loading range. Furthermore, the suture hole sizing and spacing could be altered to either concentrate or dissipate the load.

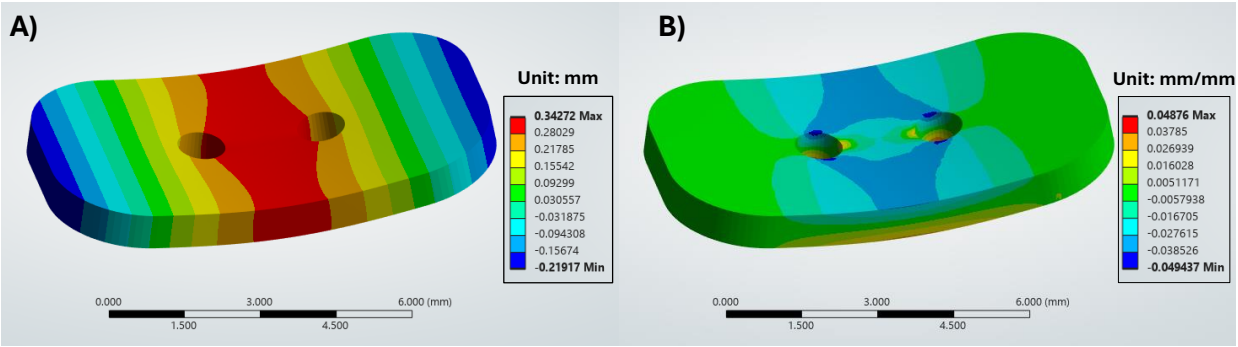

Figure 46. Simulated deformation in the direction of applied load of the 0.75 mm thick sensor substrate (A) and strain in the longitudinal direction of the sensor substrate (B) at 40 N of loading.

3.8.5 Suture Tension Detection

Ideal UCL graft tension ranges from 20 to 40 N during reconstruction surgery [33]. Therefore, to detect under- and over-loading conditions the operating force measurement range of the sensor was desired to be 10 to 50 N. To characterize sensitivity and detection ranges for each sensor design, static tensile loading was applied from 10 N to 50 N by a step of 5 N with a mechanical tester (ElectroForce 3200; TA Instruments, New Castle, DE, USA) (n = 3) (Figure 47). Sensors were placed in a custom 3D printed holder and United States Pharmacopeia size #2 polyester braided sutures (Ti-Cron; Covidien, Dublin, Ireland) were threaded through the sensor structures for all loading tests. A 62.5 N pre-stress (125% maximum detection load) was applied for 5 minutes to reduce the impact of plastic deformation on sensor operation. Sensor repeatability and reproducibility were both evaluated during mechanical testing. Deformation during loading of the sensor and sutures versus only sutures were also recorded to quantify changes in displacement with sensor bending. Cyclic loading with the mechanical testing system was also utilized to assess drift in sensor performance over 10^4 loading cycles by ramping loads between 10 N and 50 N at a rate of 10 Hz. Additionally, to determine the impact of loading angle on the sensor operation,

sutures were placed at maximum angles of off-axis loading expected in a UCLR humeral bone tunnel (~16 degrees) in both the transverse and longitudinal directions during mechanical testing from 10 to 50 N by a step of 5N.

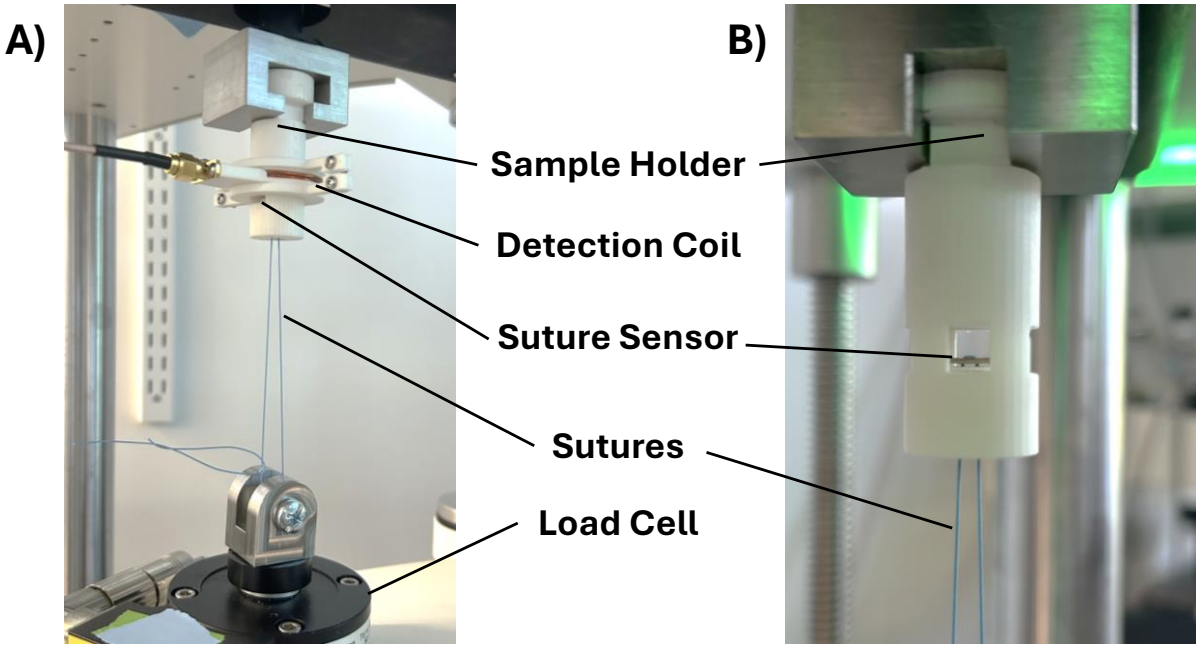

Figure 47. Mechanical testing set-up for evaluating the sensor response to loading (A). Close up image of a suture sensor within the sample holder (B).

Sensor circuits were engineered to resonate near 28.25 MHz $\pm$ 0.14 MHz (n = 35) and fall within the high frequency portion of radiofrequency spectra (3-30 MHz). This frequency range was selected to maximize signal transmission through biological tissues in order to increase detection depth [55]. Mechanical testing of the suture accessory sensor indicated that suture loading from 10 N to 50 N was directly related to changes in the sensor resonance frequency (Figure 48A). The sensitivity of the 0.75 mm thick sensor was 0.0051 MHz/N and the full-scale output (FSO) was 0.21 MHz. Suture loading was indirectly related to the measured peak magnitude (reflection coefficient value at the resonance frequency) of the sensor (Figure 48B). To evaluate

the impact of sensor substrate thickness on sensitivity, loading characterization was completed with both 0.75 and 1 mm thick sensor substrates. Increasing substrate thickness from 0.75 to 1 mm reduced sensitivity by nearly 40%. Specifically, the sensitivity of the 1 mm thick sensor (0.0031 MHz/N) was lower than the 0.75 mm thick sensor (0.0051 MHz/N) over the tested loading range, therefore the 0.75 mm sensor was utilized for further testing (Figure 48C). Sensitivity testing of multiple 0.75 mm thick sensors showed one of three sensors had lower sensitivity suggesting improved manufacturing techniques are required to produce consistent sensors in later studies (Figure 48D). The impact of varying the distance between the sensor and detection coil during mechanical testing was also evaluated and revealed the coil could be placed up to 8 mm above the sensor before changes in sensitivity measurements were observed. To comply with UCLR method evaluation protocols, the sensor should withstand at least 10^3 cycles, therefore cyclic loading with the mechanical testing system was also utilized to assess drift in sensor performance over 10^4 loading cycles [61, 62]. Results indicated that sensitivity was not altered after 10^4 loading cycles from 10 to 50 N (Figure 48E). However, the baseline resonance frequency at 10 N of loading increased by 0.18% after 10^4 loading cycles (Figure 48F). This 0.18% increase corresponded to approximately 22% of the sensor FSO representing sensor baseline frequency drift over 10^4 loading cycles. Considering ten times the number of loading cycles were used to evaluate repetitive loading of the sensing platform compared to other suture accessories in the UCLR literature, drift in baseline frequency may be lower when only loaded to 10^3 cycles. Drift in sensor baseline frequency with repetitive loading may be attributed to fatigue in the PEEK substrate material during cyclic testing, but further evaluation is required to determine the root cause. While these results demonstrated repeatable trends in sensor response under the tested conditions, the limited

sample size should be considered preliminary and larger-scale studies are needed to evaluate variability across specimens, sensors, and reconstruction conditions.

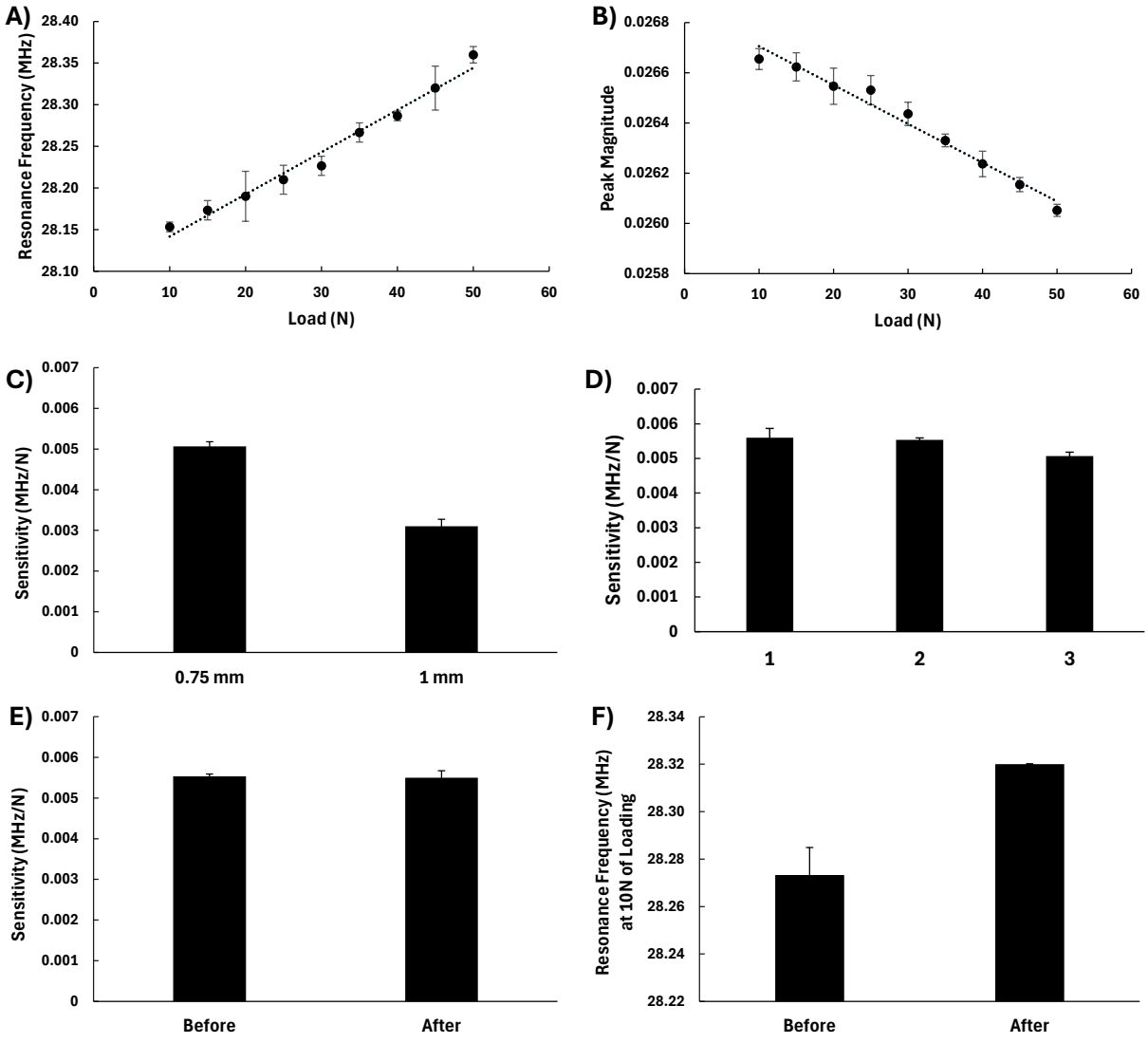

Figure 48. A strong linear trend ($R^2 = 0.98$) was observed for a 0.75 mm thick sensor between load ranging from 10 to 50 N and measured resonance frequency (A). Magnitude of the reflection coefficient value at resonance frequency versus load ranging from 10 to 50 N demonstrating a linear trend ($R^2 = 0.98$) (B). The sensitivity of a 1 mm thick sensor was lower than a 0.75 mm sensor (C). Sensitivities of three 0.75 mm thickness sensors, Sensor 1, Sensor 2, and Sensor 3,

labeled as 1, 2, and 3, respectively (D). There were no noticeable differences in sensitivity before and after 10^4 cycles of loading (E) but baseline resonance frequency at 10 N of loading increased after 10^4 cycles of loading (F) for a 0.75 mm thick sensor. *Error bars represent standard deviation of the mean (n = 3 measurements of the same sensor).*

Since sensor deployment in a UCLR involves anchoring grafts in regions native to the UCL, some off-axis loading is expected within the bone tunnel in UCLR applications. Therefore, off-axis loading in both the X and Y directions of the sensor were evaluated due to the lack of axisymmetric sensor geometry (Figure 49A). Specifically, off-axis loading of 16 degrees was tested as it represented the worst-case angle scenario (i.e., short bone tunnel with maximum suture displacement to the edge of the bone tunnel during off-axis loading). Results indicated a lower sensitivity for off-axis loading in the X direction (0.0039 MHz/N) when compared to both on-axis loading (0.0056 MHz/N) and off-axis loading in the Y direction (0.0052 MHz/N) (Figure 49B). Given the aspect ratio of the sensor circuit, it was anticipated off-axis loading in the X direction would have a greater impact than in the Y direction. With bone tunnel placement and sensor accessory integration in UCLR most off-axis loading would be expected in the Y direction.

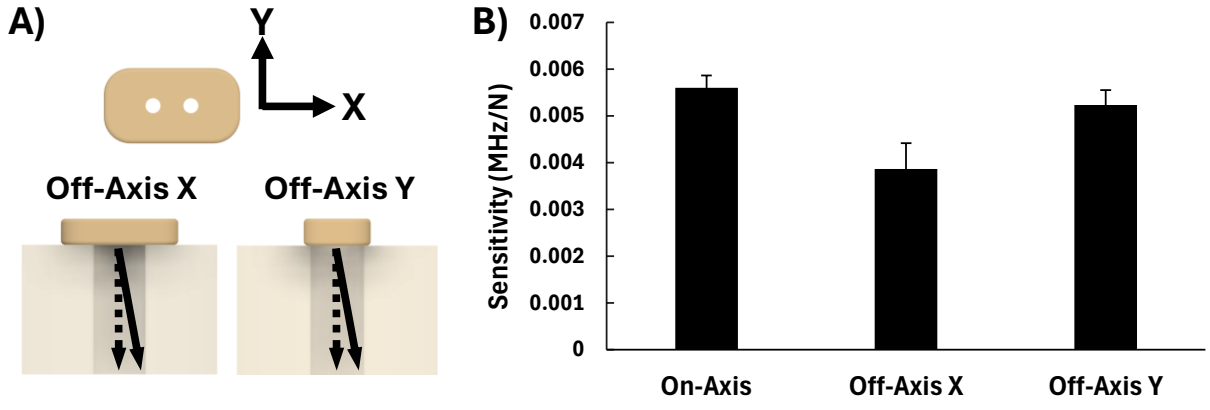

Figure 49. Schematic of off-axis suture loading in the X and Y directions showing suture positioning in bone tunnel (A). Results indicated a lower sensitivity for off-axis loading in the X direction when compared to both on-axis loading and off-axis loading in the Y direction (B). *Error bars represent standard deviation of the mean (n = 3 measurements of the same sensor).*

3.8.6 Temperature Testing

It is well known that temperature and humidity impact the resonance characteristics (i.e., resonance frequency, signal magnitude, and quality factor) of LC sensors, especially planar inductor platforms [57]. Therefore, initial thermal characterization was performed on the sensing platform by varying temperature from 20 to 40 °C by a step of 2 °C from 20 °C (room temperature) to 30 °C and a finer resolution step of 1 °C from 30 °C to 40 °C (range containing body temperature). Results indicated resonance frequency decreased with increasing temperature according to a second-order polynomial fit (R^2 = 0.996) (Figure 50A). Peak magnitude at resonance also decreased with increasing temperature according to a second-order polynomial fit (R^2 = 0.997) (Figure 50B). A small deviation from the relationship between temperature and resonance frequency as well as peak magnitude was observed around 31 to 32 °C and may be due to manual temperature settings of the heating chamber. Furthermore, it was observed that spectra background signal level increased with increasing temperature which may be a result of detection coil and circuitry heating. In-depth temperature and humidity characterization of the sensor and detection device operating conditions with an environmental chamber is required to fully evaluate the thermal and moisture impacts on the sensing platform.

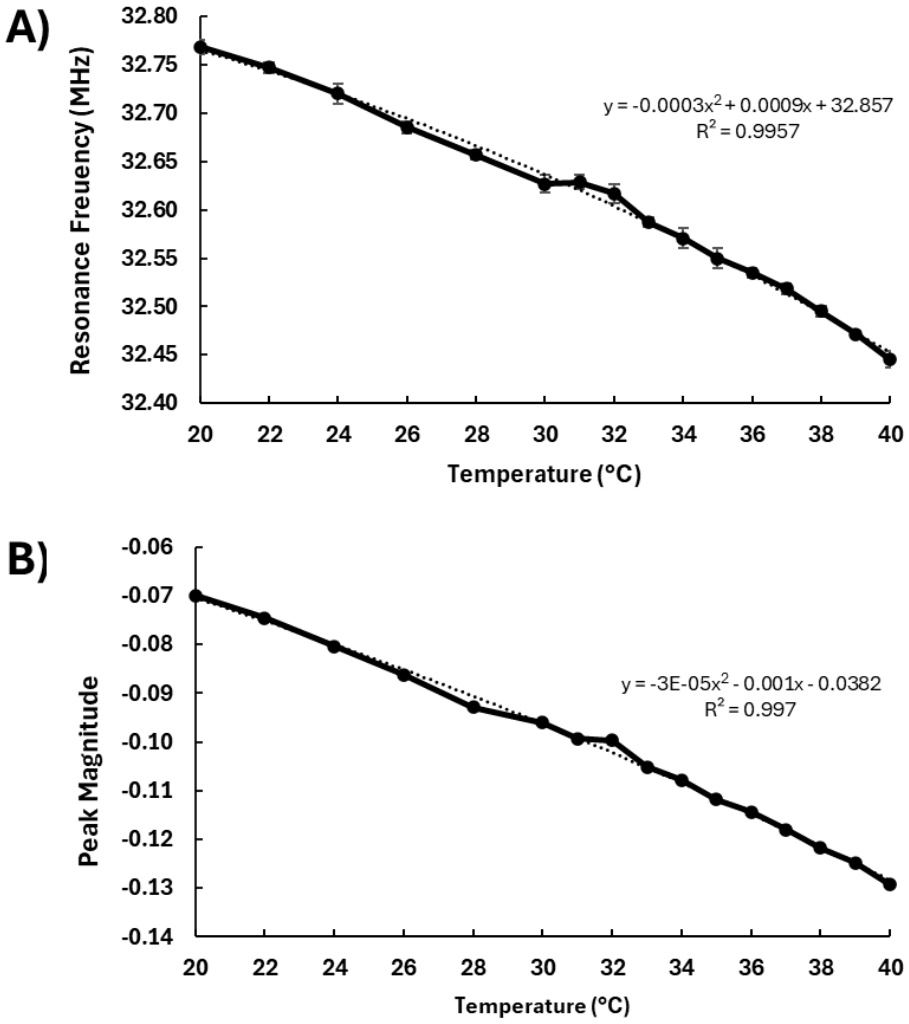

Figure 50. Change in resonance frequency (A) and peak magnitude at resonance (B) with increasing temperature. *Error bars represent standard deviation of the mean (n = 3 measurements of the same sensor).*

3.9 Limitations & Conclusions

The most significant limitation of sensor fabrication and function characterization in this study was limited sample size (n = 3). Although the studies demonstrated consistent trends in resonance response with loading, larger sample sizes will be required in future work to quantify manufacturing variability, establish statistical confidence intervals, and evaluate inter-device

reproducibility. Future work should employ sufficiently powered loading studies to generate tolerance intervals according to design input specifications and confidence and reliability levels associated with risk zone assignment in a design failure modes and effects analysis related to the sensors ability to transduce force (e.g., for a medium risk zone 2, 95% confidence and 90% reliability levels are required). Further, process capability studies should be employed to ensure sensor designs can meet desired specification ranges. Based on preliminary sensor data, sufficient sample size should be utilized to generate statistical claims and conclusions. For example, with a historical sensitivity standard deviation of $\pm$ 0.0002 MHz/N for PEEK-based sensors, a significance level of 5% and a power of 90% a sample size of 40 sensors is needed to conduct a proper analysis of variance study comparing group means. In conclusion, this chapter gave initial characterization data on determining if sensor designs can transduce changes in loading force via alterations in measured sensor resonance frequency. Specifically, sensor resonance frequency changed in response to tension loading during loading on a mechanical tester according to calibrated transfer functions. However, evidence indicated the transfer functions were only valid until a limit in off-axis loading angle and that sensor baseline frequency increased after 10^4 cycles of loading. Further, sensor baseline resonance frequency was also shown to be impacted by temperature conditions and is likely also further impacted by humidity levels and condensing moisture according to the literature. Therefore, future design of experiments studies are needed to perform sensor operating conditions testing where temperature and humidity conditions are varied to evaluate the isolating effects of sensor encapsulation approaches (i.e., optimizing encapsulation material, methods, and thickness).

Chapter 4: Engineering an LC Sensor Detection Device

Content of this chapter are adapted from:

Meyers K, Ong K (2026) “A Wireless, Passive Sensor to Monitor Intra- and Post-Operative Graft Loading in Reconstructed Medial Ulnar Collateral Ligaments.” In-preparation.

Author contributions

Conceptualization: KM, KO

Data Collection and Analysis: KM

Interpretation: KM, KO

Writing and Editing: KM, KO

4.1 Introduction

To wirelessly record implanted sensor data, a custom detection device was engineered to produce a frequency-varying alternating current electromagnetic field to measure an impedance spectrum from the sensor and remotely transfer resonance spectra data to a computer via Bluetooth or a serial USB connection (Figure 51A). The device was specifically designed for postoperative wearable applications (Figure 51B). Overall, this chapter focuses on determining if sources of measurement error in the resonance spectra can be bounded when sensors are coupled with varying antenna designs from a wireless detection device.

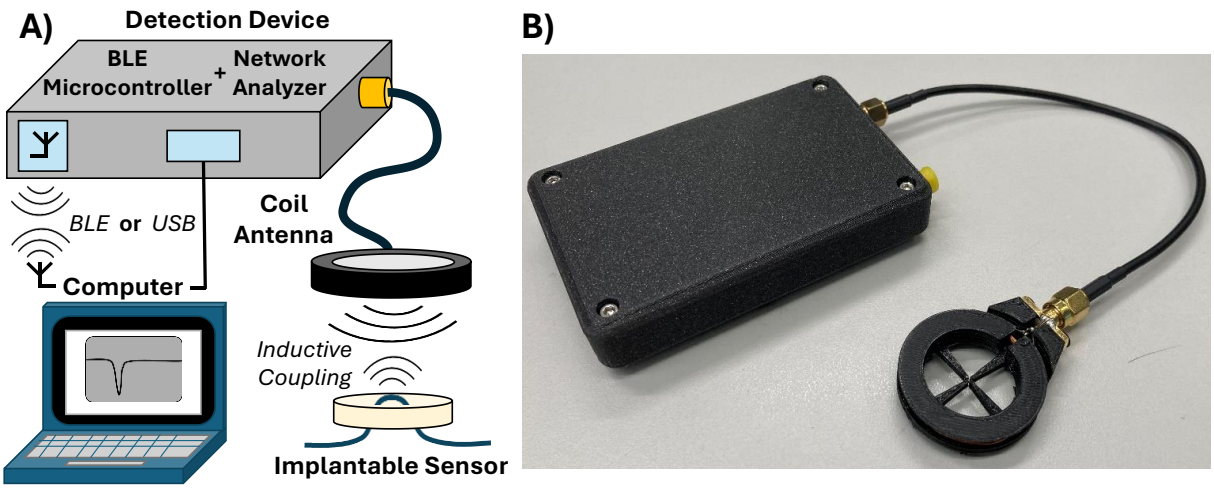

Figure 51. Schematic diagram of the detection device sending and receiving signals from a computer via Bluetooth Low Energy (BLE) or Universal Serial Bus (USB) and implantable sensor via inductive coupling (not to scale) (A). Detection device with coil antenna (B).

4.2 Detection Device Design Clinical Feedback

4.2.1 Voice of Surgeon

Since a handheld version of the detection device was out of the scope of the thesis work (other lab members focused on a handheld design for operation use case environments), surgeon feedback on the wearable detection device was not obtained.

4.2.2 Voice of Physical Therapist

Physical therapist feedback on various aspects of the wearable detection device (e.g., size, shape, and weight, software interfaces) was obtained and incorporated into the design of the user interface layout, graphics, features, and options. It was also determined that a phone and/or tablet interface was desired over a computer application to facilitate portability. Specifically, preferences on graphic displays of the loading data and data storage were collected.

4.2.3 Voice of Regulatory Consultant

According to consulting experts, the largest regulatory burden resides in software documentation. Specifically, documentation burden is high when wireless communication is involved (e.g., Wi-Fi, Bluetooth) and connects to third-party devices (e.g., phone, tablet, computer). Therefore, the detection device was designed to operate with both wired serial and wireless Bluetooth capabilities.

4.3 Detection Device Design Considerations

4.3.1 Wearable Detection Device Size & Weight

Detection device size should be compact and light enough to be worn on the upper arm during physical therapy exercises.

4.3.2 Detection Range

Since sensor placement in a UCL reconstruction application is at the humeral medial epicondyle, a minimum sensor detection distance of 3 mm through superficial tissues is required.

4.3.3 Connection Range

For a post-operative use case environment, the detection device should be able to connect over BLE to a computer or phone application in the same room. It should also be noted that sources of path interference in the form of walls, body tissue, humidity, etc. can influence communication ranges and reliability.

4.3.4 EMC, EMI, and ESD Regulations

In accordance with IEC 60601, the detection device must pass electromagnetic interference (EMI), electromagnetic compatibility (EMC), and electrostatic discharge (ESD) testing.

4.3.5 Battery Life

For a post-operative use case environment, the detection device battery life should last for the duration of a physical therapy session (1-2 hours) before needing recharging.

4.3.6 Sampling Rate

A sampling rate of 10 Hz (10 samples a second) is desired for sensor recordings during dynamic physical therapy exercises. However, sampling rate will be lower if implementing BLE connections compared to wired, serial communication.

4.4 Fabrication of Detection Device

A wearable detection device was engineered with a microcontroller, detection coil, miniaturized network analyzer, and user interface circuitry to provide information on suture loading force measured by the implanted sensor (Figure 52). The device was programed to remotely output suture loads from the sensor to a computer app with Bluetooth Low Energy. This device will be worn by the patient to pick up sensor readings and send them to a mobile device or computer. Specifically, a computer or mobile phone controls sweep frequency ranges of a miniaturized network analyzer by establishing a Bluetooth Low Energy connection with a microcontroller via a computer or phone app. Data points from the network analyzer frequency sweeps will then be collected and sent back to the computer or mobile phone over the Bluetooth Low Energy connection for interpretation. Major components of the excitation and detection system and their functionalities are outlined below:

Network Analyzer: A vector network analyzer (VNA) capable of performing 50k-1.5GHz frequency sweeps on the implanted sensor (NanoVNA H4).

BLE Microcontroller: A microcontroller with Bluetooth Low Energy capabilities (NanoBLE 33; Arduino, Turin, Piedmont, Italy).

Excitation & Detection Coil: A custom-built inductor coil antenna to perform electromagnetic coupling with the implanted sensor.

Power Supply: A 3.7V lithium-ion polymer battery to give power to the wearable device.

Visual Studios C# Programming Software: Enables programming of the frequency sweep settings of the network analyzer and reading datapoints from the network analyzer via Bluetooth Low Energy. This functionality is integrated into a computer app with a graphical user interface (buttons, textboxes, graphics, etc.) for research and patient/therapist utilization.

Arduino Integrated Development Environment Software: Enables programming of the BLE microcontroller chip set.

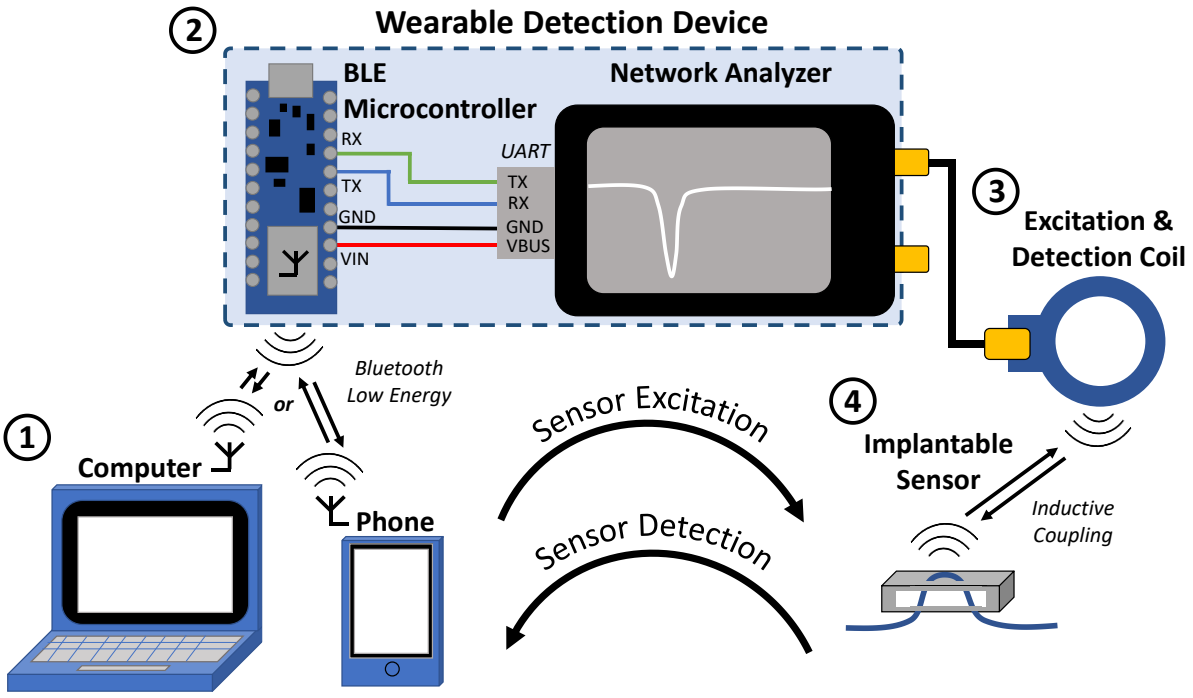

Figure 52. Schematic showing connectivity among wearable device components and the implantable sensor. A computer or mobile device (1) communicates with the wearable detection device (2) over Bluetooth Low Energy so that the excitation and detection coil (3) receives loading data from the implantable sensor (4) that can be processed by a computer or phone app.

The wearable device components were successfully assembled and placed in a custom housing fabricated with 3D printing (Figure 53). The device was integrated into commercially available knee, shoulder, and ankle braces via Velcro attachments (Figure 54). Wearable elastic bands containing Velcro were also designed to be compatible with the device as option for physical therapy exercises that do not require braces.

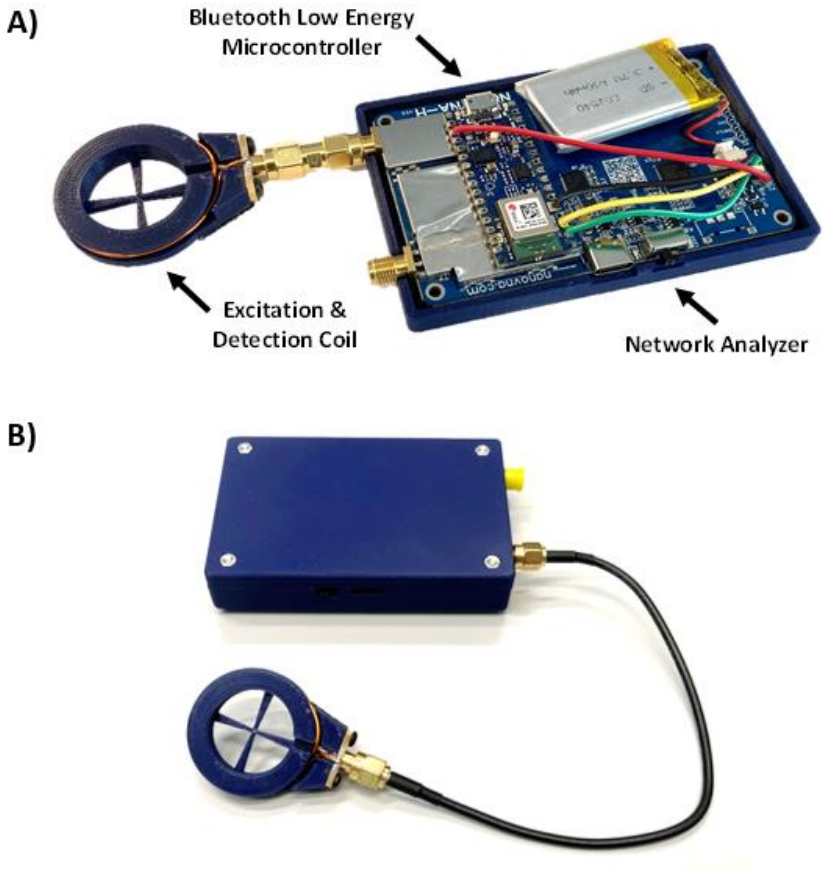

Figure 53. Detection system device major components (A) and assembly (B).



Figure 54. Wearable detection system device incorporated in a knee (top left), shoulder (bottom left) and ankle brace (right).

A computer app with a graphical user interface was developed for research use with a C# programming language in a software development program (Visual Studios; Microsoft) to control the wearable detection device (Figure 55). The researcher app version contains advanced functionality (frequency sweep settings, background subtraction buttons, calibration options, detailed graphs, etc.) that was useful in the design and testing of implantable sensors. A version of the app utilized by patients and healthcare professionals would show a simplified interface with basic functionality (i.e. connection button, progress messages, battery level, and a basic force graphic) based on human factors engineering feedback.

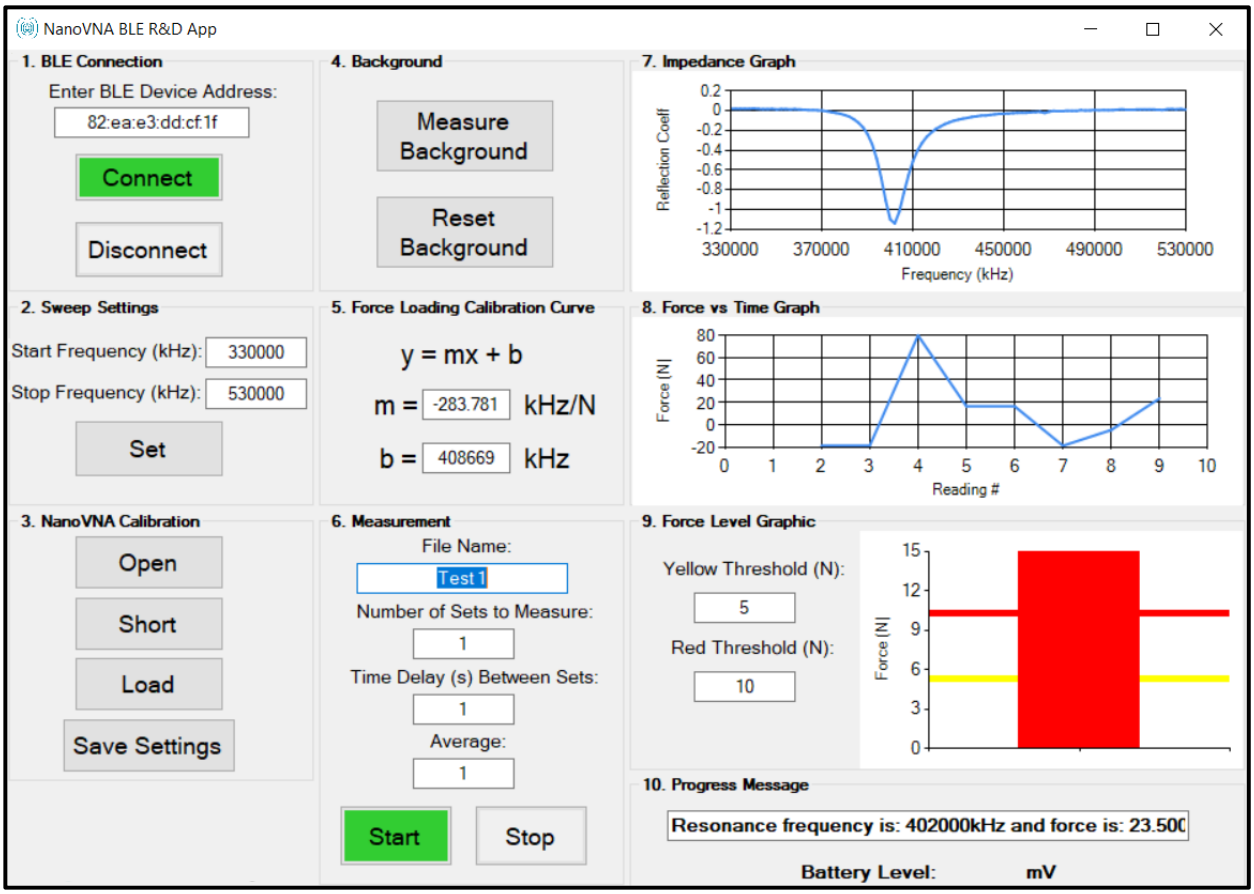

Figure 55. Graphical user interface of computer app designed for research use.

The computer application that was used to communicate with the wearable detection device was programmed to continuously record sensor data with a sampling rate of 1 reading every 3 seconds. Sampling rate can be increased by tripling the serial communication speed (38400 to 115200 bits/second) between the Bluetooth Low Energy microcontroller and network analyzer as well as reducing the number of measured points and decimal places by modifying network analyzer firmware. Additionally, the sampling rate could be increased by programming the wearable detection device to only send the measured resonance frequency (2 bytes of data) over a Bluetooth Low Energy connection, rather than sending 100 points of raw data (200 bytes of data).

Further, the network analyzer firmware could be modified to increase sampling rates prior to serial or wireless transmission.

The battery life of the wearable detection device lasted about 4 hours in a pre-connection state (i.e., the device was powered on, waiting for a connection, but no measurements were being taken or data transmitted) using a rechargeable 350mAh lithium polymer battery. When measuring and transmitting data, device power consumption could be more or less, therefore battery life during continuous device operation is likely different and further testing is needed to characterize battery life during non-stop recording sessions. Minimally, the device needs to operate for 1 to 2 hours to be sufficient for most physical therapy sessions. By utilizing a battery with a higher mAh rating, the battery life of the device could be extended, however increasing the mAh of a battery typically involves also increases the size and weight of the battery which negatively impacts the form factor of the wearable detection device. The current size of the detection device is 6 x 10 x 1 cm and the weight is 80g with the battery. Redesigning the printed circuit board and removing excess electronic components reduced circuit board area by 49% (Figure 56**)**. Due to regulatory and software update hurdles associated with existing phones, tablets, and computers, a prototype device was also wired and programmed to receive force readings over a wireless BLE connection as a potential alternative (Figure 57).

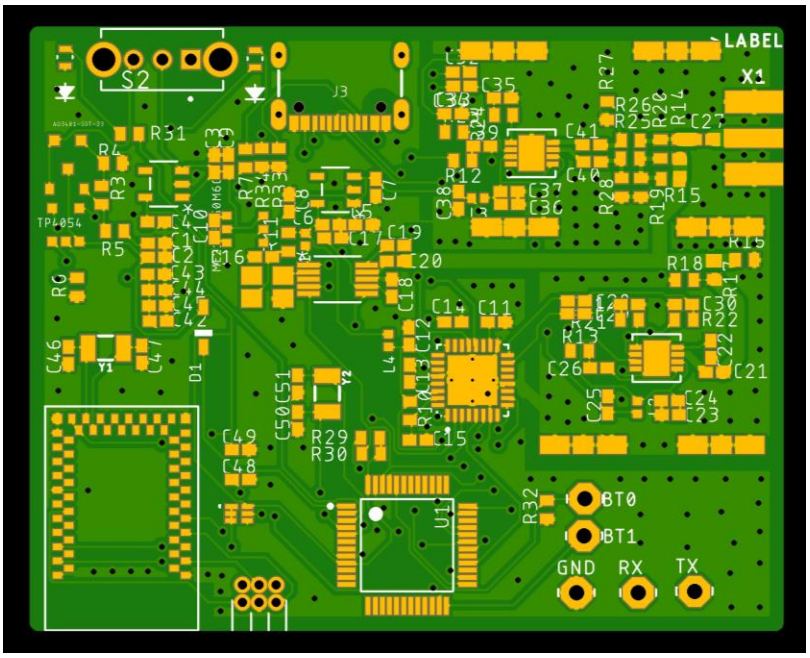

Figure 56. Redesigned wearable detection device circuit board integrating measurement circuitry with BLE microcontroller.

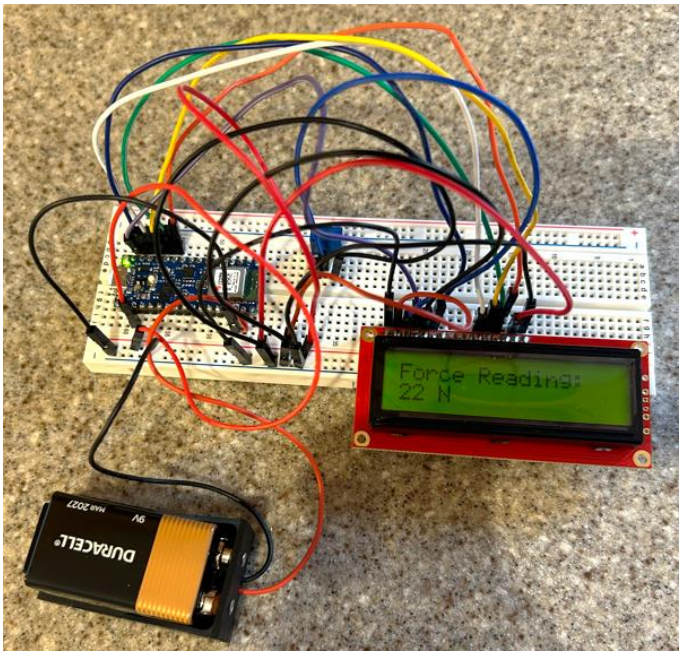

Figure 57. Prototype remote display device to receive wearable detection device force readings over a BLE connection.

4.5 Detection Device Testing

4.5.1 Connection Distance

Received signal strength indicator (RSSI) was measured as a function of distance between the wearable detection device containing the Bluetooth Low Energy transmitter and an iPhone receiver (Figure 58). All measurements were performed through air at normal atmospheric conditions with 2-foot increments. The maximum connection distance was 28 feet which is consistent with limitations described for Bluetooth Low Energy modules. This maximum connection range is suitable for most indoor and outdoor physical therapy settings. RSSI values around -100 dBm are considered poor for data transmission and reception. As RSSI decreases with distance, communication performance between the transmitter and receiver is negatively impacted through increases in bit error rates. Further testing using bit error rate measurement techniques could be utilized to better understand the influence of distance on the wireless communication between the wearable detection device and a computer or phone. It should also be noted that sources of path interference in the form of walls, body tissue, humidity, etc. can also influence communication ranges and reliability. The wearable detection device case did not have any measurable effects on signal strength.

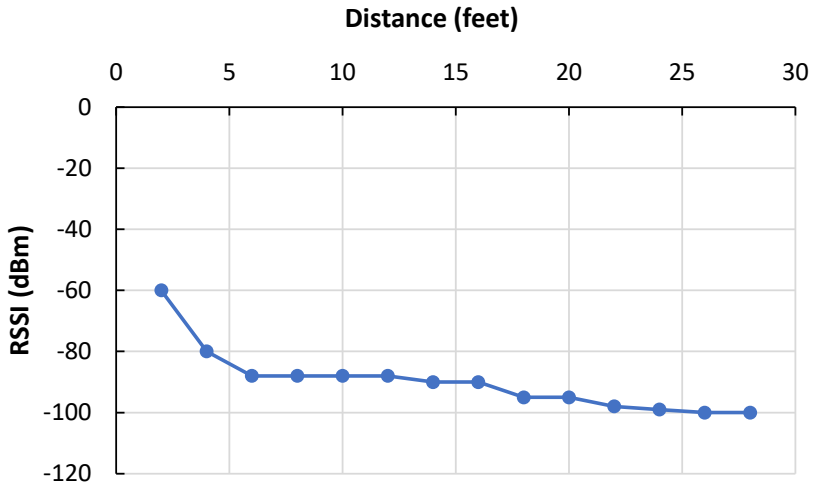

Figure 58. Measured received signal strength indicator (RSSI) as a function of distance between Bluetooth Low Energy transmitter on wearable detection device and a phone receiver *(n = 1)*.

4.5.2 Antenna Optimization

Since antenna design influences detection area, depth, and quality, optimization of detection coils was performed. For planar inductor detection coils, the trace thickness and spacing as well as shape were varied (Figure 59). Planar inductor coils were sufficient for sensor proof-of-concept studies, but to increase detection coupling area, inductor coil designs were preferred. Therefore, a design of experiments study was conducted varying detection coil diameter, wire diameter (i.e., gauge), and turn number (Table 3) to optimize antenna design.

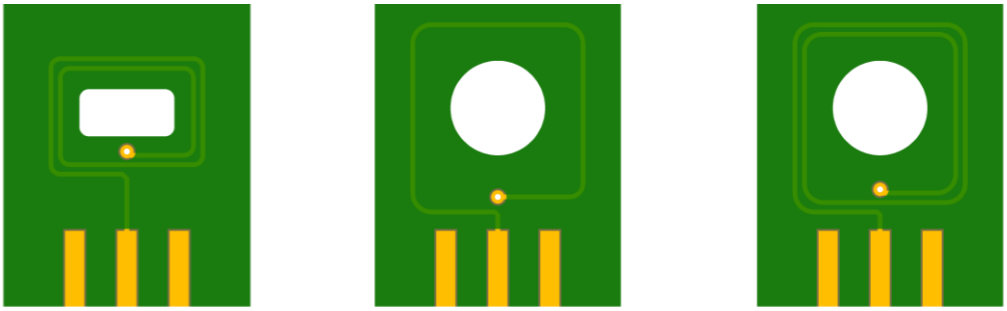

Figure 59. Example of variations in detection antenna planar inductor designs covering differences in trace shape, thickness, and turn number.

Table 3. Antenna design comparison.

Antenna #	Diameter	Gauge (AWG)	Turn #
1	30	18	2
2	30	18	4
3	40	18	2
4	40	18	4
5	40	14	2
6	50	18	2
7	50	18	3

Each antenna design was tested at a displacement distance of 3 mm from a rounded stacked LC sensor while observing variations in measured resonance frequency, peak magnitude, and quality factor (Figure 60). Given Antenna #1 (2-turn, 18-gauge coil with a diameter of 30 mm) provided the best signal strength, it was selected for all subsequent experimental studies.

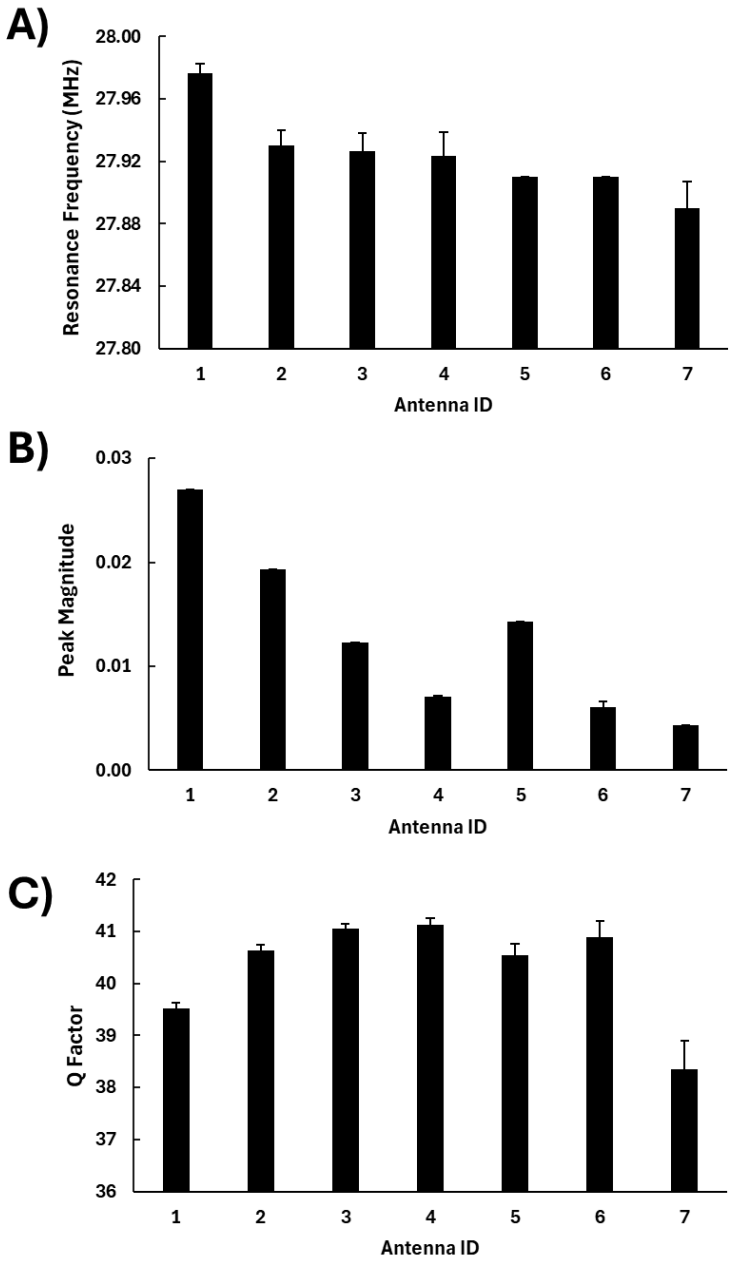

Figure 60. Comparison of antenna design sensor coupling with measured resonance frequency (A), peak magnitude (B), and quality factor (C). *Error bars represent standard deviation of the mean (n = 3 measurements of the same sensor).*

4.5.3 Resolution & Stability Testing

Baseline noise of the detection device was quantified during stability testing to determine the detection resolution of the system near the sensor frequency operation range. With the detection device set to spans of 1, 3, and 10 MHz respectively, average and standard deviation in resonance frequency, quality factor, and peak magnitude sensor readings were quantified (n = 100) (Figure 61). Rounded to the resolution of the detection device, the 1 MHz span standard deviation was $\pm$ 0.01 MHz which was consisted with the network analyzer's specifications. Signal averaging (n = 5) was also utilized during sensor testing to reduce the impact of noise on sensor readings. Observing a run chart of the sensor recordings indicated no clustering or grouping of points ($p=0.791$), trends or sustained drift in the data ($p=0.212$), and oscillation or data fluctuating up and down ($p=0.788$). Due to device resolution setpoints, raw data during stability testing was tied but with greater than 5 groupings. However, Ryan-Joiner testing still indicated the data did not pass normality assumptions ($p<0.05$). Therefore, nonparametric approaches with sample sizes greater than n = 93 need to be utilized to generate tolerance intervals with 95% confidence and 95% reliability assuming the classification of risk associated with resonance frequency measurement accuracy is moderate according to ISO 14971.

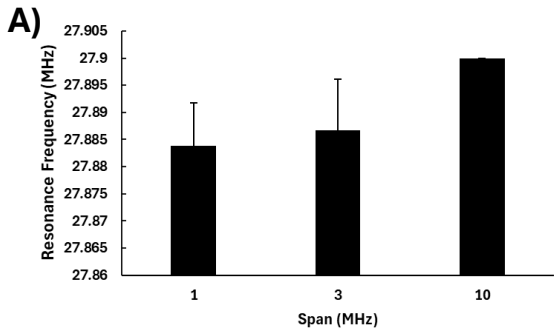

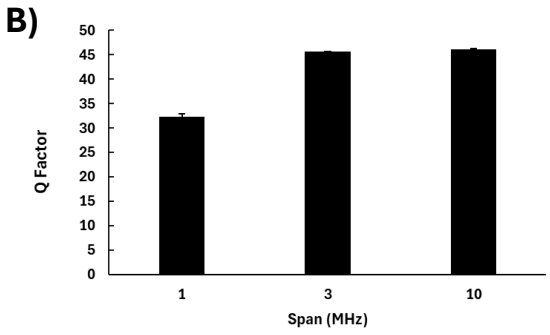

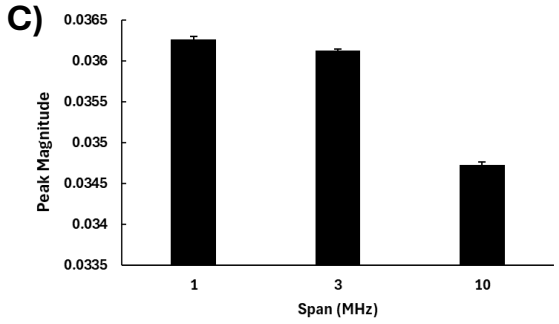

D)

Standard Deviation			
Span (MHz)	Q-Factor	Resonant Frequency (MHz)	Peak Magnitude
1	0.516856	0.007886	3.89E-05
3	0.061449	0.009434	2.22E-05
10	0.094809	5E-14	4.11E-05

Figure 61. At span settings of 1, 3, and 10 MHz measured resonance frequency (A), quality factor (B), and peak magnitude (C) were recorded. The standard deviation in measured metrics across span settings was also compared (D). *Error bars represent standard deviation of the mean (n = 100 measurements of the same sensor).*

4.5.4 ESD, EMC, & EMI Testing

A third party was utilized to conduct initial electrostatic discharge (ESD), electromagnetic compatibility (EMC), and electromagnetic interference (EMI) testing following IEC 60601 standards. Specifically, ESD testing involved simulating electrostatic shocks that may be present in the device use case environment (e.g., professional medical facility, at-home healthcare setting, etc.) both during direct contact with the device under test and as a result of discharge through air. EMC testing measured the impact of radiated emissions from a medical device on the surrounding environment containing other equipment that could be suspectable to electromagnetic interference.

Conversely, EMI testing assessed the susceptibility of a device to inference in the presence of electromagnetic emissions from other equipment in the surrounding environment.

The detection device passed all ESD test conditions when utilizing 15 kV ESD air discharge and 8 kV contact discharge as immunity testing levels. However, more work on EMC shielding needs to be completed as the device emitted radiation of approximately 50.6 dBµV/m at 900 MHz which was slightly above the acceptable limit of 48 dBµV/m of radiated electric field strength following IEC 60601 (Figure 62). A preliminary assessment of EMI testing indicated temporary interference with device function at 400 and 900 MHz as well as 1.8, 2.4, and 5.5 GHz. Further evaluation of the severity of EMI on the detection device function would need to be performed to quantify the severity of interference on device operation to determine if engineering solutions are required or adding warnings indicating the impact of interference.

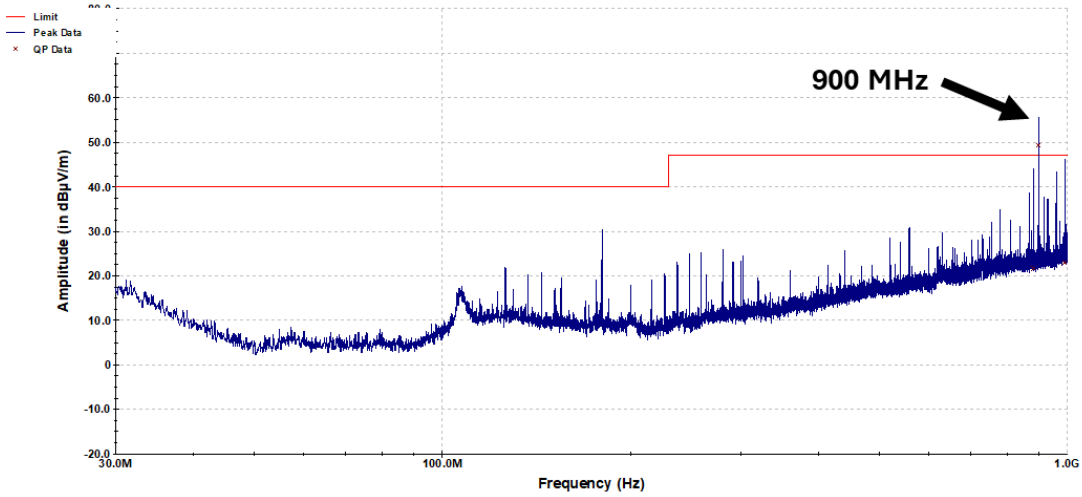

Figure 62. Electromagnetic compatibility (EMC) of the detection device test results spectra showing emitted radiation levels above threshold at 900 MHz.

4.5.5 Manual Sensor Coupling Displacement Test

Reflection coefficient magnitude measurements with the high frequency versions of the LC sensors were utilized to optimize planar inductor antenna design. Manual evaluation of sensor detection limits in air was completed by simultaneously varying vertical and longitudinal distances between the detection coil antenna and sensor (Figure 63A). Measured resonance frequency decreased with longitudinal displacement at all antenna heights (Figure 63B). Specifically, the closer the detection coil was placed to the sensor in the vertical direction, the more prominent a change in resonance frequency with longitudinal displacement. Changes in resonance frequency in response to displacement are undesirable since resonance frequency is the metric utilized to detect load with the sensor. Also measured reflection coefficient at resonance (a metric for signal amplitude) decreased with longitudinal displacement at all antenna heights as expected (Figure 63C). Again, changes in reflection coefficient amplitude were more pronounced with longitudinal displacement when the detection coil was closer to the sensor vertically.

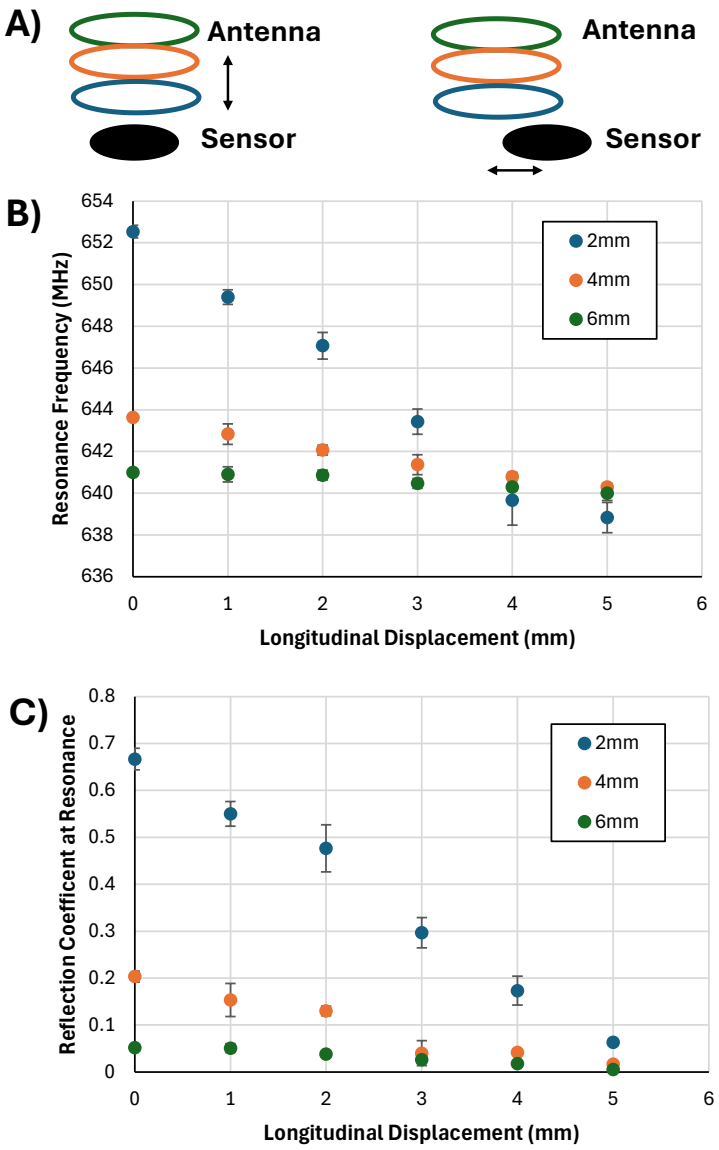

Figure 63. Schematic illustrating how the vertical and longitudinal distance between the antenna and sensor was varied to evaluate coupling behavior (A). Change in resonance frequency (B) and reflection coefficient at resonance (C) when antenna displacement is varied from 0-5 mm longitudinally for antennas placed 2, 4, and 6 mm above the high-frequency sensor. *Error bars represent standard deviation of the mean (n = 3 measurements of the same sensor).*

4.5.6 Automated Sensor Coupling Displacement Test

An automated antenna/sensor coupling testing system was developed to improve testing accuracy and time efficiency when evaluating inductor coil antenna designs with low frequency LC sensors. The set-up consisted of a custom computer application that controlled the position of the antenna relative to the sensor and mediated the readings collected from a network analyzer (Figure 64). Once programming was completed, 3D scans from the system enabled mapping of any changes in sensor signal including resonance frequency, signal amplitude, and quality factor with displacement in the X, Y, and Z directions.

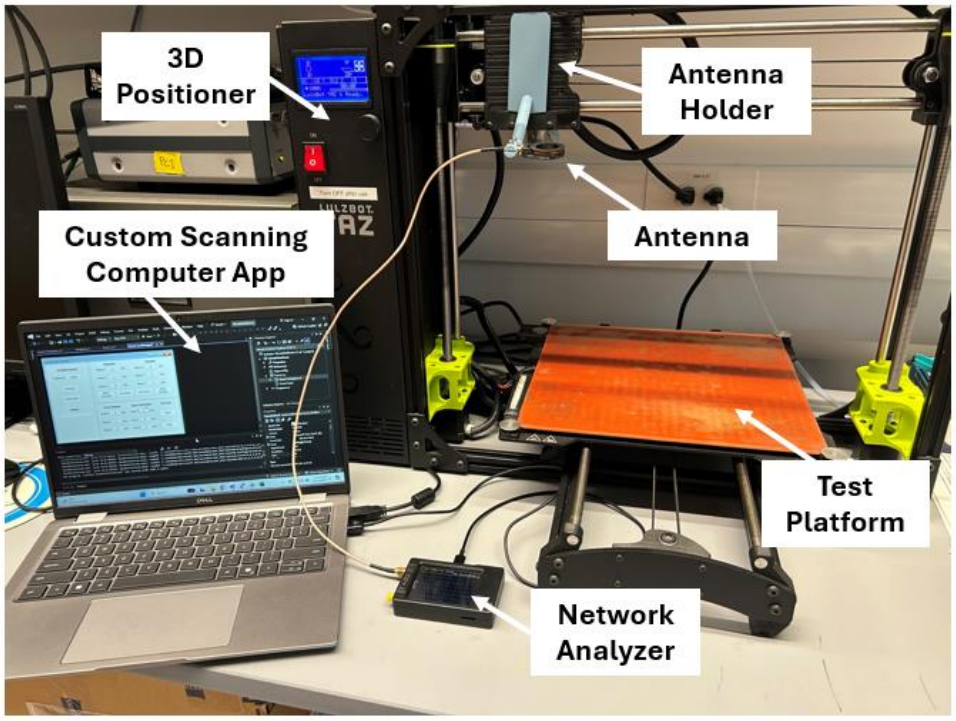

Figure 64. Image of automated sensor coupling test set up and components.

The effects of alignment between the sensor and detection coil in three different directions were determined by monitoring changes in sensor resonance spectra characteristics including resonance frequency and sensor signal transmission strength. Specifically, a custom 3D positioning

system was programmed to displace a detection coil over a sensor covering a grid pattern of 20 by 20 by 10 mm with a step resolution of 1 mm. A custom MATLAB program was coded to output 3D scans of measured reflection coefficient, resonance frequency, and quality factor at various displacement levels between the detection coil and sensor (Figure 65).

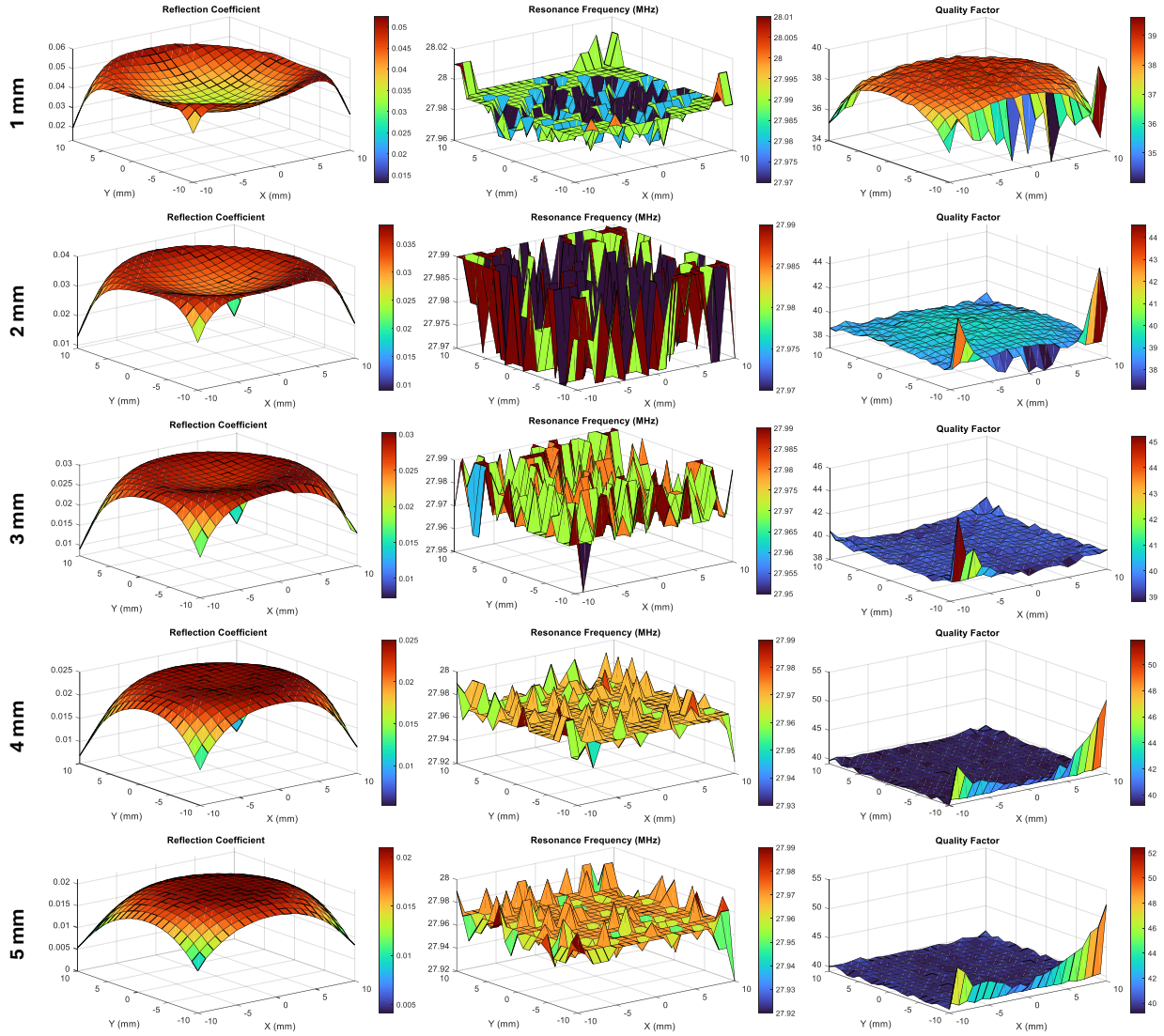

Figure 65. Scans of measured reflection coefficient (left), resonance frequency (middle), and quality factor (right) from 1 (top row) to 5 mm (bottom row) of displacement between the detection coil and sensor.

To characterize changes in signal transmission due to variations in the distance between the detection coil (30 mm in diameter) and implanted sensor as well as relative displacement during misalignment, 3D scans covering a 20 x 20 x 10 mm cube in the X, Y, and Z directions with a resolution of 1 mm in air were performed (Figure 66A). With the detection coil placed 3 mm above the sensor (in the Z direction), measured changes in resonance frequency in the X and Y directions were near the detection device resolution limit ($\pm$ 0.01 MHz with a 1 MHz span) (Figure 66B). Increasing Z displacement of the detection coil centered on the sensor from 1 to 10 mm, indicated variation in measured resonance frequency stayed near the resolution limit up until around 7 to 10 mm (Figure 66C). The value of the real reflection coefficient (peak magnitude) at resonance frequency was utilized as a metric for signal strength during 3D scans (Figure 66D). Changes in peak magnitude during X and Y displacement were similar, with peak magnitude slightly less in the Y direction compared to the X at 10 mm of displacement (Figure 66E). As Z displacement increased, peak magnitude decreased from 1 to 10 mm (Figure 66F).

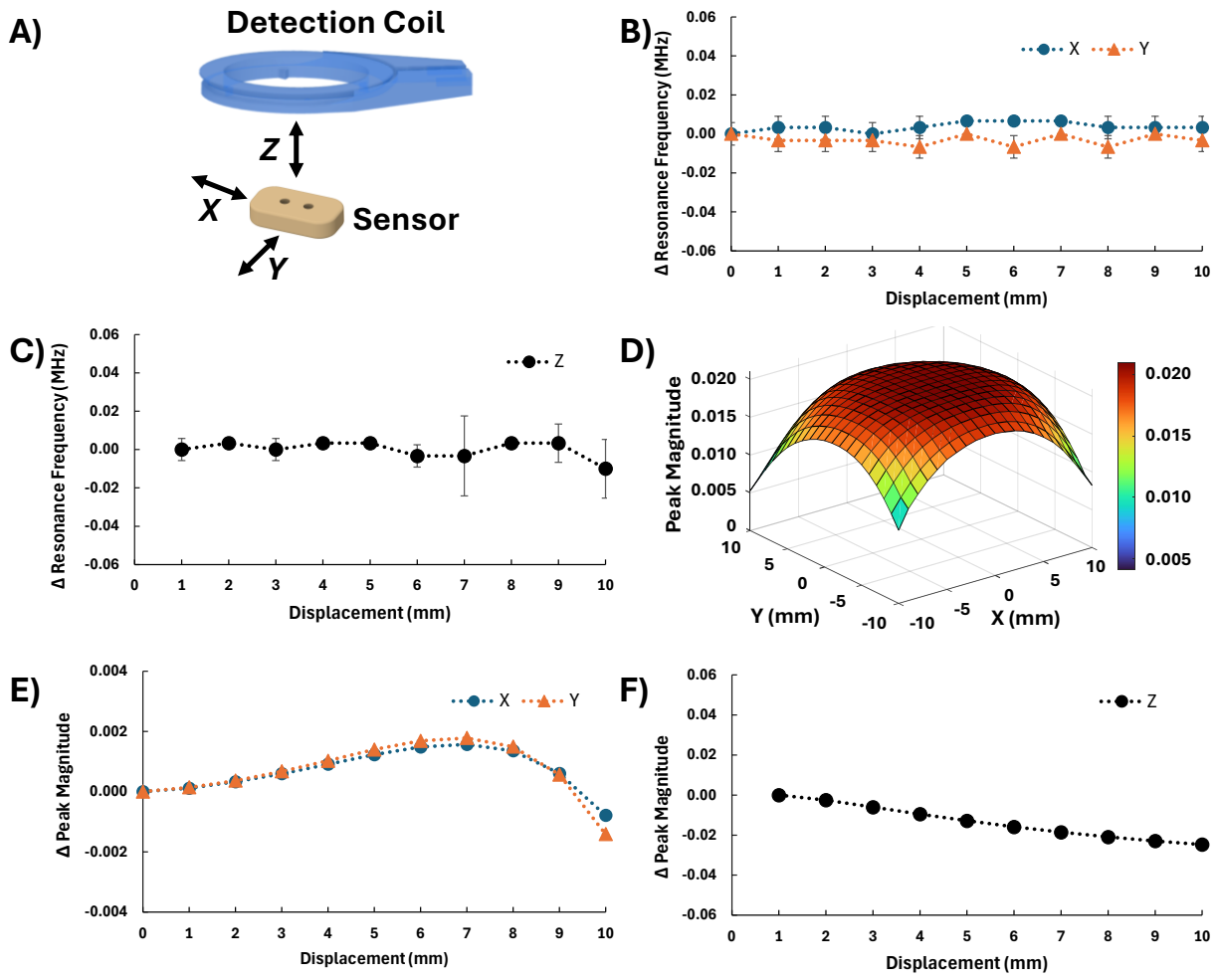

Figure 66. Schematic showing displacement directions between the sensor and detection coil (A). Changes in resonance frequency with displacement (0 to 10 mm) in both the X (blue circles) and Y (orange triangles) directions (B). Change in resonance frequency with displacement (1 to 10 mm) in the Z direction (C). A grid scan of peak magnitude at resonance in the X and Y directions at a Z displacement of 5 mm (D). Change in peak magnitude at resonance with displacement (0 to 10 mm) in both the X (blue circles) and Y (orange triangles) directions (E). Change in the value of peak magnitude at resonance with displacement (1 to 10 mm) in the Z direction (F). *Error bars represent standard deviation of the mean (n = 3 measurements of the same sensor).*

4.5.7 Rotation & Tilt Coupling Test

Since the surface of skin and the medial epicondyle at the site of sensor deployment are not perfectly parallel, changes in signal transmission due to variations in relative orientation of three axis of rotation (θ_1, θ_2, and θ_3) were varied between the senor and detection coil in air (Figure 67A). Measured changes in resonance frequency with rotation from 0 to 60 degrees about the θ_1 and θ_2 axes were near the detection device resolution limit ($\pm$ 0.03 MHz with a 3 MHz span) except at 50 degrees about the θ_2 axis (Figure 67B). As rotation around the θ_3 axis was varied from 0 to 330 degrees measured changes in resonance frequency stayed within the resolution limit (Figure 67C). As expected due to decreased coupling area, peak magnitude decreased with increasing rotation angles about the θ_1 and θ_2 axes (Figure 67D).

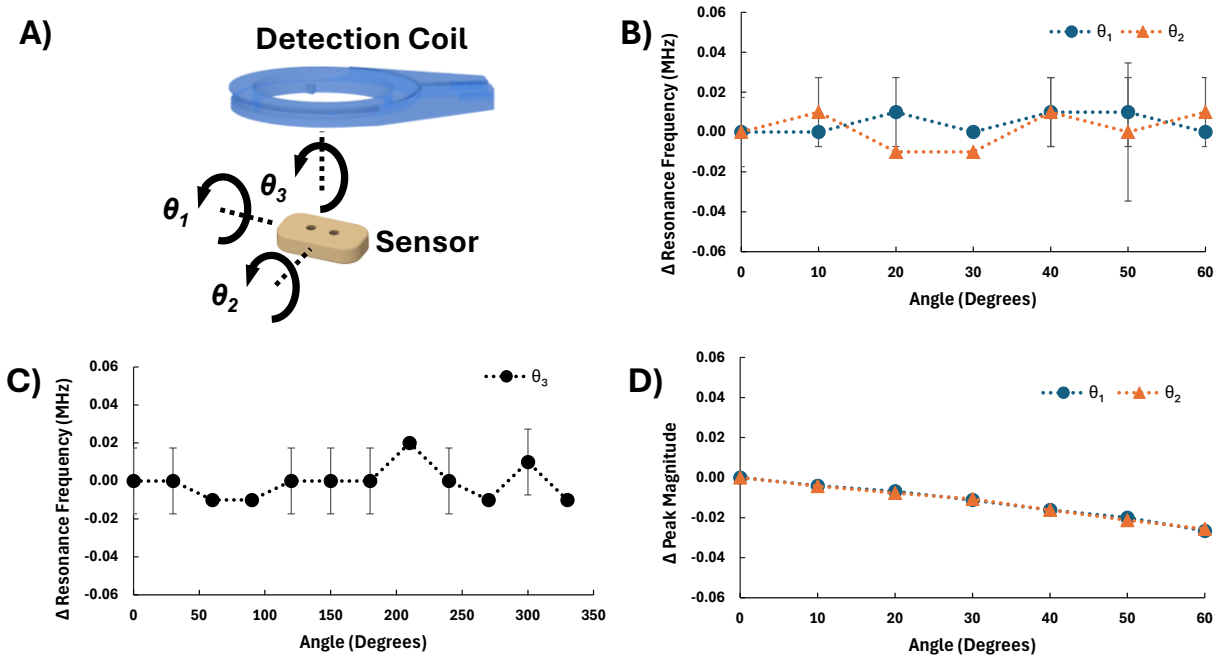

Figure 67. Schematic showing rotation directions between the sensor and detection coil (A). Changes in resonance frequency with rotation (0 to 60 degrees) in both the θ_1 (blue circles) and θ_2 (orange triangles) directions (B) Change in resonance frequency with rotation (0 to 330 degrees)

in the θ_3 direction (C). Change in peak magnitude at resonance with rotation (0 to 60 degrees) in both the θ_1 (blue circles) and θ_2 (orange triangles) directions (D). *Error bars represent standard deviation of the mean (n = 3 measurements of the same sensor).*

4.5.8 Skin Transmission Test

Since sensor placement in a UCL reconstruction application is at the humeral medial epicondyle, a sensor detection distance of 3 mm through superficial tissues (skin, subcutaneous tissue, etc.) is required [72]. Transmission distance of the sensor was evaluated by utilizing synthetic tissue mimics with dielectric properties of human skin (SynDaver) with a thickness of 3 mm. The impact on sensor signal transmission by varying the distance (Z) between the detection coil and electrophysiologically relevant skin tissue mimic measuring 3 mm thick superficial to the sensor was quantified (Figure 68A). Comparing the signal transmission of the sensor through air versus the skin mimic indicated the skin mimic caused a slight drop in resonance frequency (Figure 68B) and peak magnitude of the real reflection coefficient (Figure 68C). A reduction in signal magnitude with the introduction of a skin tissue mimic is likely due to absorption of the radiofrequency energy by the tissue mimic when compared to air. Change in resonance frequency when varying the distance (Z) between the detection coil and skin mimic superficial to the sensor, demonstrated resonance frequency readings were most consistent from 1 to 2 mm and 4 to 7 mm of displacement (Figure 68D). From 2 to 12 mm of displacement the signal magnitude decreased in a logarithmic manner ($R^2 = 0.99$) (Figure 68E).

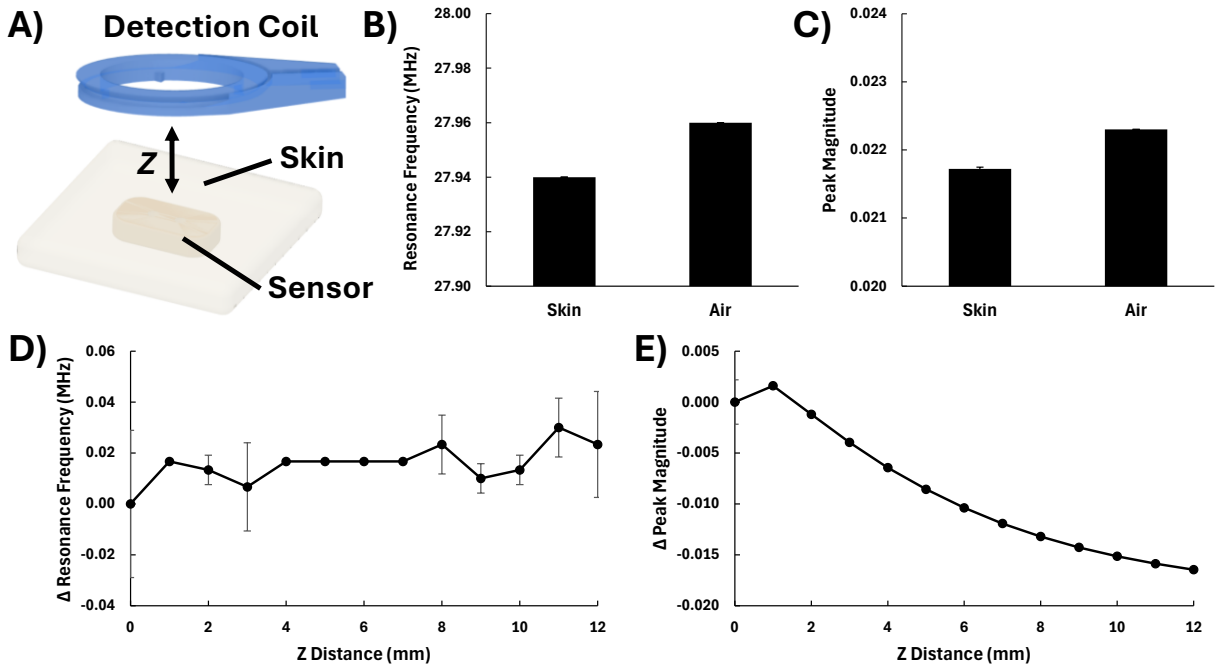

Figure 68. Schematic showing how distance (Z) varied between the detection coil and skin mimic superficial to the sensor (A). Comparison of measured sensor resonance frequency (B) and peak magnitude at resonance (C) through 3 mm of skin mimic and air. Change in resonance frequency (D) and peak magnitude at resonance (E) with increasing Z distance. *Error bars represent standard deviation of the mean (n = 3 measurements of the same sensor).*

4.6 Limitations & Conclusions

The largest limitation to detection device testing was the restricted detection device resolution (±0.01 MHz) as the resolution of the detection device measurements determines force resolution for sensitivity transfer functions based on the LC sensor. Furthermore, preliminary EMC/EMI characterization identified emissions near 900 MHz that exceeded targeted thresholds for the prototype detection device. These findings highlight that the present system should be considered an early-stage research platform rather than a clinically compliant medical device. Additionally, spatial and orientation resonance spectra detection limitations were determined with

respect to three different displacement directions and rotation orientations between the detection coil and sensor. Synthetic skin with physiologically relevant electrical properties was shown to slightly reduce sensor baseline resonance signals and future studies should evaluate if sensor force transduction transfer functions are also impacted by tissues superficial to the implanted sensor. In conclusion, this chapter gave initial characterization on some sources of resonance spectra measurement error when sensors were coupled with varying antenna designs from the engineered wireless detection device. Specifically, antenna design was optimized for signal transmission strength and coupling area while orientation and alignment limits were determined. However, future coupling characterization studies employing sensor encapsulation should be completed to optimize sensor design for signal transmission through tissues. Furthermore, antenna coupling and transmission experiments were conducted to guide engineering optimization of the detection system. Additional studies with larger sample populations and anatomically variable conditions will be necessary to characterize robustness across clinically relevant use case environments.

Chapter 5: Detecting Graft Loading in Ligament Reconstruction

Content of this chapter are adapted from:

Meyers K, Ong K (2026) “A Wireless, Passive Sensor to Monitor Intra- and Post-Operative Graft Loading in Reconstructed Medial Ulnar Collateral Ligaments.” In-preparation.

Author contributions

Conceptualization: KM, KO

Data Collection and Analysis: KM

Interpretation: KM, KO

Writing and Editing: KM, KO

5.1 Introduction

When the suture accessory sensor is deployed in a UCLR, the graft, suture, and sensor are placed in series. Therefore, the viscoelastic behavior of the graft tissue, suture, and suture accessory sensor all impact time-dependent loading mechanics. Various viscoelastic models that describe the time-dependent response to loading have been developed. One common model includes the standard linear viscoelastic model. The Zener representation of the standard linear viscoelastic model utilizes a spring (elastic element) in series with a dashpot (viscous element) and spring in parallel to model of viscoelastic materials (Figure 69).

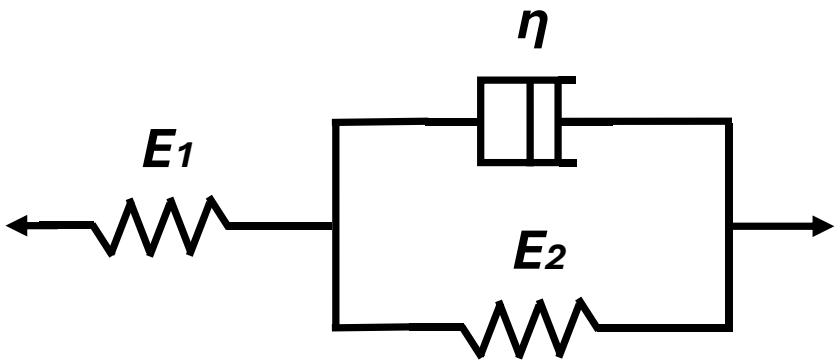

Figure 69. Standard linear viscoelastic model where E_1 is Young's modulus of the series spring, E_2 is the Young's modulus of the spring in parallel, and η is the viscosity of the dashpot in parallel.

The standard linear viscoelastic model is configured to describe the time-dependent phenomena of stress relaxation and creep. Stress relaxation occurs when stress in a material decreases when kept at a constant strain (Figure 70A). Creep describes the time-dependent change in strain of a material under constant stress (Figure 70B). Sensor loading studies generated signal calibration curves accounting for the primarily elastic behavior of the suture and sensor elements. However, graft material for UCLR is typically composed of highly viscoelastic tendon tissue.

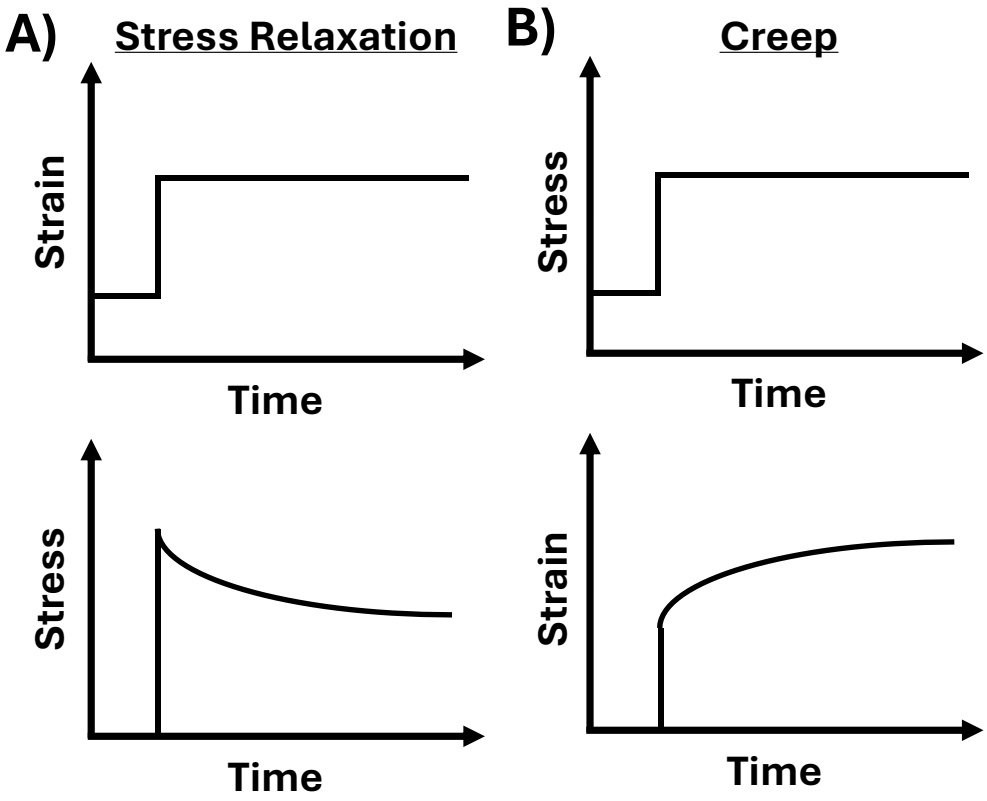

Figure 70. Relationship between force and strain during stress relaxation (A) and creep (B).

A typical stress-strain curve for tendons and ligaments can be divided into three regions: toe, linear, and failure (Figure 71A). The toe region represents elongation of crimped collogen of tendon and ligament tissue with initial loading. In the linear region describes how the tissue deforms before yielding where the slope of the graph represents elastic modulus. Tendon tissues utilized in UCLR grafts have elastic moduli ranging between 101 MPa (gracilis tendon) and 185 MPa (palmaris longus tendon) [73]. The failure region of the stress-strain curve consists of yielding to failure where tendon fibers are damaged. Ultimate failure torque in the UCL is reported between 22.7 to 36.9 N-m under valgus stress and UCLR failure modes include graft rupture [74].

Tendon tissue loading response is also rate-dependent where modulus increases with increased loading rates (Figure 71B). Due to the repetitive physiological loading requirements of tendon tissue, the impact of time-dependent viscoelastic properties on cyclic loading behavior of tendon tissue is fundamental in tendon biomechanics. During cyclic loading and unloading, tendon tissue displays hysteresis where the loading and unloading curves do not coincide (Figure 71C). Specifically, the hysteresis area between the loading and unloading portions of the stress-strain curve represents energy loss. With increasing cycles of loading tendon tissue exhibits decreased stiffness and increased strain at given stress. Generally, tendons have a shorter toe region and higher modulus compared to ligaments while ligaments can withstand higher levels of strain before failure (Figure 72). Despite the biomechanical differences between tendons and ligaments, tendons (e.g., palmaris longus or gracilis tendon) are utilized to replace the UCL in UCLR. Therefore, an *ex vivo* cadaver model utilizing tendon grafts for UCLR was employed to study the ability of the suture accessory sensor to detect loading after ligament reconstruction. Overall, this chapter focuses on determining if sensor loading measurements can be preliminarily characterized under biomechanical conditions in an *ex vivo* model.

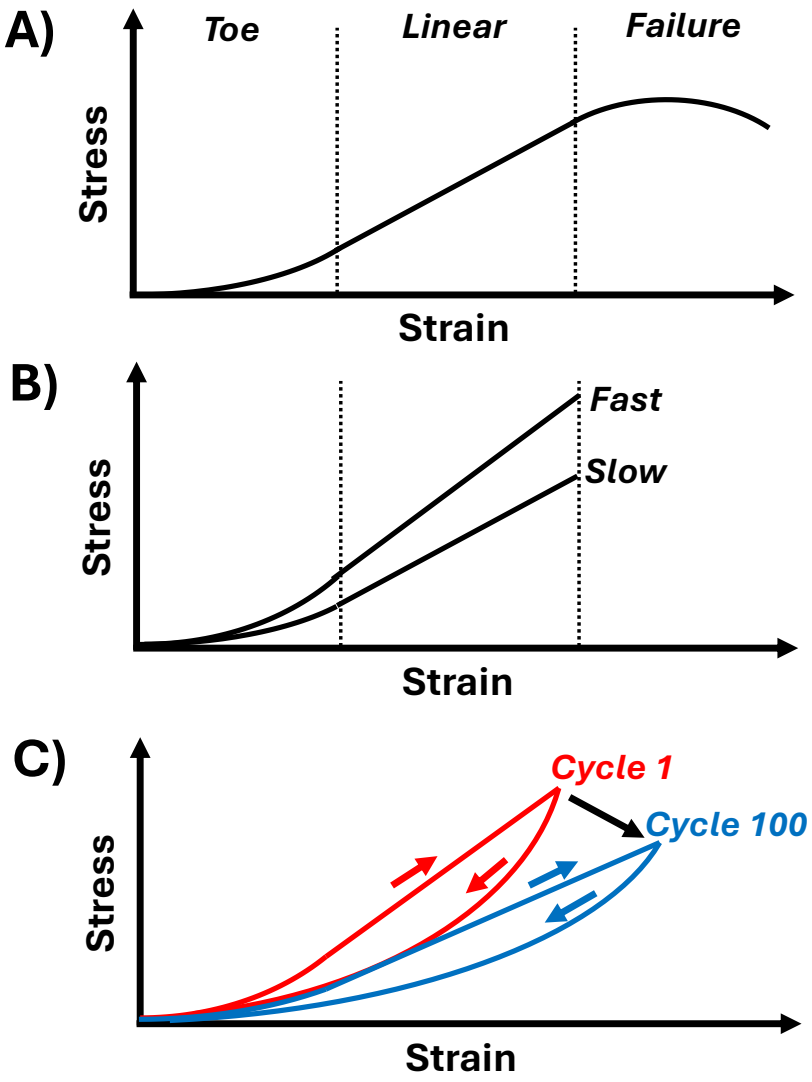

Figure 71. Stress-strain curve of tissue showing a toe, linear, and failure region (A). Stress-strain curve showing fast versus slow strain-rate stiffening behavior (B). Stress-strain curve showing loading and unloading behavior after 1 versus 100 cycles of loading (C).

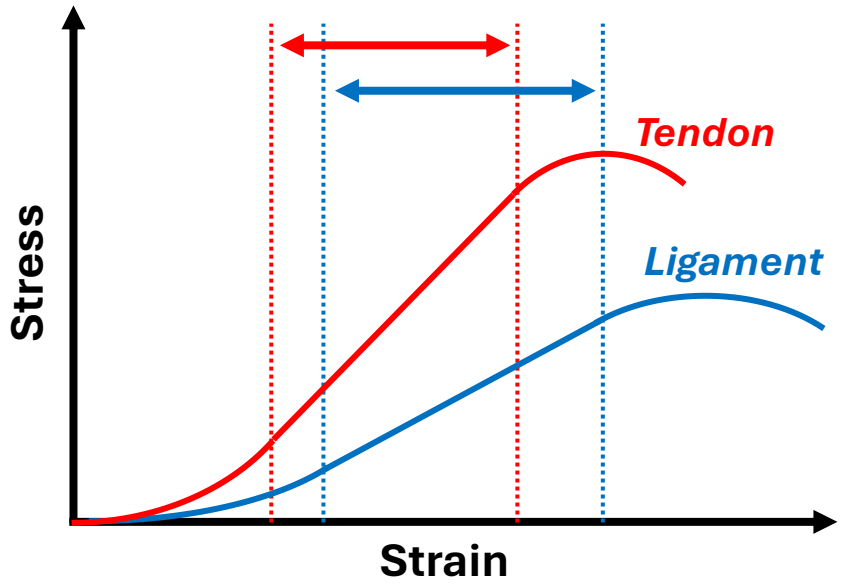

Figure 72. Stress-strain curve comparison of tendon versus ligament. Vertical dashed lines split respective toe, linear, and failure regions.

5.2 *Ex Vivo* Cervid Cadaver Model

5.2.1 Model Rationale

Human cadaver models are gold standard for evaluating UCLR techniques and approaches. However, some animal models for elbow injuries and pathologies have been developed utilizing rats, mice, rabbits, felines, and canines [75]. Literature on large animal models for human elbow reconstruction is limited, possibly due to the inclusion of quadrupedal mammals in most large animal studies and the complexity of human elbow anatomy [75]. For example, many animals can flex/extend the elbow joint but cannot pronate/supinate. Further, a large animal model was desired to match the relative size of the suture button to human anatomy. Non-human primates are an ideal animal model for elbow anatomy during UCLR, but availability of cadavers is restricted. To address limited availability of human tissues for experimentation, animal models for *ex vivo*

studies can be utilized. Human anterior ulnar collateral ligament stiffness has been reported between approximately 20 and 40 N/mm, but no animal models have been shown to mimic all major mechanical properties (e.g., Young modulus, ultimate tensile stress, and ultimate tensile strain) of human ligament tissue [76, 77]. Cervid limbs for *ex vivo* animal models are widely available and cervid joints have been previously shown to be candidates for human ligament models [78]. Therefore, to mimic a proximal single-tunnel suspensory fixation technique for UCLR with the suture sensor in a large animal, an *ex vivo* cervid model was utilized. Since cervids are quadrupedal, front limbs are designed for running and bounding with no supination. The cervid elbow joint has a small humeral medial epicondyle and extended olecranon process compared to humans (Figure 73A-B). Cervid front limb anatomy contains a relatively short humerus and long metacarpal compared to humans (Figure 73C-D). Therefore, a cervid carpal joint was utilized to mimic UCLR with the suture sensor, bridging the radius and metacarpal instead of the humerus and ulna in an elbow joint.

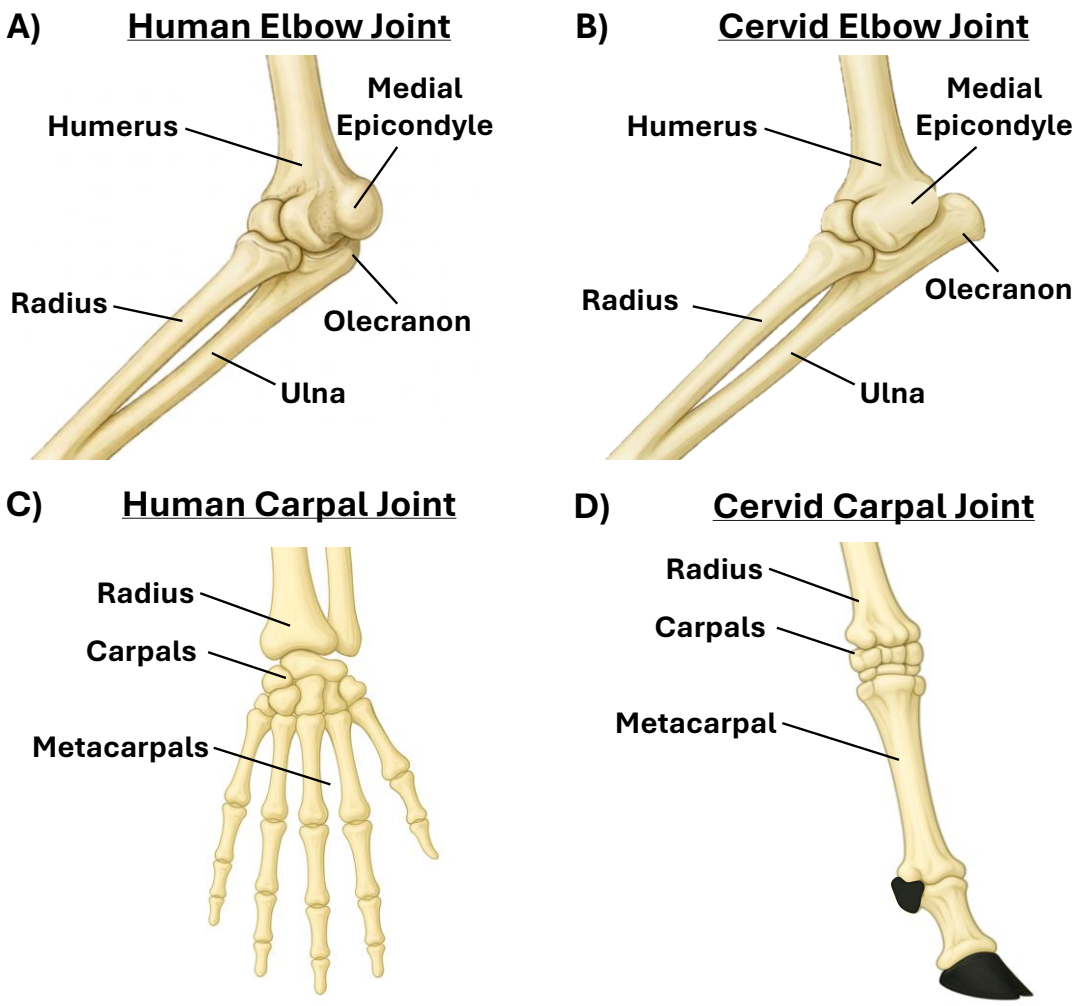

Figure 73. Comparison of human (A) and cervid (B) elbow joint skeletons. (Image partially generated with the assistance of Microsoft Copilot and Google Gemini Flash 3.0)

5.2.2 Model Methods

A cervid carpal joint was obtained to mimic a proximal single-tunnel suspensory fixation technique for UCLR while integrating the suture accessory sensor. The primary purpose of the *ex vivo* cervid model was to evaluate sensor deployment feasibility and wireless functionality within a reconstructed ligament environment rather than to reproduce the complete biomechanics of the human elbow. First the skin above the medial side of the joint was exposed via shaving and an

incision was made to show the intact joint (Figure 74A). A posterior tendon was identified and harvested for graft preparation (Figure 74B). The medial ligament was identified and excised (Figure 74C). A drill bit (5.5 mm in diameter) was utilized to create converging bone tunnels on the distal side of the joint (Figure 74D). On the proximal side of the joint, a single bone tunnel was generated with a drill bit (4.5 mm in diameter). Polyester braided sutures (Ti-Cron) of United States Pharmacopeia size #2 were stitched through the proximal end of the graft, passed through the proximal bone tunnel, and secured in a knot over the sensor (Figure 74E). Superficial tissues were closed and a detection coil was placed above the implanted sensor for subsequent load readings (Figure 74F). Sensor recordings were taken when the cervid joint was subject to valgus stress and bent from full flexion to full extension. Sensor response during failure of the suture knot was also characterized. In addition to an imperfect representation of complex human elbow anatomy, the *ex vivo* cadaver model could not replicate post-operative osteointegration of the graft expected in an *in vivo* environment.

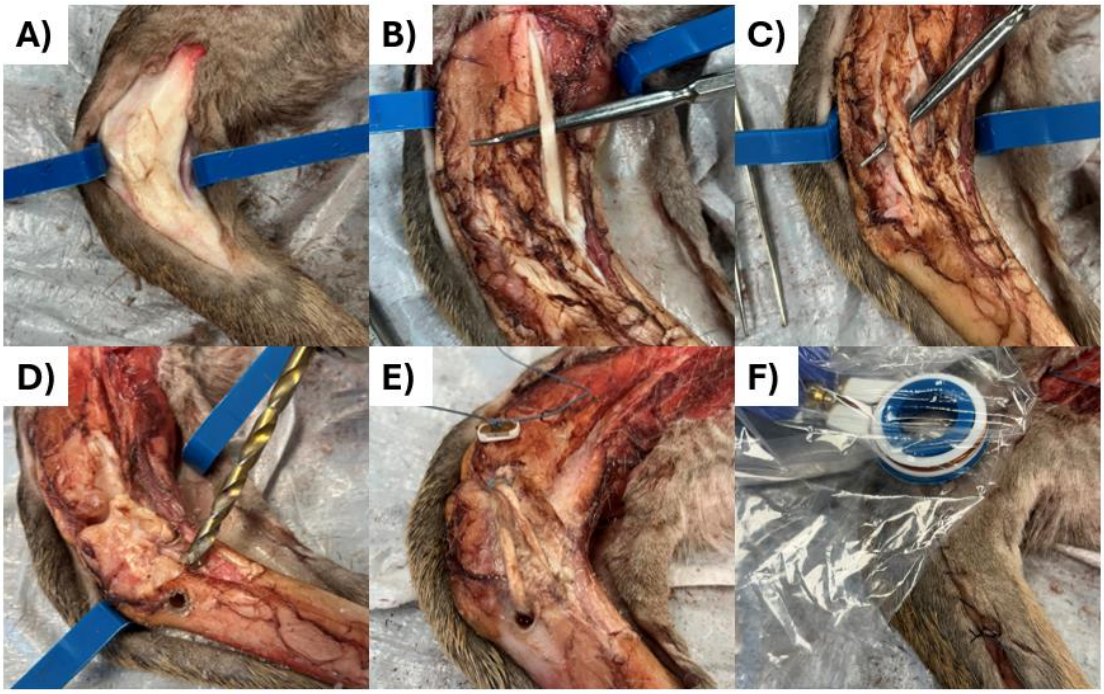

Figure 74. Incision at the joint (A). Isolation of the graft tendon (B). The medial ligament to be excised (C). Distal bone tunnel drilling (D). Sutured graft construct sutured with accessory sensor (E). Detection coil placed over implanted sensor (F).

5.3 *Ex Vivo* Cervid Cadaver Model Results

5.3.1 Baseline Frequency Change

When recording sensor signals, a decrease in baseline resonance frequency was observed with cervid skin placement over the sensor (~26 MHz implanted versus ~28 MHz in air). Since the sensor was not encapsulated, a change in baseline resonance frequency is likely attributed to a combination of cervid skin permittivity and the humidity/moisture at the implant site. For example, moisture increases the parasitic capacitance of the sensor circuit, leading to a decrease in resonance frequency according to Equation 5. Further, all *ex vivo* experiments were performed at room temperature and heating the sensor to body temperature would reduce resonance frequency

according to previous thermal characterization experiments. Additional combinations of temperature and humidity testing would be needed to fully characterize sensor signal susceptibility to environmental conditions. A decrease in signal magnitude from the sensor was noted when cervid skin was placed over the sensor (~0.0012 implanted versus ~0.0026 in air) likely due to radiofrequency energy absorption by the surrounding tissues.

5.3.2 Valgus Stress

The human UCL resists valgus and rotational stresses to support elbow joint stability (A). Valgus stress tests are performed by physicians to assess the integrity of the UCL by flexing the elbow, stabilizing the distal part of the humerus, and applying a valgus stress to the elbow joint. Joint laxity is compared to the contralateral elbow.

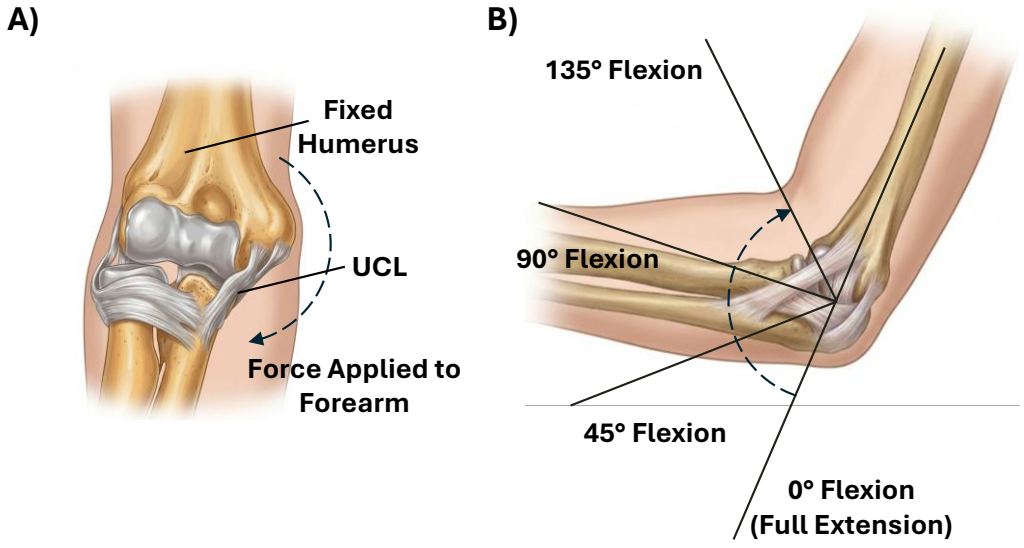

Figure 75. Human elbow valgus stress test (A) and flexion (B) schematics. (Image partially generated with the assistance of Google Gemini Flash 3.0)

To evaluate sensor load detection function, valgus stress was applied to the reconstructed cadaver graft with the joint at approximately 70 degrees of flexion while signal recordings were

taken with accessory sensor. As expected from previous loading characterization studies, resonance frequency increased with valgus stress application (Figure 76A). An increased measured resonance frequency from the implanted sensor demonstrated the ability of the sensing platform to detect graft construct loading. Fluctuation in sensor signal peak magnitude at resonance was also observed during initial valgus stress application but returned to baseline (Figure 76B).

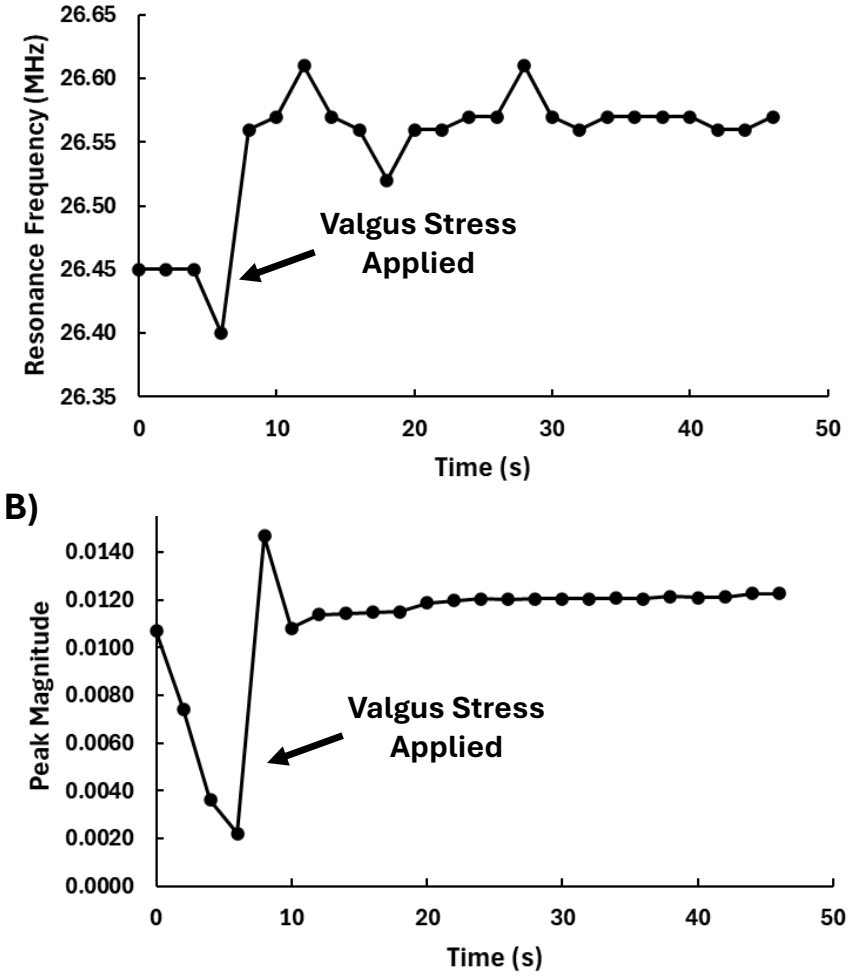

Figure 76. Sensor signal and resonance frequency (A) and magnitude (B) change during joint valgus stress application *(n = 1)*.

5.3.3 Flexion & Extension

The full range of motion of a human elbow joint ranges from 0 to 145 or 150 degrees of flexion (Figure 75B). Since the UCL resists elbow extension, UCL loading is higher during extension compared to flexion when an elbow is swept through full joint range of motion. When flexion from full extension to full flexion (approximately 150 degrees) was applied to the cervid joint, sensor resonance frequency was reduced (Figure 77A). A reduction in implanted sensor resonance frequency signal during joint flexion further indicated the sensing platform could detect graft construct loading. A slight fluctuation in measure sensor peak magnitude was observed during joint flexion but returned to a baseline at full flexion (Figure 77B).

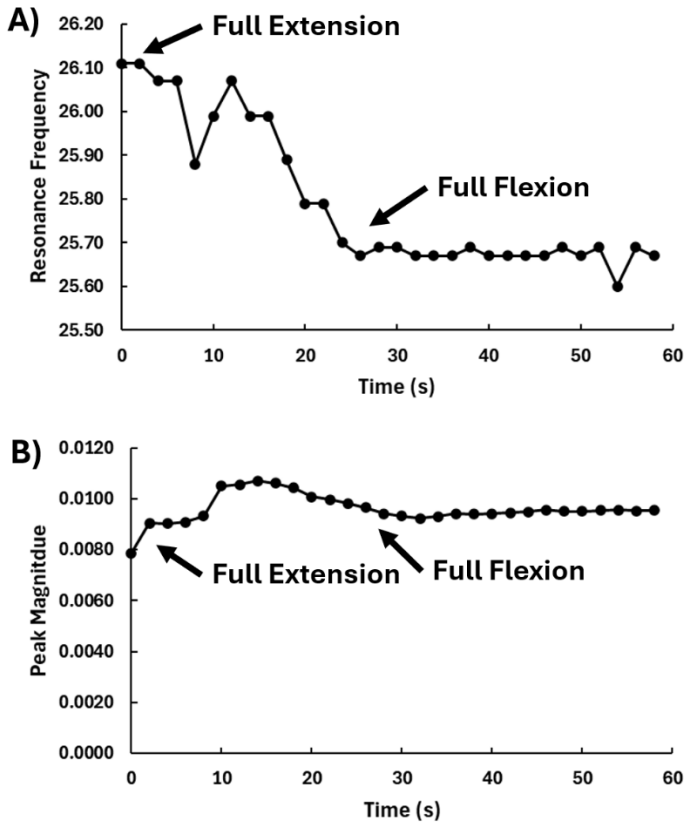

Figure 77. Sensor signal magnitude (A) and resonance frequency (B) change during joint flexion *(n = 1).*

Conversely, during joint extension sensor resonance frequency increased with initial extension and graft loading (Figure 78A). After 30 seconds, a noticeable negative drift in sensor resonance frequency was observed possibly due to relaxation in the suture-graft construct when held at a constant strain. Similarly, sensor signal magnitude at resonance also drifted negatively after full extension was applied (B).

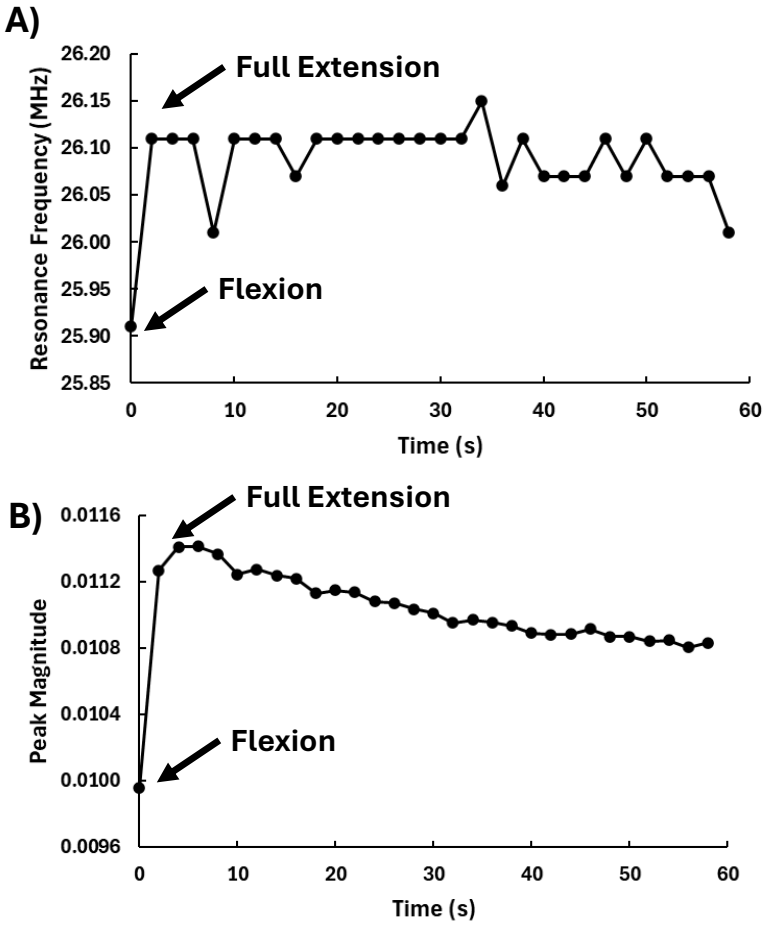

Figure 78. Sensor resonance frequency (A) and signal magnitude at resonance (B) change during joint extension *(n = 1)*.

Cyclic loading from full cervid joint flexion to full extension and back to full flexion indicated measured sensor resonance frequency responded to changes in graft construct loading in

both the loading and unloading directions (Figure 79). Notably, sensor resonance frequency signal appeared to return to flexion level baseline after the joint extension cycle was applied.

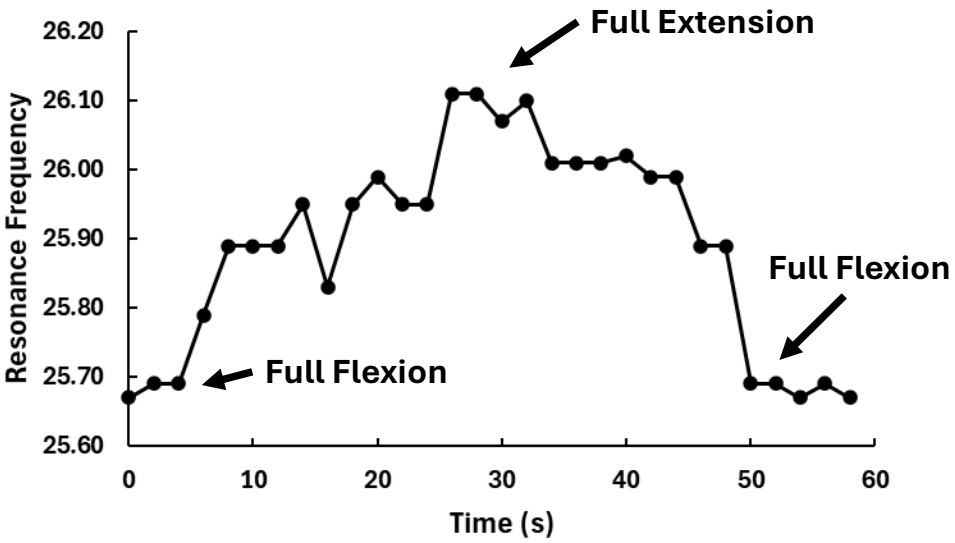

Figure 79. Sensor resonance frequency response when bending joint from maximum flexion to extension and back to maximum flexion *(n = 1).*

5.3.4 Failure Detection

Failure modes of the suture graft construct include the rupture of the graft, breakage of the suture, suture-graft interface failure, bone tunnel bridge failure, and suture knot slippage/loosening for example. Generally, suture failure is the most commonly reported failure mode of UCLR [75]. In the *ex vivo* cervid model, knot slippage occurred and was detected with the suture accessory sensor when the sensor stopped responding to load stimulus (Figure 80). Specifically, when applying valgus stress during knot slippage, resonance frequency signal quickly dropped after initial loading and subsequently resonance frequency signal did not increase with loading (Figure 81).

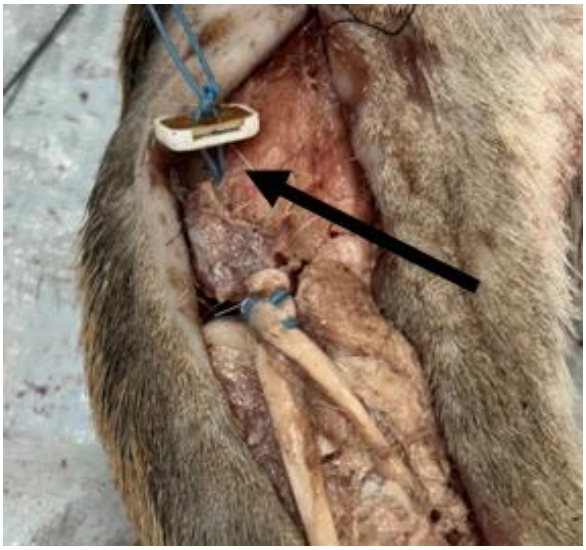

Figure 80. Loosened suture in sensor deployed in ligament reconstruction.

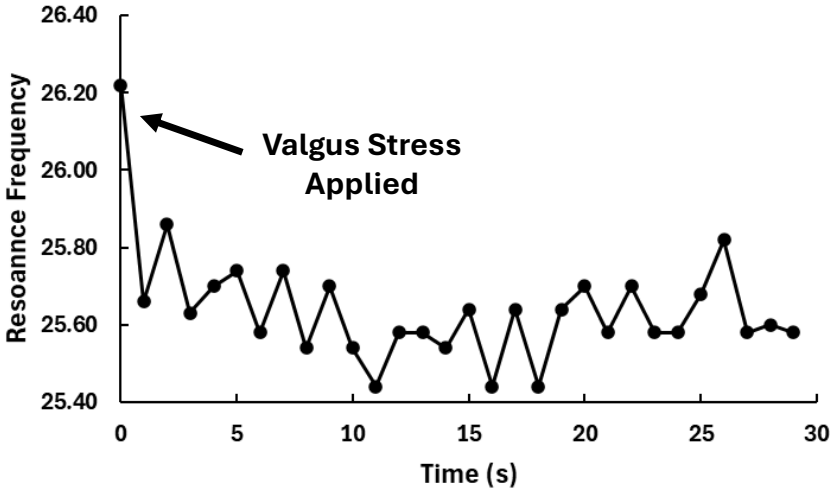

Figure 81. Sensor resonance frequency measurements during application of valgus stress with knot slippage failure of the graft construct *(n = 1)*.

5.3.5 Static Loading

To characterize sensor signal changes due to the viscoelastic graft construct, static loading of the sutured graft construct was performed outside the cervid cadaver joint by utilizing weights

(Figure 82). No cervid skin was placed above the sensor and as a result, baseline frequency was approximately 28 MHz. Static loads of 0 and 40 N were applied to the suture graft indicated increased measured resonance frequency with static loading (Figure 83).

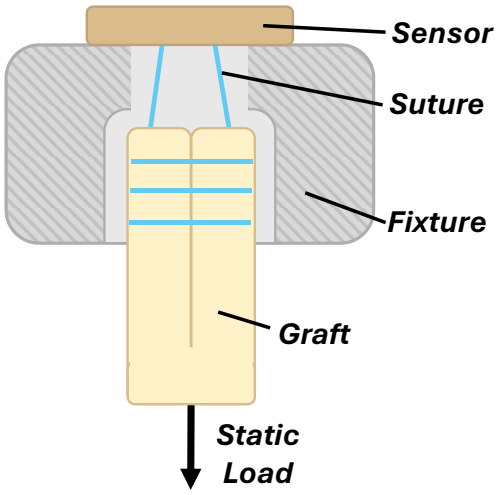

Figure 82. Schematic of graft construct static loading set-up.

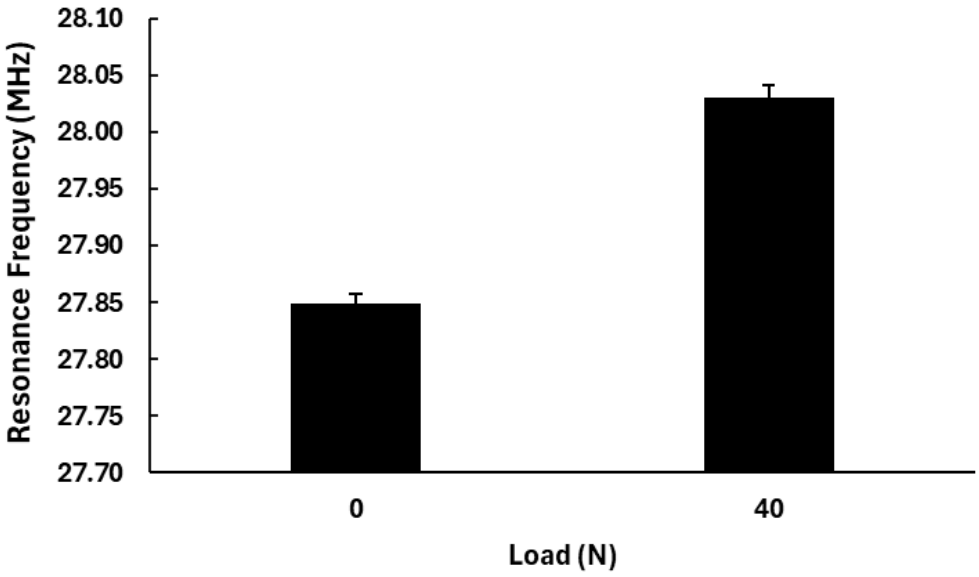

Figure 83. Sensor resonance frequency at graft static loads of 0 and 40 N. *Error bars represent standard deviation of the mean (n = 3 measurements of the same sensor).*

5.4 Limitations & Conclusions

A limitation of the cervid *ex vivo* model for evaluating sensor deployment and functionality was that cervid limb joint anatomy did not match that of humans. Further the mechanical properties (e.g., Young modulus, ultimate tensile stress, and ultimate tensile strain) of cervid and human ligaments and graft tendons are likely not exactly similar. Besides anatomical limitations, the *ex vivo* cervid model only utilized one sensor and one joint for testing, restricting conclusions that can be drawn from the data in the absence of replication. Also, since the baseline resonance frequency of the sensor was altered when implanted beneath superficial cervid tissues, it was not possible to directly correlate loading calibration curves generated in air (i.e., without overlaying tissues) with load-dependent frequency changes in the *ex vivo* model. Therefore, *in situ* calibration of the sensing platform needs to be completed as demonstrated in implantable LC sensors already implemented in the clinic [50, 79].

The present dissertation focused primarily on engineering validation of the sensing platform rather than clinical validation of graft biomechanics. This chapter provides feasibility if sensor loading measurements could be implemented under biomechanical conditions in an ex vivo model. Specifically, sensor resonance frequency changed in response to tension loading during joint valgus stress and varying degrees of joint flexion and extension. However, future *ex* vivo studies employing *in situ* calibration with force gauges should be performed to generate transfer functions relating changes in resonance frequency with alterations in tension. This experiment was also limited by small specimen numbers and should therefore be interpreted as feasibility demonstrations of wireless sensing functionality rather than comprehensive biomechanical validation studies. Future investigations involving larger cadaveric sample sizes and human tissue models will be required to evaluate statistical reproducibility and clinical relevance.

Chapter 6: Conclusions

Content of this chapter are adapted from:

Meyers K, Ong K (2026) "A Wireless, Passive Sensor to Monitor Intra- and Post-Operative Graft Loading in Reconstructed Medial Ulnar Collateral Ligaments." In-preparation.

6.1 Primary Conclusions & Contributions to the Field

In conclusion, the thesis work established the basic functionality of a suture accessory sensor that could measure tension in UCLR grafts to help surgeons determine correct tension during operation and physical therapists with guiding post-operative rehabilitation. Additionally, the sensing technology could inform healthcare professionals of reinjury due to suture breakage or graft failure complications. Important questions on how tight grafts should be tensioned, how well graft tension is maintained after surgery, and how variations in surgical technique influence graft loading behavior could be elucidated by the sensing platform. Quantifying the biomechanical forces on UCL grafts during rehabilitation could also aid in improving UCLR physical therapy practices and guidelines. For example, biofeedback on UCL graft tension could also help facilitate evidence-based, personalized care for baseball pitchers when determining return to throwing and assist in calculating throwing load during rehabilitation to prevent overuse during the recovery period. The sensor could also potentially assist athletes in determining when it is appropriate to return to play since it is expected that suture load will decrease as tissue healing progresses. Overall, the graft loading information provided by the suture accessory sensor may help improve ULCR surgery and rehabilitation with the rise in UCLR procedures in adolescent and professional baseball pitchers.

The engineering objective of this work was to develop a wireless and battery-free implantable sensor in the form of an inductor-capacitor (LC) suture accessory to detect graft loading magnitude in ulnar collateral ligament reconstruction (UCLR). A central question guiding the objective consisted of determining if a passive, implantable LC-based suture sensor could provide quantitative and reliable measurements of graft loading under clinically relevant biomechanical conditions specific to UCLR. The overall hypothesis was that tensile loading applied to a ligament graft construct can produce measurable and repeatable changes in the resonance behavior of an integrated passive LC-based suture accessory sensor, enabling wireless detection of relative changes in graft loading under biomechanically relevant UCLR conditions. To test this hypothesis, Aim 1 demonstrated that planar inductor-based LC sensors could be utilized to transduce loading across UCLR-relevant loading ranges from 10 to 50 N with calibrated transfer functions in controlled settings. However, during off-axis loading of the sensor and varying sensor environmental conditions (i.e., temperature changes) these transfer functions may be undesirably altered. Aim 2 indicated detection device resolution is limited to $\pm$ 0.01 MHz, constraining the sensing platform load resolution. Furthermore, the sources of error in measured resonance frequency with varying displacement direction and rotation orientation coupling conditions could be constrained via antenna optimization, but further evaluation of the impact of superficial tissues on sensor signals is needed to optimize future sensor encapsulation approaches. Finally, Aim 3 combined the engineered sensor and detection device from previous aims to demonstrate that the measured resonance frequency of an implanted sensor responded to joint loading when deployed within an *ex vivo* ligament reconstruction model. However, further *in situ* force calibration with sensors deployed in a ligament reconstruction is needed since baseline resonance frequency was altered when implanted with superficial tissues versus in air.

6.2 Limitations

Since the current frequency resolution limitation of detection device is 0.01 MHz (~5% FSO of the sensor), improving the resolution of the detection device could be utilized to better resolve changes in sensor resonance and therefore UCLR graft tension. If increased sensitivity is desired by clinicians, sensor aspect ratio could also be increased while suture hole placement distance could be reduced. However, testing indicated that sensor thickness should not be reduced for UCLR loading ranges for device mechanical integrity purposes. Although a detection distance of 3 mm through superficial tissues is sufficient for UCLR, if deeper suture accessory applications (e.g., rotator cuff, ankle syndesmosis, etc.) are required, the power output of the detection device could be increased. For example, the detection device power output was only 0.1 mW during testing but may be safely increased to 1 mW to match clinically available radiofrequency detection devices [79, 80]. The size of the sensor circuit design and trace thickness may also be increased to improve signal transmission through tissues for applications that allow suture accessories with a larger physical footprint. Due to some drift in the baseline frequency of the sensor with 10^4 loading cycles, further repetitive loading studies are required to characterize fatigue in the sensor material with a lower number of loading cycles and determine if the level of drift is acceptable for loading cycle quantity in UCLR applications.

One fundamental weakness in the sensor design is that it is contradictory to make the plastic sensor design resistant to overloading as a thicker sheet leads to higher force loading ranges but decreased sensitivity. If the sensor is not engineered to withstand overloading, failure of the sensor occurs via permanent deformation of the structure. Another anticipated problem with the sensing platform includes the impact of sensor bending deformation on UCLR graft displacement and ulnohumeral gapping. Typical human ulnohumeral gaps measure from 4 to 8 mm which is essential

for on graft-bone tunnel integration and elbow joint biomechanics [74]. Therefore, the sensing platform needs to be rigorously evaluated with human cadaver models to ensure ulnohumeral gaps remain in adequate ranges. The indirect relationship between sensor size and signal transmission distance is also a major weakness in the sensing platform since the smaller size demands make it increasingly difficult to detect the implanted sensor through tissue at greater depths. However, inductor stacking withing the sensors developed in the thesis work present a method to combat size-dependent transmission capability. Since planar inductor LC sensors are sensitive to various environmental parameters, more in-depth temperature and humidity characterization is required covering physiologically relevant implant conditions. Finally, the sensor can determine graft loading forces only for as long as interface between the graft and bone tunnel is not healed, whereafter the sensor is instead measuring healing progression of the interface.

6.3 Future Directions

Future work includes determining failure loads and modes to identify the mechanical limitations of the implantable sensor. Finding appropriate bioinert encapsulation materials to shield the implanted sensor circuit from biological environment while still maintaining sensitivity of the device is also required before performing *in vivo* biocompatibility and functionality testing of the sensing platform. It is critical that encapsulation materials prevent water leakage as the permittivity of water can impact sensor baseline signals, although water vapor diffusion into encapsulation materials in not preventable. However, fabrication techniques employing humid conditions during sensor encapsulation could help reduce sensor drift due to water vapor diffusion. Accelerated lifetime testing may also be helpful in determining sensor function performance over time prior to *in vivo* experimentation. Since the sensor utilizes changes in deformation to transduce loading force, examining how the viscoelastic behavior of suture material and ULCR grafts influence

sensor tension detection will also reveal how well the sensor performs during loading versus unloading conditions. Evaluating the impact of varying suture knotting techniques during UCLR on the performance of the sensor platform would be useful in addressing any effects of knot slippage. Although coupling characterization between the detection coil and sensor were performed with altering relative displacement, orientation, and rotation to determine the impact on baseline senor signals, any impact of alignment on sensor sensitivity should also be characterized. Further, an algorithmic approach to positioning the detection coil superficial to an implanted sensor should be developed to assist end users with optimizing detection coil alignment for subsequent sensor readings. Within the area of UCL repair, the use of suture bracing for partial UCL tears is rising, therefore integrating the wireless, passive sensor technology into suture anchors used in securing braces may also help address other forms of UCL injuries that require surgical intervention [58, 81].

Appendix 1: Tracheostomy Tube Monitoring Accessory to Detect Accidental Decannulation and Obstruction Emergencies in Ventilator-Independent Pediatric Patients

Content of this chapter are adapted from:

Meyers K, Burke Q, Siddiqui A, Zalzal H, Osmond T, Ong K, Sherman J (2024) "Tracheostomy Tube Monitoring Accessory to Detect Accidental Decannulation and Obstruction Emergencies in Ventilator-Independent Pediatric Patients." Tracheostomy 1(3):7-16.

Author contributions

Conceptualization: JS, KM, QB, KO, HZ

Data Collection and Analysis: QB, KM, AS

Interpretation: KM, KO, JS, QB, HZ, TO

Writing and Editing: KM, KO, JS, QB, HZ

Abstract

Introduction:

Some of the leading causes of tracheostomy-related complications in pediatric populations are accidental decannulation and obstruction events that result in permanent neurological damage or death if not mitigated quickly enough. Despite the severity of tracheostomy tube emergency events, there is currently no effective medical technology available that can specifically detect accidental decannulation or obstruction in a tracheostomized patient that is not ventilator

dependent. Therefore, a pediatric tracheal breathing model system was developed to assist with testing new tracheostomy tube technologies for identifying emergency events.

Methods:

A custom carbon dioxide monitoring tracheostomy tube attachment was engineered to collect breathing waveform data during emergency events (e.g., improper insertion, accidental decannulation, and mucus obstruction). Anatomically accurate pediatric tracheal models for various age groups (0-3 months, 2-4 years, and 10-12 years old) were developed with modelling software and a 3D printer. A breathing simulator was integrated with the tracheal models to generate age-dependent respiration patterns during simulated tracheostomy tube emergencies.

Results:

Carbon dioxide readings from the custom tracheostomy tube attachment indicated distinct waveform recordings during simulated tracheostomy tube emergency events for all age groups tested. During incorrect insertion, accidental decannulation, and complete blockage of a tracheostomy tube, exhaled carbon dioxide readings remained static at ambient levels. Partial mucus obstruction of a tracheostomy tube decreased exhaled carbon dioxide waveform amplitude relative to unobstructed conditions.

Conclusions:

The tracheostomy tube attachment successfully recorded respiration patterns during simulated tracheostomy tube emergencies in pediatric patients of varying age. Breathing waveform data collected from the model system will aid in the development of emergency airway event detection software integrated in the tracheostomy tube sensing accessory.

1. Introduction

Tracheostomy tubes are life-sustaining medical devices that maintain a secure airway for patients who require prolonged or permanent breathing support. In the United States, 4,800 pediatric tracheostomy procedures are performed annually, typically in children with a mean age of 3 years old [82-85]. Globally, 25,000 children require tracheostomies each year, and it is expected that these numbers will grow with improving healthcare quality and access in developing countries, as well as advancements in medical technologies that enable clinicians to keep younger premature babies alive [86]. To ensure the safety and quality of life for individuals needing tracheostomy interventions, tracheostomy tubes are employed in various settings including hospitals, homes, schools, and other community areas. As a result, caregivers of tracheostomized pediatric patients range from experienced medical professionals to family members. Despite well-established guidelines for tracheostomy tube care, 20% of tracheostomized pediatric patients experience an emergency complication with their tracheostomy tube that requires immediate caregiver notification and intervention [87, 88]. Furthermore, infants and children with tracheostomy tubes have difficulty vocalizing to alert caregivers of an emergency due to the presence of a tracheostomy tube, where air bypasses the vocal cords and thus prevents adequate vocalization. Qualitative interviews with caregivers of tracheostomized children also indicate that current training methods and frequency of training are insufficient [89, 90]. Specifically, nurses, assistant nurses, and emergency medical professionals report a lack of confidence in tracheostomy care skills as a result of low patient volumes, while family caregivers describe anxiety and panic surrounding emergency tracheostomy tube events at home due to insufficient training during patient discharge proceedings.

The leading causes of tracheostomy-related emergencies and fatalities in children are accidental decannulation and obstruction with many of these events occurring outside hospital settings where parents, family members, and at-home nurses serve as primary caregivers [83, 91]. Studies indicate a 4-6% mortality rate in tracheostomized pediatric patients due to accidental decannulation and obstruction complications [88, 92, 93]. Accidental decannulation transpires when a tracheostomy tube is partially or fully removed from the tracheal stoma. Decannulation can be caused by severe coughing, tracheostomy tube securing tie failure, and pediatric patients pulling on and dislodging tubes. The likelihood of accidental decannulation is increased when patients are not sedated in hospital settings or are highly mobile in at-home environments. For children, unintended decannulation is more common as toddlers improve their mobility and dexterity skills [94, 95]. Tracheostomy tube obstruction events are a result of mucus occlusions or false passages where the tracheostomy tube is accidentally inserted into the pre-tracheal space. Mucus obstruction complications arise when respiratory tract secretions fully or partially occlude the tracheostomy tube cannula, blocking airflow. When compared to adults, the frequency of mucus obstruction and plugging events is increased in pediatric patients due to smaller tracheostomy tube airway sizes and the absence of inner canula placement [96]. False passage, or unintended insertion of the tracheostomy tube into the pre-tracheal space, can happen when a tracheostomy tube needs to be changed during weekly routine or emergency replacements. Furthermore, false passage events are more likely in pediatric patients due to shorter neck anatomy [88, 97]. Irreversible injury and death are the most severe consequences of accidental decannulation and obstruction events. When a tracheostomy tube is removed via unintended decannulation or obstructed, cardiopulmonary distress and hypoxia begin immediately. If the

airway is not re-established within 3-5 minutes by a caregiver, catastrophic injury such as permanent neurological damage or death may likely occur.

Methods to identify tracheostomy complications in patients that require full-time artificial ventilation rely on built-in ventilator sensors to detect most breathing complications, but for individuals who can spontaneously breathe on their own through tracheostomy tubes there are no medical technologies available that can effectively sense a decannulation or obstruction event. Ventilator-independent use of tracheostomy tubes is especially relevant during tracheostomy weaning protocols for pediatric patients which require at least 3 months of no ventilation support [96]. To detect emergency tracheostomy tube complications in ventilator-independent patients, caregivers currently rely on visual inspection and pulse oximetry. Visual signs of accidental decannulation and mucus obstruction complications include abnormal chest movements, color change due to lack of oxygenation, and incorrect tracheostomy tube positioning. Furthermore, the tracheal space is not visible during tracheostomy tubes changes so caregivers of tracheostomized patients in at-home environments rely on subsequent indications of breathing to confirm correct tube placement [98]. Observation techniques are inefficient due to continuous supervision requirements and many visual indications of tracheostomy complications more difficult to identify in children. Pulse oximetry devices are not specific to tracheostomy tube complications and delay problem identification between 1-3 minutes when the effects of hypoxia may have already started. Infants and children also commonly pull or kick off pulse oximetry monitors, causing false alarms and alarm fatigue for caregivers. A tool that enables real-time and specific tracheostomy tube problem-identification would allow caregivers to spend less time troubleshooting and provide a greater opportunity for airway re-establishment in an emergency event, significantly reducing negative outcomes in pediatric patients [99].

Therefore, a custom carbon dioxide sensing system was engineered in the form of a compact, universal tracheostomy tube attachment to monitor for tracheostomy tube decannulation and obstruction emergencies. The sensitized attachment device was utilized to collect breathing waveform data during simulated tracheostomy tube emergency events (e.g., accidental decannulation, improper insertion, and mucus obstruction). To assist with testing new tracheostomy tube technologies for identifying emergency events in ventilator-independent patients, a pediatric tracheal breathing model system was developed to mimic tracheostomy tube respiration patterns. The airway model system consisted of 3D-printed tracheal models and a breathing simulator to create respiration patterns for various pediatric patient age groups (0-3 months, 2-4 years, and 10-12 years old). Results indicated that during incorrect insertion, accidental decannulation, and complete blockage of a tracheostomy tube, exhaled carbon dioxide readings remained at a static baseline while waveforms collected during partial mucus obstruction had decreased signal amplitude relative to unobstructed conditions. Overall, the tracheostomy tube breathing monitor developed in this work will enable caregivers to more quickly identify and specifically detect airway problems in ventilator-independent patients.

2. Methods

A. Custom Carbon Dioxide Monitoring Tracheostomy Tube Attachment

A prototype carbon dioxide sensing tracheostomy tube attachment was engineered with a medical-grade carbon dioxide sensor (USEQGSEAC82180; Kemet, Fort Lauderdale, FL), power management circuitry, a coin cell battery (CR1632), and Bluetooth Low Energy (BLE) microcontroller (Artemis; SparkFun, Boulder, CO). Printed circuit board design software (Eagle; Autodesk, San Fransico, CA) and manufacturing facilities (OSH Park, Lake Oswego, OR) were utilized to fabricate custom circuitry. Calibration of the carbon dioxide sensor was achieved

following manufacturers specifications. The microcontroller was programmed to output carbon dioxide sensor readings over a serial communication interface for data collection purposes. Electronics housing prototypes were made with an Original Prusa i3 MK3S+ 3D printer (Prusa Research, Prague, Czech Republic) and polylactic acid filament (eSUN, Shenzhen, China). The size of custom attachment was approximately 2.5 x 2 x 2.5 cm and the weight (including battery) was 8.7 g. To ensure compatibility with existing tracheostomy tubes and accessories, the carbon dioxide monitoring attachment was designed to fit between a standard tracheostomy tube hub (15 mm outer diameter) and a heat moisture exchanger (Figure 1).

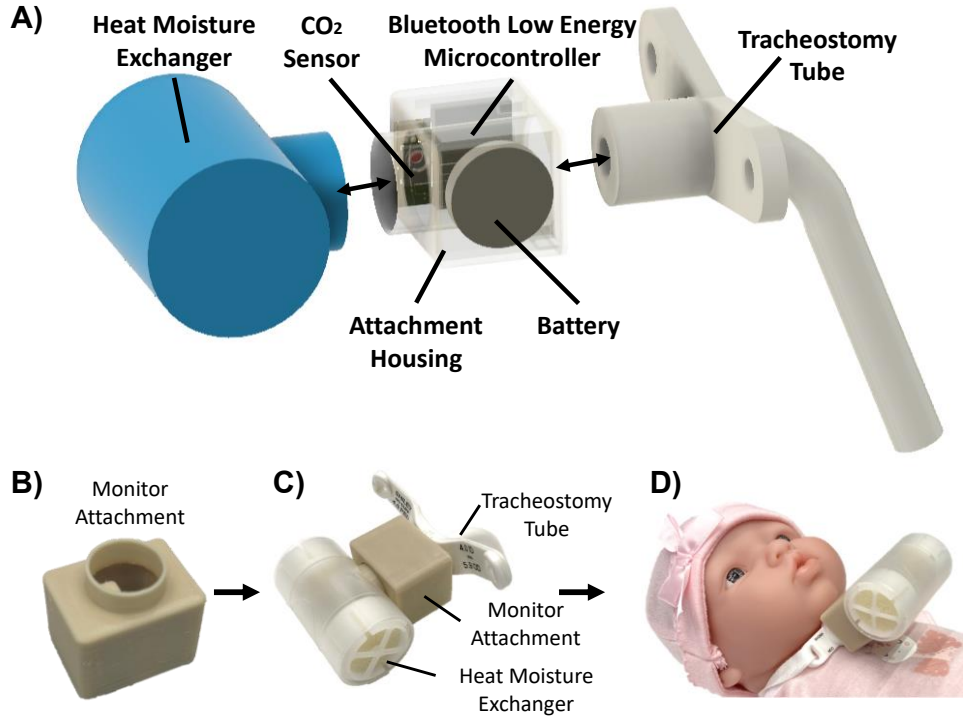

Figure 1. Exploded model of tracheostomy tube emergency complication detector attachment aligned between a heat moisture exchanger and tracheostomy tube (A). Assembled carbon dioxide monitoring attachment (B). The attachment can be coupled to a tracheostomy tube and heat moisture exchanger (C). Tracheotomized extremely premature infant-sized model (~24-week gestational age) with monitoring attachment and heat moisture exchanger (D).

B. Pediatric Tracheostomy Model Fabrication

Since pediatric tracheal anatomy and respiration patterns are age-dependent, models were generated for patients aged 0-3 months, 2-4 years, and 10-12 years. Pre-existing 3D digital files representing the upper torso/neck and trachea were utilized to achieve anatomically accurate tracheal models. All virtual prototyping was performed using a Dell Precision 7530 mobile workstation laptop with Onshape (PTC, Boston, MA) and Parasolid (Version 34.1; Siemens AG, Munich, Germany) software. For the 0-3 months, 2-4 years, and 10-12 years age groups, models were generated with an average trachea diameter of 5.25 mm, 7.67 mm, and 12 mm and average neck circumferences of 22.5 cm, 25 cm, and 31.5 cm, respectively (Figure 2) [100-102]. Tracheas were positioned approximately 3-5.5 mm deep from the outer surface of the anterior portion of the neck depending on the age group [103, 104]. The trachea was positioned vertically with the assumptions that the top of the larynx was in the same traverse plane as the C5 vertebrae and that the C5 vertebrae was in the same traverse plane where the superior portion of the trapezius muscle meets the neck [105].

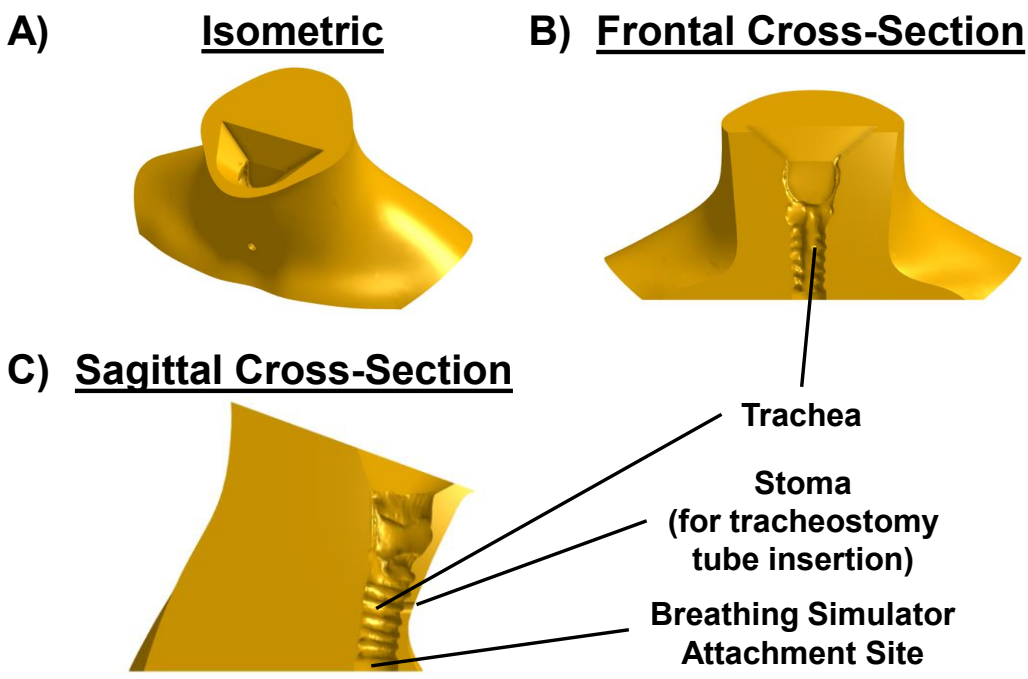

Figure 2. Digital rendering of pediatric tracheal model showing isometric (A), frontal cross-section (B), and sagittal cross-section (C) views.

The printable components of the tracheal models were fabricated with an Original Prusa i3 MK3S+ 3D printer and thermoplastic polyurethane (3D Printing Canada, Hamilton, Ontario). Details on printer settings are available (Appendix A). To replicate the tracheostomy tube/stomal interface, synthetic skin overlays were fabricated from rubber silicone (Smooth-On Dragon Skin™ 10 NV; Macungie, Pennsylvania) and a fabric mesh. The silicone skin was poured in a mold and left to cure for an excess of 18 hours. Tracheal models were assembled by overlaying the 3D-printed tracheal models with synthetic skin (Figure 3).

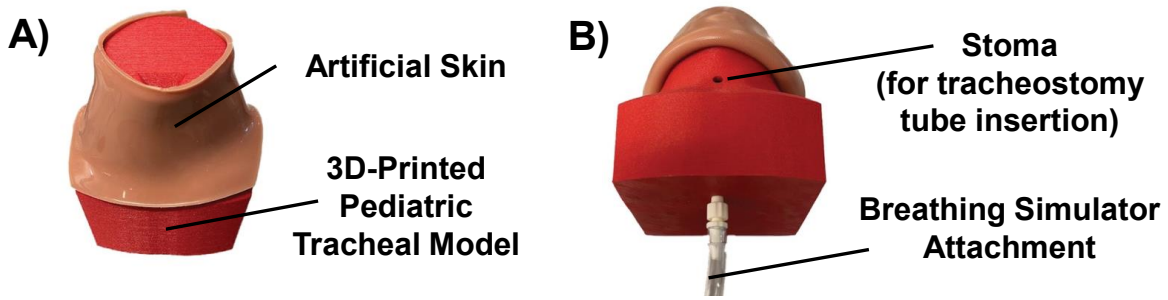

Figure 3. Pediatric tracheal model assembly (A) and airway integration features (B).

C. Breathing Circuit Set-Up for Simulations

To provide pressure-driven respiration function in the tracheal models, an ASL 5000 Breathing Simulator (IngMar Medical, Pittsburgh, PA) was integrated in the model system. Age-dependent breathing parameters (e.g., breathing rate, tidal volume, and resistance) were matched to the neonate, toddler, and pediatric tracheal models (Table 1).

Table 1. Age-dependent breathing model parameters.

Breathing Parameter by Age	**Neonate (0 to 3-month-old)**	**Toddler (2 to 4-year-old)**	**Pediatric (10 to 12-year-old)**
Tidal Volume (mL) [106, 107]	25	120	210
Uncompensated Residual Capacity (mL)	200	375	500
Resistance In and Out ($cmH_2O/L/s$)	40	25	20
Compliance (mL/cmH_2O)	8	15	30
Breathing Rate (breaths/min)	32	24	22
Inspiration Pressure Max (cmH_2O)	8	12	14

To produce exhaled carbon dioxide in the model system, an auxiliary gas exchange cylinder (balloon lung) was incorporated along with a gas supply tank. Carbon dioxide delivery was adjusted to match normal, healthy end-tidal carbon dioxide values (35 to 45 mmHg) [108]. A medical-grade capnograph (EMMA Capnograph; Masimo, Irvine, CA) was used to verify carbon dioxide output levels in the model system. Additionally, a TSI 3076 Aerosol Generator (TSI Incorporated, Shoreview, MN) was used to provide humidity in exhaled breaths of the model system. A humidity sensor (IncuTherm Plus; Incubator Warehouse, Fruitland, ID) was used to confirm moisture levels in the artificial airway. To account for added resistance of downstream

simulation components (balloon lung, tubing, etc.), the lung resistance on the ASL 5000 was lowered until tidal volumes matched expected values for each age group [106, 107]. Output from the breathing simulator, aerosol generator, and carbon dioxide supply was connected to tracheal models for emergency tracheostomy tube simulations (Figures 4-5A). An incision was made in the artificial skin of the pediatric tracheal models for subsequent tracheostomy tube insertion (Figure 5B). For the neonate model, a cuffless 2.5 mm inner diameter Bivona neonatal tracheostomy tube (#60SN025) (Smiths Medical, Minneapolis, MN) was used for the simulations. Cuffless Bivona tracheostomy tubes of 3.5 mm inner diameter (#60SP035) and 5.5 mm inner diameter (#60SP055) were implemented in the toddler and pediatric models respectively. Once the tracheostomy tube was in place, the custom carbon dioxide monitoring attachment was coupled to the tracheostomy tube hub (Figure 5C). Since ventilator-independent patients require passive airway humification, a heat moisture exchanger (Ballard 500 pediatric T; Avanos Medical, Knivsta, Sweden) was also added (Figure 5D).

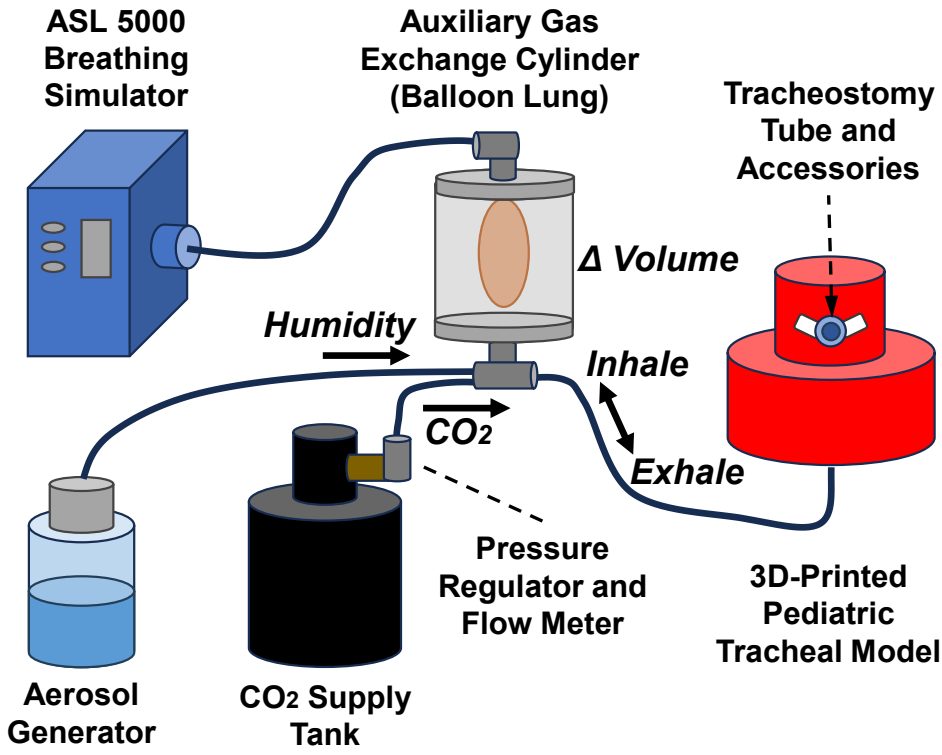

Figure 4. Diagram of pediatric tracheostomy simulation model showing breathing circuit connections.

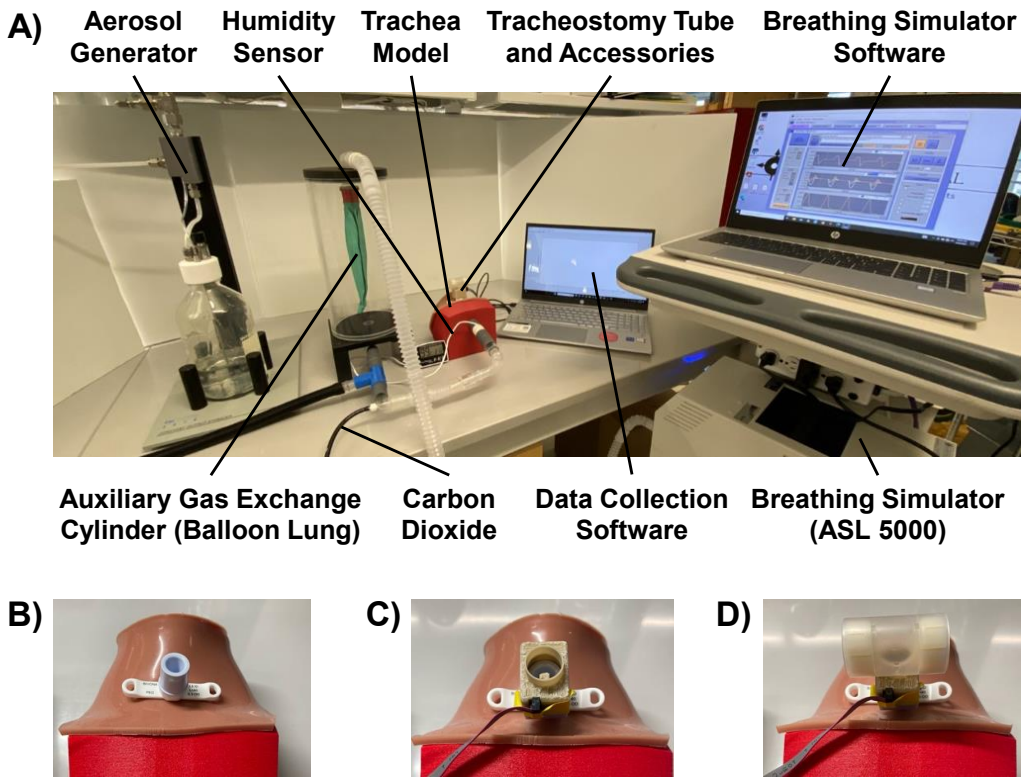

Figure 5. Pediatric breathing model system set-up for simulating tracheostomy tube emergency events (A). Tracheal model with the addition of a tracheostomy tube (B), carbon dioxide monitoring attachment (wired version) (C), and passive heat moisture exchanger (D).

D. Simulation of Tracheostomy Tube Emergency Events

Emergency tracheostomy tube events of incorrect insertion, accidental decannulation, and mucus obstruction were simulated with the pediatric breathing model system. Incorrect insertion of tracheostomy tube into the pre-tracheal space was emulated by placing the tracheostomy tube cannula between the synthetic skin and underlying 3D printed trachea model. Accidental decannulation of the tracheostomy tube was mimicked by fully removing the tracheostomy tube cannula from the trachea and stoma of the model. Partial and full blockages of tracheostomy tubes were simulated with an artificial mucus (Biochemazone, Leduc, Alberta, CA). Blockage was achieved by gradually adding artificial mucus (0.05 mL increments) directly into the tracheostomy

tube. For the 2-4 year-old model, partial blockage was achieved after the addition of 0.15 mL of mucus, accounting for about 40% of the tracheostomy tube volume, and full blockage occurred with the addition of 0.3 mL of mucus. During all simulated tracheostomy emergency scenarios, continuous recordings from the carbon dioxide monitoring attachment were obtained. A wired connection between a computer and the monitoring attachment was utilized for raw data collection. Serial carbon dioxide waveform data was collected with a custom computer program (MATLAB; MathWorks, Natick, MA). A moving average filter spanning 100 data points (1 second worth of data) was applied to smooth carbon dioxide waveform readings for graphing purposes.

3. Results

A. Normal Breathing Measurements

Carbon dioxide recordings were collected during simulations of normal tracheostomy tube respiration across all tested age groups (Figure 6). As expected, the frequency of carbon dioxide sensor output waveforms corresponded with age-dependent pediatric breathing rate settings (i.e., respiration rate decreases with age). Measured carbon dioxide levels increased with each age group tested during normal breathing simulations with the tracheostomy attachment monitor while standard mainstream capnograph recordings showed exhaled carbon dioxide levels remained constant. Since the attachment monitor directs airflow over the embedded carbon dioxide sensor rather than using a mainstream approach, age-dependent respiration pressures may be impacting carbon dioxide diffusion to the sensing element. Furthermore, the shape of measured carbon dioxide waveforms from the monitor are sharper compared to the rounded rectangular morphology of normal breathing conditions recorded with standard capnographs.

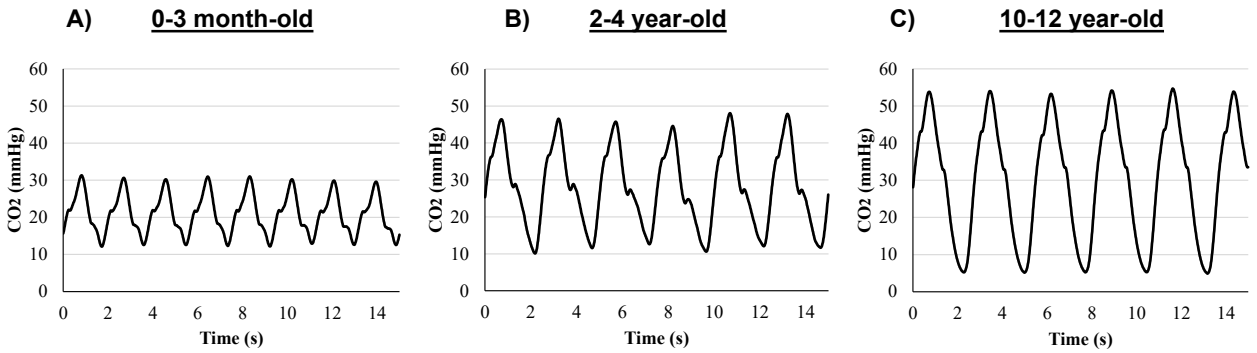

Figure 6. Carbon dioxide waveform recordings during normal breathing in 0–3 month-old infant (A), 2-4 year-old toddler (B), and 10-12 year-old child (C) simulations.

B. Incorrect Insertion Simulation

Simulation during correct placement of the tracheostomy tube into the trachea was performed while recording carbon dioxide levels from the monitoring device (Figure 7A & 7C). Prior to insertion of the tracheostomy tube, static ambient carbon dioxide levels were present followed by the generation of exhaled carbon dioxide breathing waveforms with correct placement into the trachea. Carbon dioxide recordings during incorrect tracheostomy tube insertion into the pretracheal space show ambient levels in the absence of exhaled breaths (Figure 7B & 7D). The distinct differences between monitor readings with correct and incorrect tracheostomy tube insertion indicated that placement complication detection is feasible with the tracheostomy tube attachment device. Neonatal (0-3 months) and pediatric (10-12 years) recordings during correct and incorrect tracheostomy insertion are available (Appendix B & C).

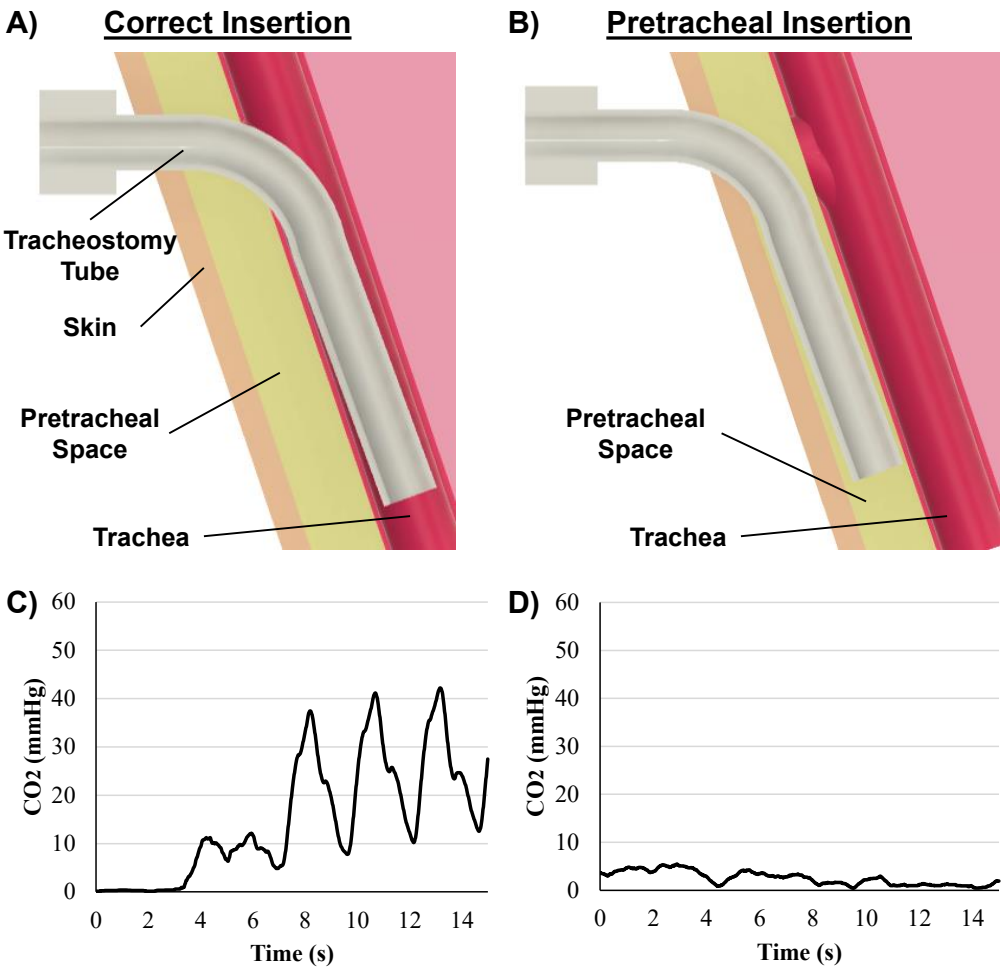

Figure 7. Sagittal cross-section schematics of correct (A) and pretracheal (B) insertion of a tracheostomy tube. Exhaled carbon dioxide readings during correct (C) and incorrect pretracheal (D) insertion of a tracheostomy tube in the 2-4 year-old toddler simulation.

C. Accidental Decannulation Simulation

During simulated accidental decannulation, carbon dioxide level recordings from the monitoring device showed the transition between normal breathing conditions with cyclic breathing patterns to ambient carbon dioxide level (Figure 8). When exhaled carbon dioxide waveforms desist, the tracheostomy tube attachment device could be programmed to quickly

trigger an emergency notification to a caregiver. Neonatal (0-3 months) and pediatric (10-12 years) recordings during accidental decannulation are available (Appendix B & C).

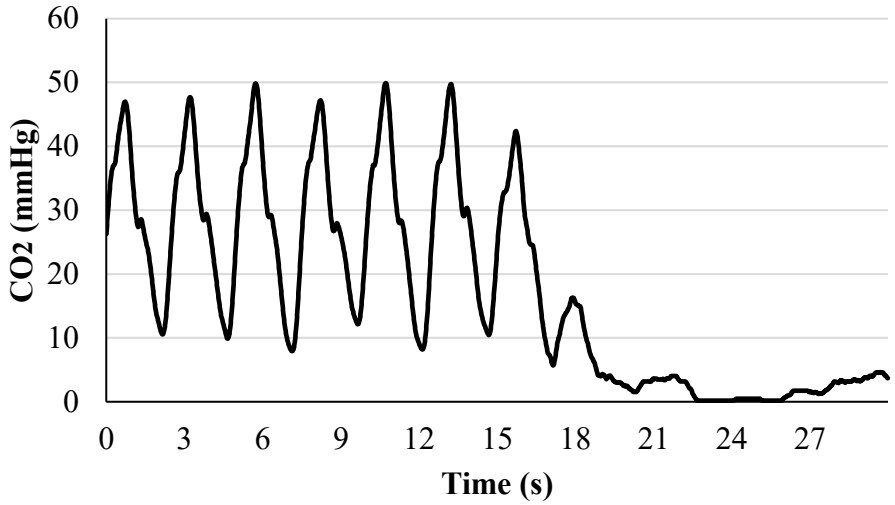

Figure 8. Exhaled carbon dioxide readings for 6 breathing cycles of correct tracheostomy tube placement and subsequent accidental decannulation in the 2-4 year-old toddler simulation.

D. Partial and Full Blockage Simulation

Unobstructed respiration through tracheostomy tubes indicated periodic exhaled carbon dioxide waveforms (Figure 9A & 9D). With partial mucus blockage of a tracheostomy tube, simulation results showed decreased exhaled carbon dioxide waveform amplitude compared to unobstructed conditions (Figure 9B & 9E). Further testing is required to determine the relationship between exhaled carbon dioxide amplitude alterations and occlusion percentage for indicating when tracheostomy tubes require suctioning or cleaning to remove mucus build-up. During simulated full blockage of a tracheostomy tube, carbon dioxide measurements remained static at ambient levels providing a basis for complication detection (Figure 9C & 9F). Neonatal (0-3 months) and pediatric (10-12 years) recordings during complete mucus obstruction are available (Appendix B & C).

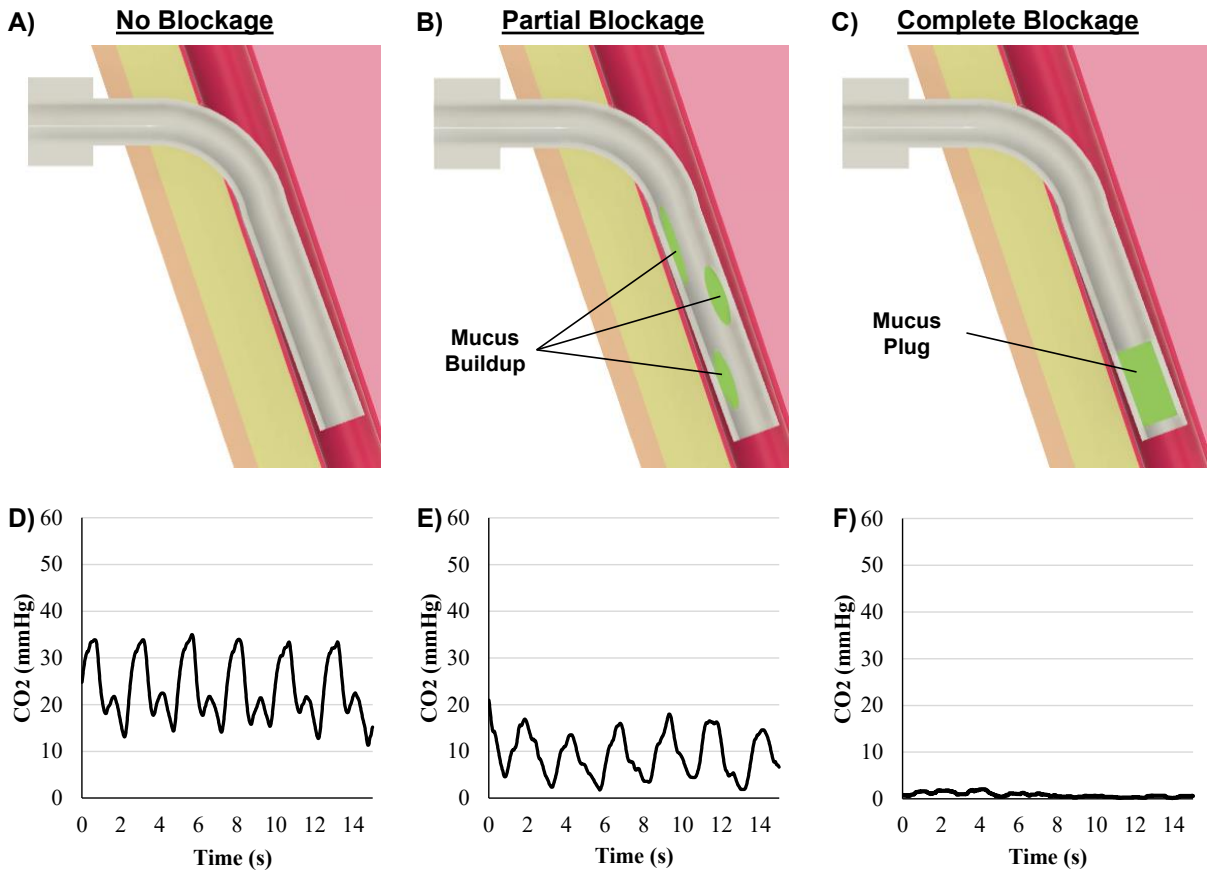

Figure 9. Sagittal cross-section schematics of no (A), partial (B), and complete (C) blockage of a tracheostomy tube in an airway. Exhaled carbon dioxide readings during no (D), partial (E), and full (F) obstruction of a tracheostomy tube in the 2-4 year-old toddler simulation.

4. Discussion

This study demonstrated proof-of-concept for a tracheostomy tube monitoring system designed to quickly and reliably detect critical airway emergencies such as decannulation and obstruction events. Using three-dimensional anatomically accurate pediatric trachea models connected to a breathing simulator, we emulated respiration patterns during tracheostomy tube emergency events for children aged 0-3 months, 2-4 years, and 10-12 years. In addition to assisting with the evaluation of new tracheostomy tube technologies for identifying emergency events in ventilator-independent patients, the tracheal models could also be used for simulation-based medical education allowing caregivers to build and maintain competency and skills in tracheostomy care and complication mitigation [109]. Limitations of the study include that the breathing simulator settings were not adjusted to replicate abnormal breathing patterns, such as those found in patients with respiratory complications (e.g., asthma, apnea, hiccupping). Additionally, only cuffless tracheostomy tubes were tested, as ventilator-independent patients typically do not require cuffs unless severe secretion management is necessary. Furthermore, the simulation setup did not account for the impact of patient mobility on the function of the monitoring attachment.

In conclusion, this work was necessitated by an accidental decannulation emergency event in a ventilator-independent tracheostomized toddler that was not recognized by a caregiver in time and resulted in mortality. Existing portable, medical-grade carbon dioxide sensing systems are not used to constantly monitor for accidental decannulation or obstruction events in ventilator-independent tracheostomized patients since they are not small and compact enough to be worn continuously (> 5 cm in length and weigh 65 g), have limited battery-life (5-10 hours), are costly (~$1500 not including required consumables), and contain interfaces that are tailored for

healthcare professional use. To overcome these constraints, the detection device developed in this study incorporated wireless low-power, carbon dioxide sensing circuitry in the form of a miniaturized tracheostomy tube hub attachment. Functions of the device include: 1) alerting caregivers of accidental decannulation and obstruction, 2) aiding in the confirmation of correct tube placement during emergency and routine tracheostomy tube changes, especially for family members and nurses in at-home settings who often have limited tracheostomy tube care experience, and 3) indicating when tracheostomy tubes require suctioning or cleaning to remove mucus build-up and partial obstructions. The detection tool will also address the limitations of existing monitoring methods by identifying an emergency tracheostomy tube complication faster than standard pulse oximeter techniques, giving caregivers more time to re-establish an airway before permanent injury or death occurs. Overall, this technology will provide a practical solution to preventing injury, death, and recurrent hospitalizations due to pediatric tracheostomy tube complications.

Future efforts include designing signal analysis software for identifying the presence and type of tracheostomy tube complication from carbon dioxide breathing waveforms and triggering a wireless alert. To provide a simple and accessible interface, remote monitoring in the form of a mobile phone application or baby monitor-like device will be engineered to inform and guide caregivers with visual and audio cues during tracheostomy tube complication mitigation efforts. Continuous clinical feedback on the device form factor and weight as well as battery lifetime will be utilized to ensure feasibility for a wearable tracheostomy tube attachment. Furthermore, the size and weight of the battery powering the device requires optimization to ensure the sensitized attachment can meet operation duration and form factor needs. Another anticipated challenge includes balancing device cost and infection control methods. For example, the current sensor

utilized in the carbon dioxide monitor would require disposal on a single use basis as it is not feasible to wash or sterilize daily. Pricing analysis with existing tracheostomy tube accessories (e.g., disposable, single-use heat-moisture exchangers and washable speaking valves) indicate current products cost approximately $2-4/day, therefore alternative methods and technologies for identifying tracheostomy tube complications with cheap disposable or washable sensing components may be preferred.

Appendix A

Supplemental Table 1: 3D printing specifications

Filament material	1.75 mm TPU
Nozzle size	0.4 mm
Layer height	0.2 mm
Nozzle temperature	240˚C
Bed temperature	50˚C
Speed/Acceleration	Uniform 30 mm/s
Flow	115%
Retraction	OFF
Cooling (fan speed)	50%
Infill percentage & type	10% / Gyroid
Support	None
Adhesion	Brim – 5 mm
Shell thickness	2 lines (minimum 0.86 mm)
Top/Bottom layer thickness	5 layers (minimum 0.7) / 4 layers (minimum 0.5)
Combing	Avoid crossing perimeters – ON

Appendix B

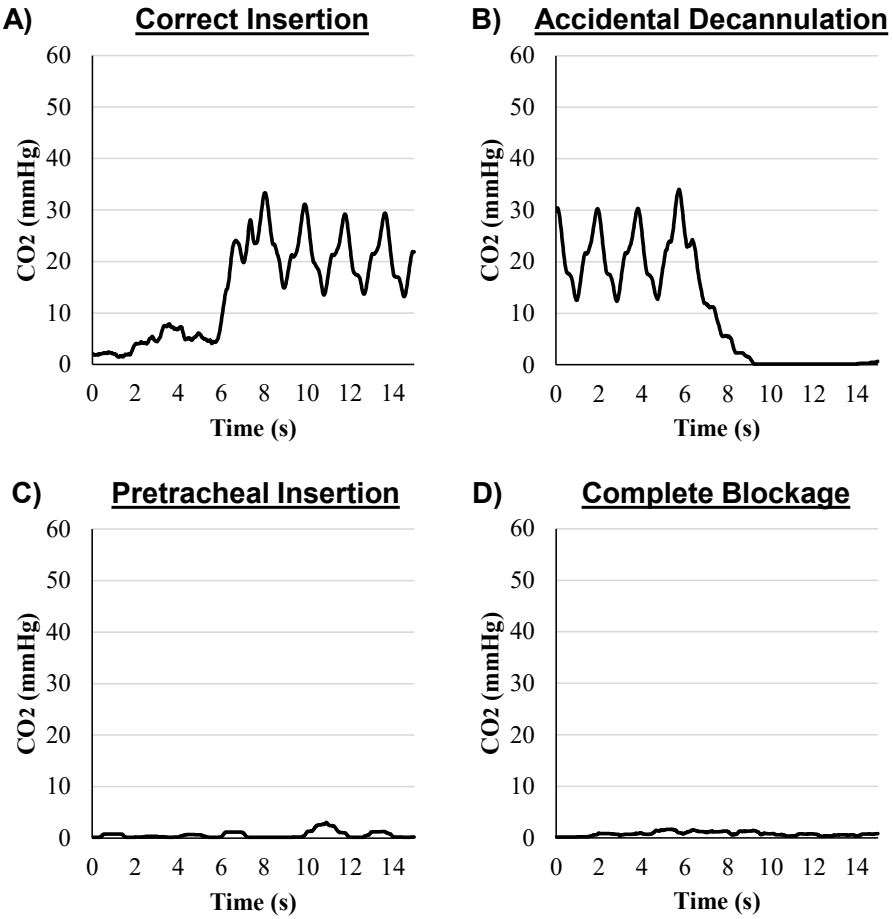

Supplemental Figure 1. Neonatal (0-3 months) exhaled carbon dioxide readings during correct tracheostomy tube placement (A), accidental decannulation (B), incorrect pretracheal insertion (C), and complete mucus obstruction (D).

Appendix C

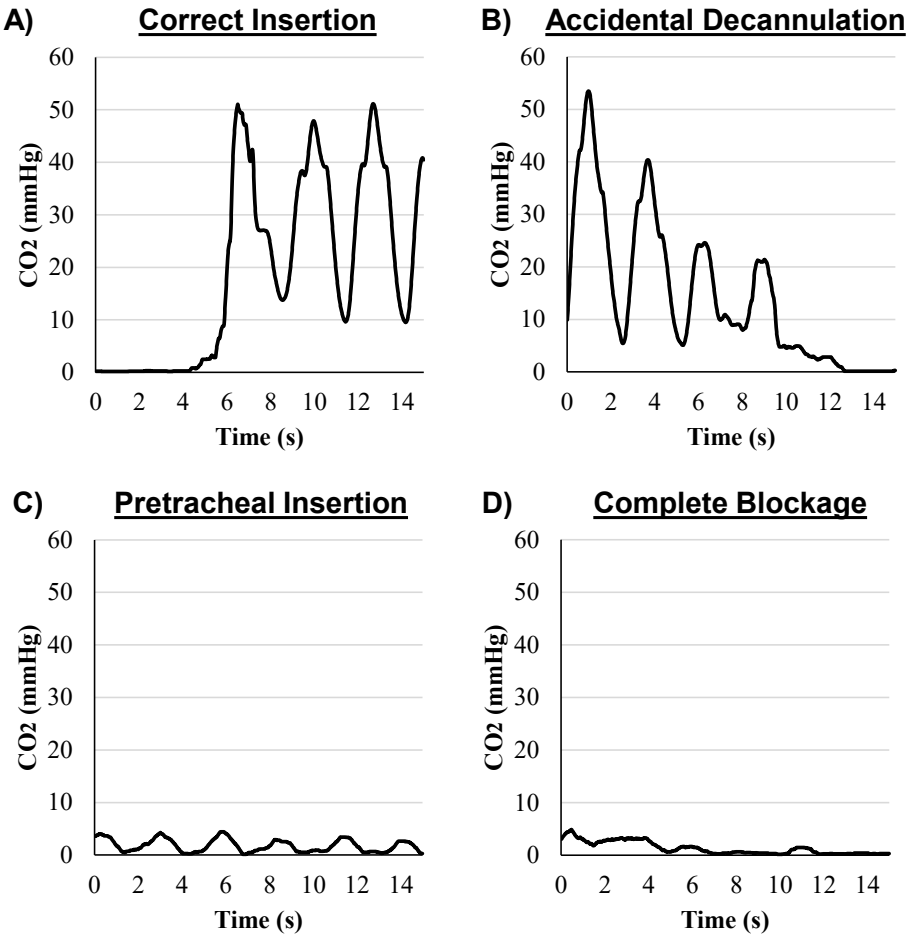

Supplemental Figure 2. Pediatric (10-12 years) exhaled carbon dioxide readings during correct tracheostomy tube placement (A), accidental decannulation (B), incorrect pretracheal insertion (C), and complete mucus obstruction (D).

References

[1] M. V. Paterno, "Incidence and Predictors of Second Anterior Cruciate Ligament Injury After Primary Reconstruction and Return to Sport," *J Athl Train,* vol. 50, no. 10, pp. 1097-9, Oct 2015.

[2] A. M. Abtahi, E. K. Granger, and R. Z. Tashjian, "Factors affecting healing after arthroscopic rotator cuff repair," *World J Orthop,* vol. 6, no. 2, pp. 211-20, Mar 18 2015.

[3] G. R. Lalchandani, R. T. Halvorson, A. L. Zhang, L. L. Lattanza, and I. Immerman, "Patient outcomes and costs after isolated flexor tendon repairs of the hand," *J Hand Ther,* Apr 14 2021.

[4] S. Aufwerber, A. Heijne, G. Edman, K. G. Silbernagel, and P. W. Ackermann, "Does Early Functional Mobilization Affect Long-Term Outcomes After an Achilles Tendon Rupture? A Randomized Clinical Trial," *Orthopaedic Journal of Sports Medicine,* vol. 8, no. 3, p. 2325967120906522, 2020/03/01 2020.

[5] M. Senese, E. Greenberg, J. Todd Lawrence, and T. Ganley, "Rehabilitation Following Isolated Posterior Cruciate Ligament Reconstruction: A Literature Review of Published Protocols," *Int J Sports Phys Ther,* vol. 13, no. 4, pp. 737-751, Aug 2018.

[6] S. R. Filbay and H. Grindem, "Evidence-based recommendations for the management of anterior cruciate ligament (ACL) rupture," *Best Pract Res Clin Rheumatol,* vol. 33, no. 1, pp. 33-47, Feb 2019.

[7] M. Buckthorpe, "Optimising the Late-Stage Rehabilitation and Return-to-Sport Training and Testing Process After ACL Reconstruction," *Sports Med,* vol. 49, no. 7, pp. 1043-1058, Jul 2019.

[8] J. K. Monson, J. Schoenecker, J. W. Matheson, J. O'Keefe, N. Schwery, and A. Hickmann, "Modern Principles for Rehabilitation for Medial and Lateral Knee Ligament

Surgery: How to Optimize Outcomes," *Operative Techniques in Sports Medicine,* vol. 30, no. 2, p. 150915, 2022/06/01/ 2022.

[9] A. Escriche-Escuder, A. I. Cuesta-Vargas, and J. Casana, "Modelling and in vivo evaluation of tendon forces and strain in dynamic rehabilitation exercises: a scoping review," *BMJ Open,* vol. 12, no. 7, p. e057605, Jul 25 2022.

[10] L. Chernak Slane and D. G. Thelen, "The use of 2D ultrasound elastography for measuring tendon motion and strain," *J Biomech,* vol. 47, no. 3, pp. 750-4, Feb 7 2014.

[11] Q. Zhang, N. C. Adam, S. H. Hosseini Nasab, W. R. Taylor, and C. R. Smith, "Techniques for In Vivo Measurement of Ligament and Tendon Strain: A Review," *Ann Biomed Eng,* vol. 49, no. 1, pp. 7-28, Jan 2021.

[12] N. Juncosa, J. R. West, M. T. Galloway, G. P. Boivin, and D. L. Butler, "In vivo forces used to develop design parameters for tissue engineered implants for rabbit patellar tendon repair," *Journal of Biomechanics,* vol. 36, no. 4, pp. 483-488, 2003/04/01/ 2003.

[13] D. C. Meyer, H. A. Jacob, R. W. Nyffeler, and C. Gerber, "In vivo tendon force measurement of 2-week duration in sheep," *J Biomech,* vol. 37, no. 1, pp. 135-40, Jan 2004.

[14] F. Sheng *et al.*, "Ultrastretchable Organogel/Silicone Fiber-Helical Sensors for Self-Powered Implantable Ligament Strain Monitoring," *ACS Nano,* vol. 16, no. 7, pp. 10958-10967, Jul 26 2022.

[15] D. Yan *et al.*, "Ultracompliant Carbon Nanotube Direct Bladder Device," *Adv Healthc Mater,* vol. 8, no. 20, p. e1900477, Oct 2019.

[16] J. Hoer and O. Wetter, "Miniaturized Sensors Registering the Long-Term Course of Suture Tension In Vivo under Varying Intra-Abdominal Pressure," *Sensors (Basel),* vol. 18, no. 6, May 28 2018.

[17] M. E. Cinque, M. Schickendantz, and S. Frangiamore, "Review of Anatomy of the Medial Ulnar Collateral Ligament Complex of the Elbow," *Curr Rev Musculoskelet Med,* vol. 13, no. 1, pp. 96-102, Feb 2020.

[18] M. J. Solomito, R. O. Kostyun, J. T. Sabitsky, and C. W. Nissen, "Trends in Ulnar Collateral Ligament Injuries and Surgery From 2010 to 2019: An Analysis of a National Medical Claims Database," *Orthop J Sports Med,* vol. 12, no. 11, p. 23259671241290532, Nov 2024.

[19] J. Roegele, "2024 MLB Pitchers Who Have Had TJ Surgery," in *Tommy John Surgery List*, ed, 2024.

[20] B. J. Erickson *et al.*, "Trends in Medial Ulnar Collateral Ligament Reconstruction in the United States: A Retrospective Review of a Large Private-Payer Database From 2007 to 2011," *Am J Sports Med,* vol. 43, no. 7, pp. 1770-4, Jul 2015.

[21] O. A. Idowu *et al.*, "Trends of Ulnar Collateral Ligament Reconstruction in the United States from 2003 to 2014: Analysis of 3,133 Patients," *Arthrosc Sports Med Rehabil,* vol. 2, no. 6, pp. e705-e710, Dec 2020.

[22] M. Harrell *et al.*, "Increased Pitch-Specific Velocity, Spin Rate, and Horizontal Movement Lead to Increased Odds of Undergoing Ulnar Collateral Ligament Reconstruction in Professional Baseball Pitchers Using Baseball Savant Data," *Arthroscopy,* Jul 28 2025.

[23] J. J. Greiner, C. A. Trotter, B. E. Walczak, S. J. Hetzel, and G. S. Baer, "Pitching Behaviors in Youth Baseball: Comparison With the Pitch Smart Guidelines," *Orthop J Sports Med,* vol. 9, no. 11, p. 23259671211050127, Nov 2021.

[24] M. S. Fury *et al.*, "Return to Performance After Ulnar Collateral Ligament Reconstruction in Major League Baseball Pitchers: A Case-Control Assessment of Advanced Analytics, Velocity, Spin Rates, and Pitch Movement," *Orthop J Sports Med,* vol. 9, no. 9, p. 23259671211035753, Sep 2021.

[25] S. J. Thomas *et al.*, "Return-to-Play and Competitive Outcomes After Ulnar Collateral Ligament Reconstruction Among Baseball Players: A Systematic Review," *Orthop J Sports Med,* vol. 8, no. 12, p. 2325967120966310, Dec 2020.

[26] C. J. Hadley, D. Edelman, A. Arevalo, N. Patel, M. G. Ciccotti, and C. C. Dodson, "Ulnar Collateral Ligament Reconstruction in Adolescents: A Systematic Review," *Am J Sports Med,* vol. 49, no. 5, pp. 1355-1362, Apr 2021.

[27] J. N. Liu, G. H. Garcia, S. Conte, N. ElAttrache, D. W. Altchek, and J. S. Dines, "Outcomes in revision Tommy John surgery in Major League Baseball pitchers," *J Shoulder Elbow Surg,* vol. 25, no. 1, pp. 90-7, Jan 2016.

[28] L. K. Keyt, J. Tangtiphaiboontana, T. W. Turner, J. S. Dines, M. L. Knudsen, and C. L. Camp, "Revision Medial Ulnar Collateral Ligament Reconstruction in Baseball Pitchers: Review of Epidemiology, Surgical Techniques, and Outcomes," *Curr Rev Musculoskelet Med,* vol. 13, no. 3, pp. 361-368, Jun 2020.

[29] B. J. Erickson *et al.*, "Outcomes of Revision Elbow Medial Ulnar Collateral Ligament Reconstruction in Professional Baseball Players: An Analysis of 191 Pitchers From 2010 to 2023," *Am J Sports Med,* vol. 53, no. 5, pp. 1210-1215, Apr 2025.

[30] G. Yang, B. B. Rothrauff, and R. S. Tuan, "Tendon and ligament regeneration and repair: clinical relevance and developmental paradigm," *Birth Defects Res C Embryo Today,* vol. 99, no. 3, pp. 203-222, Sep 2013.

[31] L. H. Redler, R. M. Degen, L. S. McDonald, D. W. Altchek, and J. S. Dines, "Elbow ulnar collateral ligament injuries in athletes: Can we improve our outcomes?," *World J Orthop,* vol. 7, no. 4, pp. 229-43, Apr 18 2016.

[32] B. M. Ose *et al.*, "Variability of rehabilitation protocols for ulnar collateral ligament repair with suture tape augmentation," *JSES Rev Rep Tech,* vol. 4, no. 4, pp. 703-709, Nov 2024.

[33] J. E. Pichora, G. S. Fraser, L. F. Ferreira, J. R. Brownhill, J. A. Johnson, and G. J. King, "The effect of medial collateral ligament repair tension on elbow joint kinematics and stability," *J Hand Surg Am,* vol. 32, no. 8, pp. 1210-7, Oct 2007.

[34] T. Horeman, E. J. Meijer, J. J. Harlaar, J. F. Lange, J. J. van den Dobbelsteen, and J. Dankelman, "Force sensing in surgical sutures," *PLoS One,* vol. 8, no. 12, p. e84466, 2013.

[35] W. J. Jung, K. S. Kwak, and S. C. Lim, "Vision-Based Suture Tensile Force Estimation in Robotic Surgery," *Sensors (Basel),* vol. 21, no. 1, Dec 26 2020.

[36] N. Marsidi, S. A. M. Vermeulen, T. Horeman, and R. E. Genders, "Measuring Forces in Suture Techniques for Wound Closure," *J Surg Res,* vol. 255, pp. 135-143, Nov 2020.

[37] M. L. Newport and R. L. Tucker, "New perspectives on extensor tendon repair and implications for rehabilitation," *J Hand Ther,* vol. 18, no. 2, pp. 175-81, Apr-Jun 2005.

[38] S. Raniga, J. Cadman, D. Dabirrahmani, D. Bui, R. Appleyard, and D. Bokor, "Mapping of the Inferior Glenohumeral Ligament for Suture Pullout Strength: A Biomechanical Analysis," *Orthop J Sports Med,* vol. 9, no. 1, p. 2325967120969640, Jan 2021.

[39] O. Pearce, M. T. Brown, K. Fraser, and L. Lancerotto, "Flexor tendon injuries: Repair & Rehabilitation," *Injury,* vol. 52, no. 8, pp. 2053-2067, Aug 2021.

[40] C. Y. Yen, Y. J. Tsai, C. K. Hsiao, F. C. Kao, and Y. K. Tu, "Biomechanical evaluation of patellar tendon repair using Krackow suture technique," *Biomed Eng Online,* vol. 18, no. 1, p. 64, May 22 2019.

[41] S. L. Sherman *et al.*, "Graft tensioning during knee ligament reconstruction: principles and practice," *J Am Acad Orthop Surg,* vol. 20, no. 10, pp. 633-45, Oct 2012.

[42] A. Piskopakis *et al.*, "Manual and Device-Assisted Hamstring Autograft Tensioning Yield Similar Outcomes following ACL Reconstruction," *J Clin Med,* vol. 12, no. 14, Jul 11 2023.

[43] M. K. Kaseta, L. E. DeFrate, B. L. Charnock, R. T. Sullivan, and W. E. Garrett, Jr., "Reconstruction technique affects femoral tunnel placement in ACL reconstruction," *Clin Orthop Relat Res,* vol. 466, no. 6, pp. 1467-74, Jun 2008.

[44] L. E. DeFrate, "Effects of ACL graft placement on in vivo knee function and cartilage thickness distributions," *J Orthop Res,* vol. 35, no. 6, pp. 1160-1170, Jun 2017.

[45] M. Liu *et al.*, "Biomimicking Antibacterial Opto-Electro Sensing Sutures Made of Regenerated Silk Proteins," *Advanced Materials,* https://doi.org/10.1002/adma.202004733 vol. 33, no. 1, p. 2004733, 2021/01/01 2021.

[46] Y. Lee *et al.*, "A multifunctional electronic suture for continuous strain monitoring and on-demand drug release," *Nanoscale,* vol. 13, no. 43, pp. 18112-18124, Nov 11 2021.

[47] N. Saranya and T. Kesavamurthy, "Review on next generation wireless power transmission technology for implantable biomedical devices," (in English), *International Journal of Biomedical Engineering and Technology,* vol. 35, no. 3, pp. 207-222, 2021.

[48] L. M. Zhao, H. Li, J. P. Meng, and Z. Li, "The recent advances in self-powered medical information sensors," (in English), *Infomat,* vol. 2, no. 1, pp. 212-234, Jan 2020.

[49] J. E. Ferguson and A. D. Redish, "Wireless communication with implanted medical devices using the conductive properties of the body," (in English), *Expert Review of Medical Devices,* vol. 8, no. 4, pp. 427-433, Jul 2011.

[50] O. Tolu-Akinnawo, N. Akhtar, N. Zalavadia, and M. Guglin, "CardioMEMS Heart Failure System: An Up-to-Date Review," *Cureus,* vol. 17, no. 1, p. e77816, 2025/1/22 2025.

[51] J. Li *et al.*, "An ultrasensitive multimodal intracranial pressure biotelemetric system enabled by exceptional point and iontronics," *Nat Commun,* vol. 15, no. 1, p. 9557, Nov 5 2024.

[52] F. Gao *et al.*, "Wearable and flexible electrochemical sensors for sweat analysis: a review," *Microsyst Nanoeng,* vol. 9, p. 1, 2023.

[53] M. H. Nguyen and H. Fortin Blanchette, "Optimizing AC Resistance of Solid PCB Winding," *Electronics,* vol. 9, no. 5, p. 875, 2020.

[54] S. S. Karipott, P. M. Veetil, B. D. Nelson, R. E. Guldberg, and K. G. Ong, "An Embedded Wireless Temperature Sensor for Orthopedic Implants," *IEEE Sensors Journal,* vol. 18, no. 3, pp. 1265-1272, 2018.

[55] A. R. Carr, Y. J. Chan, and N. F. Reuel, "Contact-Free, Passive, Electromagnetic Resonant Sensors for Enclosed Biomedical Applications: A Perspective on Opportunities and Challenges," *ACS Sens,* vol. 8, no. 3, pp. 943-955, Mar 24 2023.

[56] C. Pacurar *et al.*, "Adapting the Formula for Planar Spiral Inductors' Inductance Computation to the New Oval Geometric Shape, Ideal for Designing Wireless Power Transfer Systems for Smart Devices," *Mathematics,* vol. 13, no. 3, p. 348, 2025.

[57] Z. Dong *et al.*, "A dual-sensitive element wireless passive LC temperature sensor and application in bearing monitoring," *Measurement Science and Technology,* vol. 37, no. 7, p. 075105, 2026/02/23 2026.

[58] S. S. Karipott, B. D. Nelson, R. E. Guldberg, and K. G. Ong, "A Wireless, Battery-Free Embedded Sensor for Monitoring Tension on a Suture Anchor," *IEEE Sensors Journal,* vol. 22, no. 2, pp. 1173-1179, 2022.

[59] K. M. Meyers and K. G. Ong, "Pledget Sensor to Monitor Loading in Tendon and Ligament Sutures During Postoperative Physical Therapy," *IEEE Sensors Journal,* vol. 22, no. 19, pp. 18384-18390, 2022.

[60] S. S. Karipott, Kaylee Meyers, Stephen Laffoon, Michael McGeehan, Samuel Adams, Jonathan Riboh, Nicholas Strasser, Ken Gall, Robert Guldberg, and Keat Ghee Ong, "Wireless Suture Button Accessory Sensor for Intra- and Post-Operative Monitoring of Suture Loading in Soft Tissue Reconstruction," *Journal of Orthopaedic Experience & Innovation,* vol. 6, no. 1, 2025.

[61] G. R. Huffman, C. Piper, R. Gupta, and M. W. Hast, "Similar Biomechanics Between the Double-Cortical Button and Docking Techniques for Ulnar Collateral Ligament

Reconstruction: A Cadaveric Evaluation," *Orthop J Sports Med,* vol. 11, no. 1, p. 23259671221123342, Jan 2023.

[62] T. R. McAdams, A. T. Lee, J. Centeno, N. J. Giori, and D. P. Lindsey, "Two ulnar collateral ligament reconstruction methods: the docking technique versus bioabsorbable interference screw fixation--a biomechanical evaluation with cyclic loading," *J Shoulder Elbow Surg,* vol. 16, no. 2, pp. 224-8, Mar-Apr 2007.

[63] G. Saiko, "Skin Temperature: The Impact of Perfusion, Epidermis Thickness, and Skin Wetness," *Applied Sciences*, vol. 12, no. 14. doi: 10.3390/app12147106

[64] R. F. Escamilla, T. D. Macleod, K. E. Wilk, L. Paulos, and J. R. Andrews, "Anterior cruciate ligament strain and tensile forces for weight-bearing and non-weight-bearing exercises: a guide to exercise selection," *J Orthop Sports Phys Ther,* vol. 42, no. 3, pp. 208-20, Mar 2012.

[65] M. Kharazi, S. Bohm, C. Theodorakis, F. Mersmann, and A. Arampatzis, "Quantifying mechanical loading and elastic strain energy of the human Achilles tendon during walking and running," *Sci Rep,* vol. 11, no. 1, p. 5830, Mar 12 2021.

[66] K. A. Barrie, S. L. Tomak, J. Cholewicki, and S. W. Wolfe, "The role of multiple strands and locking sutures on gap formation of flexor tendon repairs during cyclical loading," *J Hand Surg Am,* vol. 25, no. 4, pp. 714-20, Jul 2000.

[67] T. Sakamoto *et al.*, "Clinical Outcomes of Modified Suture Buttons for Tibial Side Fixation in Anterior Cruciate Ligament Reconstruction: A Retrospective Comparative Study," *Cureus,* vol. 16, no. 7, p. e64357, Jul 2024.

[68] Z. Wei, Z. Zhang, W. Zhu, and X. Weng, "Polyetheretherketone development in bone tissue engineering and orthopedic surgery," *Front Bioeng Biotechnol,* vol. 11, p. 1207277, 2023.

[69] R. Mirzayan, K. Schoell, D. C. Acevedo, and A. Singh, "Ulnar Collateral Ligament Reconstruction of the Elbow With Double Suspensory Fixation," *Arthrosc Tech,* vol. 10, no. 2, pp. e303-e309, Feb 2021.

[70] B. W. Fossum, M. L. Vopat, J. R. Brown, S. M. Comfort, C. A. Su, and R. W. Viola, "Ulnar Collateral Ligament (UCL) Reconstruction With Proximal Single-Tunnel Suspensory Fixation," *Arthrosc Tech,* vol. 12, no. 6, pp. e997-e1002, Jun 2023.

[71] K. Delbé *et al.*, "Contribution of Raman analysis on tribological study of PEEK reinforced with micro or nano SiC particles," *Wear,* vol. 570, p. 205927, 2025/06/01/ 2025.

[72] K. Hwang, H. Kim, and D. J. Kim, "Thickness of skin and subcutaneous tissue of the free flap donor sites: A histologic study," *Microsurgery,* vol. 36, no. 1, pp. 54-8, Jan 2016.

[73] L. F. Solon, R. M. Castile, M. V. Smith, and S. P. Lake, "Mechanical properties and microstructural organization of common ulnar collateral ligament grafts: Palmaris longus and gracilis tendons," *J Orthop Res,* vol. 40, no. 8, pp. 1865-1871, Aug 2022.

[74] M. L. Vopat *et al.*, "Biomechanical comparison of ulnar collateral ligament reconstruction with single-tunnel proximal suspensory fixation versus modified docking technique," *JSES Int,* vol. 7, no. 2, pp. 364-369, Mar 2023.

[75] M. A. David, A. M. Chamberlain, and S. P. Lake, "Preclinical Models of Elbow Injury and Pathology," *Ann Jt,* vol. 6, Jan 2021.

[76] B. Van Trigt, L. Vliegen, T. Leenen, and D. Veeger, "The ulnar collateral ligament loading paradox between in-vitro and in-vivo studies on baseball pitching (narrative review)," *International Biomechanics,* vol. 8, no. 1, pp. 19-29, 2021/01/01 2021.

[77] V. Burgio *et al.*, "Mechanical properties of animal ligaments: a review and comparative study for the identification of the most suitable human ligament surrogates," *Biomech Model Mechanobiol,* vol. 22, no. 5, pp. 1645-1683, Oct 2023.

[78] N. L. Zaino, M. J. Hedgeland, M. J. Ciani, A. M. Clark, L. Kuxhaus, and A. J. Michalek, "White-Tailed Deer as an Ex Vivo Knee Model: Joint Morphometry and ACL Rupture Strength," *Ann Biomed Eng,* vol. 45, no. 4, pp. 1093-1100, Apr 2017.

[79] P. Ayyadurai *et al.*, "An update on the CardioMEMS pulmonary artery pressure sensor," *Ther Adv Cardiovasc Dis,* vol. 13, p. 1753944719826826, Jan-Dec 2019.

[80] M. Haerinia and R. Shadid, "Wireless Power Transfer Approaches for Medical Implants: A Review," *Signals*, vol. 1, no. 2*,* pp. 209-229. doi: 10.3390/signals1020012

[81] J. R. Dugas *et al.*, "Clinical Outcomes of Ulnar Collateral Ligament Repair With Internal Brace Versus Ulnar Collateral Ligament Reconstruction in Competitive Athletes," *Am J Sports Med,* vol. 53, no. 3, pp. 525-536, Mar 2025.

[82] M. Sakai, Y.-F. Kou, G. B. Shah, and R. F. Johnson, "Tracheostomy demographics and outcomes among pediatric patients ages 18 years or younger—United States 2012," *The Laryngoscope,* https://doi.org/10.1002/lary.27463 vol. 129, no. 7, pp. 1706-1711, 2019/07/01 2019.

[83] K. F. Watters, "Tracheostomy in Infants and Children," *Respir Care,* vol. 62, no. 6, pp. 799-825, Jun 2017.

[84] J. B. Mahida *et al.*, "Tracheostomy Placement in Children Younger Than 2 Years: 30-Day Outcomes Using the National Surgical Quality Improvement Program Pediatric," *JAMA Otolaryngology–Head & Neck Surgery,* vol. 142, no. 3, pp. 241-246, 2016.

[85] C. Hartnick, G. Diercks, V. De Guzman, E. Hartnick, J. Van Cleave, and K. Callans, "A quality study of family-centered care coordination to improve care for children undergoing tracheostomy and the quality of life for their caregivers," *International Journal of Pediatric Otorhinolaryngology,* vol. 99, pp. 107-110, 2017/08/01/ 2017.

[86] M. J. Brenner *et al.*, "Global Tracheostomy Collaborative: data-driven improvements in patient safety through multidisciplinary teamwork, standardisation, education, and patient partnership," *British Journal of Anaesthesia,* vol. 125, no. 1, pp. e104-e118, 2020/07/01/ 2020.

[87] L. Cardoso, J. C. Ribeiro, J. Neves, M. Cruz, and L. Silva, "Tracheotomy decannulation in children under one year of age," *Arch. Head Neck Surg.,* vol. 47, no. 2, p. e0928, 2018.

[88] J. F. Lubianca Neto, O. C. Castagno, and A. K. Schuster, "Complications of tracheostomy in children: a systematic review," *Braz J Otorhinolaryngol,* vol. 88, no. 6, pp. 882-890, Nov-Dec 2022.

[89] N. Hall *et al.*, "Providing care for children with tracheostomies: a qualitative interview study with parents and health professionals," *BMJ Open,* vol. 13, no. 1, p. e065698, Jan 31 2023.

[90] J. Sherman, K. L. Bower, and K. Eskandanian, "“100 Things I Wish Someone Would Have Told Me”: Everyday Challenges Parents Face While Caring for Their Children With a Tracheostomy," *Qualitative Health Research,* vol. 0, no. 0, p. 10497323231217387, 2024.

[91] P. Das, H. Zhu, R. K. Shah, D. W. Roberson, J. Berry, and M. L. Skinner, "Tracheotomy-related catastrophic events: results of a national survey," *Laryngoscope,* vol. 122, no. 1, pp. 30-7, Jan 2012.

[92] G. Akangire *et al.*, "Respiratory, growth, and survival outcomes of infants with tracheostomy and ventilator dependence," *Pediatr Res,* vol. 90, no. 2, pp. 381-389, Aug 2021.

[93] K. B. Hebbar *et al.*, "Mortality and Outcomes of Pediatric Tracheostomy Dependent Patients," *Front Pediatr,* vol. 9, p. 661512, 2021.

[94] S. V. Gregory *et al.*, "Factors Associated With Accidental Decannulation in Tracheostomized Children," *Respiratory Care,* p. respcare.09673, 2022.

[95] R. F. Nawaz, B. Page, E. Harrop, and C. A. Vincent, "Analysis of paediatric long-term ventilation incidents in the community," *Arch Dis Child,* vol. 105, no. 5, pp. 446-451, May 2020.

[96] R. B. Mitchell *et al.*, "Clinical consensus statement: tracheostomy care," *Otolaryngol Head Neck Surg,* vol. 148, no. 1, pp. 6-20, Jan 2013.

[97] U. Goneppanavar, S. Rao, N. Shetty, P. Manjunath, D. T. Anjilivelil, and S. S. Iyer, "Light at a tunnel's end: The lightwand as a rapid tracheal location aid when encountering false passage during tracheostomy," *Indian Journal of Critical Care Medicine : Peer-reviewed, Official Publication of Indian Society of Critical Care Medicine,* vol. 14, pp. 144 - 146, 2010.

[98] J. Ng, S. Hamrang-Yousefi, and A. Agarwal, *Tracheostomy Tube Change*. StatPearls Publishing, Treasure Island (FL), 2022.

[99] L. G. Amar-Dolan *et al.*, "“This Is How Hard It Is”. Family Experience of Hospital-to-Home Transition with a Tracheostomy," *Annals of the American Thoracic Society,* vol. 17, no. 7, pp. 860-868, 2020/07/01 2020.

[100] A. W. Ho, D. E. Moul, and J. Krishna, "Neck Circumference-Height Ratio as a Predictor of Sleep Related Breathing Disorder in Children and Adults," (in English), *Journal of Clinical Sleep Medicine,* vol. 12, no. 3, pp. 311-317, 2016.

[101] M. Kondolot *et al.*, "Neck Circumference to Assess Obesity in Preschool Children," *J Clin Res Pediatr Endocrinol,* vol. 9, no. 1, pp. 17-23, Mar 1 2017.

[102] R. Leach, S. Hachimi Idrissi, J. Meulemans, K. Monsieurs, O. Vanderveken, and V. Vander Poorten, "Complex intubation, cricothyrotomy and tracheotomy," *B-ENT,* vol. Suppl 26, no. 2, pp. 103-118, 2016.

[103] N. Hammer *et al.*, "Cervical vagus nerve morphometry and vascularity in the context of nerve stimulation - A cadaveric study," *Sci Rep,* vol. 8, no. 1, p. 7997, May 22 2018.

[104] M. Ozturk, E. Uysal, Z. I. Bayramoglu, M. Y. Ozlu, and O. Erdur, "Measurement of the subglottic diameter of the trachea and its distance from the skin by ultrasonography in children," *Int J Pediatr Otorhinolaryngol,* vol. 150, p. 110946, Nov 2021.

[105] I. Waechter, S. Seifert, and R. Dillmann, "AUTOMATIC SEGMENTATION OF CERVICAL SOFT TISSUE FROM MR IMAGES," 01/01 2005.

[106] A. A. Chakkarapani *et al.*, ""Current concepts of mechanical ventilation in neonates" - Part 1: Basics," *Int J Pediatr Adolesc Med,* vol. 7, no. 1, pp. 13-18, Mar 2020.

[107] M. Kollisch-Singule *et al.*, "Mechanical Ventilation in Pediatric and Neonatal Patients," *Front Physiol,* vol. 12, p. 805620, 2021.

[108] S. Damam *et al.*, "Navigating Pediatric Capnography: A Comprehensive Review of Scope and Limitations," *Cureus,* vol. 16, no. 1, p. e53289, Jan 2024.

[109] G. Doucet, S. Ryan, M. Bartellas, M. Parsons, A. Dubrowski, and T. Renouf, "Modelling and Manufacturing of a 3D Printed Trachea for Cricothyroidotomy Simulation," *Cureus,* vol. 9, no. 8, p. e1575, Aug 18 2017.